UNIVERSITÀ DI PARMA

UNIVERSITA' DI PARMA

DOTTORATO DI RICERCA IN
SCIENZA E TECNOLOGIA DEI MATERIALI

CICLO XXXVIII

Molecular structure and excited state dynamics: from OLEDs to 2D IR

Coordinatore:
Prof. Mauro Riccò

Tutori
Prof. Anna Painelli
Dr. Dang Khoa Andrea Phan Huu

Dottorando:
Dr. Andrea Landi

Anni accademici 2022/2023 - 2024/2025

Contents

Introduction

As we shift from the macroscopic to the microscopic realm, the laws of classical physics do not longer apply since *quantum effects* become non negligible. The behavior of atoms and molecules must be explained through the rules of *quantum physics*, and the concept of quantized (discrete) states arises. Momentum and position of a particle cannot be precisely measured at the same time. The *Heisenberg uncertainty principle*, in fact, sets a limit on how precisely the linear momentum (the velocity) and the position of a quantum particle can be measured simultaneously. The traditional definition of the state of a classical system, in terms of the position and velocity of each particle is therefore no more applicable, and the introduction of the concept of *quantum states* is necessary. The lowest energy state of a system is called *ground state*, while higher energy states are called *excited states*.

A macroscopic system shows a natural tendency to reach thermodynamic equilibrium, a condition characterized by simultaneous mechanical, thermal, and chemical equilibrium. Once this condition is attained, there is no macroscopic motion, no heat flow, and no chemical exchange within the system. At the equilibrium, the populations of the states obey the *Boltzmann distribution law*, which uniquely determines the population of each state based on its energy and the temperature of the system.

The interaction of the system with any external source of perturbation can alter the thermodynamic equilibrium. If a certain amount of population is shifted from the lower energy states to the higher energy states, the process is called *excitation*. A system can be driven out of equilibrium in several ways, depending on the source of the perturbation:

- Optical excitation, achieved by shining light on the system. This represents the easiest method to generate excited states and it is the one responsible for the functioning of solar cells;

- Electrical excitation, where excited states are generated through the injection and recombination of holes and electrons. This method is fundamental in the field of light emitting diodes (LEDs);

- Thermal excitation, achieved by increasing the temperature of the system, causing the populations of the states to readjust according to the Boltzmann distribution corresponding to the higher temperature;

- Chemical excitation, where the energy released from a chemical reaction can be absorbed by the system to generate excited states.

Once the system is brought out of equilibrium, following the principles of thermodynamics, the excess energy of the system must be released to the environment through the *relaxation* of the excited states. This excess energy can be dissipated either radiatively, through emissive processes such as fluorescence or phosphorescence, or non-radiatively, occurring through heat exchanges, which are the macroscopic consequences of the inelastic collisions.

Understanding deactivation pathways is crucial towards the optimization of optoelectronic devices such as OLEDs (Organic LEDs), LASER (Light Amplification by Stimulated Emission of Radiation) and solar cells, to mention a few. More specifically, the competition between radiative and non-radiative decay pathways profoundly affects the maximum internal quantum efficiency of the devices. A clever chemical design of the active species (the dyes) and a detailed understanding of environmental (matrix) effects are key tools for controlling the deactivation pathways of excited states. In this context, vibrational and conformational degrees of freedom of the dyes of interest play a major role. However, obtaining a complete understanding of the excited-state deactivation pathway is far from straightforward. Integrating experimental measurements with appropriate theoretical models and computational approaches is essential to elucidate the time-dependent behavior of the system.

From a computational perspective, modeling relaxation phenomena is challenging. Specifically, non-radiative decays require the interaction of the *system*, typically an object (a molecule or a collection of molecules) small enough to be dealt with quantum-mechanically, with the surrounding environment, which is a large enough system to constitute a good thermal bath. In other terms, we must abandon the familiar realm of *closed quantum system* to reach the much more complex real of *closed quantum system*. The three main chapters of this thesis address these general themes from different perspectives.

In the first chapter, a comprehensive study of the factors affecting the structure property relationships of two families of dyes of interest for OLED application is presented. More specifically, we are interested to elucidate the delicate photophysics of thermally activated delayed fluorescence (TADF), a mechanism underlying the third OLED generation. A general approach is proposed to investigate the effects of molecular modifications and solvation on TADF properties of a series of donor–acceptor systems derived from DMAC-TRZ. The modifications examined include the introduction of an additional nitrogen atom into the acridan scaffold and changes to the phenyl bridge linking the donor and acceptor moieties. The goal is to gain deeper insight into the excited-state dynamics of the conformers and their implications for properties such as TADF efficiency and emission color. Moreover, a detailed experimental and computational investigation is carried out on a second series of TADF emitters derived from DMAC-TRZ through chemical modification of the donor and/or acceptor units. This study explores how variations in peripheral groups influence the complex photophysics underlying the TADF phenomena in these systems.

In the second chapter, we address the delicate issue of estimating non-radiative rates, a particulary relevant topic in the optimization of OLEDs. Adopting the displaced harmonic oscillator as a reference toy model, we critically address recent computational strategies employed to evaluate non-radiative rates, underlying relevant

approximations. A comparison between rates extracted from the Fermi Golden Rule (FGR), as usually adopted in commercial computational codes, and rigorous open quantum system approaches, provides a good reliability test. A blended approach is proposed, thus enabling a rigorous comparison of the rate functions obtained from both techniques.

Finally, in chapter 3, we address the simulation of two-dimensional infrared (2D IR) spectra of dimethylindoaniline (phenol blue), a dye with well characterized vibrational solvatochromism. Our goal is to implement the solvation dynamics in the simulation of the 2D IR. The standard approach to 2D IR spectra relies on the linear expansion of the density matrix on the perturbing fields. However, the density matrix obtained along these lines is not "well-behaved" and, as such, cannot be propagated using "open quantum system" approaches. While the results reported in the third chapter are preliminary, we are setting the path towards an original approach to the calculation of 2D IR spectra that, in perspective, will allow us to deal with the complex and mutually entangled relaxation dynamics of the dye and of the surrounding solvent.

Chapter 1

Computational study of two families of TADF dyes for OLED applications

1.1 Introduction

Organic light-emitting diodes (OLEDs) have emerged as a leading display technology, offering advantages such as high efficiency, flexibility, and a wide color gamut, all of which are required for today's high-definition displays[1]. A critical aspect of the performance of OLED lies in the effective harvesting of excitons, which are generated as 25% singlet and 75% triplet states due to spin statistics[2, 3]. The first OLED generation, relying on fluorescent dyes is then poorly efficient and is actually exploited in commercial devices only for blue OLED, where other strategies are not viable, as for today. The second OLED generation, born thanks to an original idea of Forrest,[4] relies on phosphorescent materials, where the inclusion of heavy atoms (typically platinum or iridium) leads to efficient spin–orbit coupling (SOC).[5] The resulting large intersystem crossing (ISC) ensures the efficient transformation of electrogenerated singlets into triplet states whose emissive nature is again related to the large SOC. Along these lines, 100% maximum internal quantum efficiency can be achieved and commercial red and green OLED typically rely on this technology. The third generation of OLED is based on an original suggestion of Adachi, who proposed to exploit the known phenomenon of thermally activated delayed fluorescence (TADF) to harvest singlet and triplet excitons.[3, 6] TADF-OLED rely on purely organic materials without the need of introducing expensive, potentially toxic, and hard-to-recycle metals. TADF emitters are characterized by a small singlet-triplet energy gap (ΔE_{ST}) so that thermal energy is enough to allow for a reverse ISC (rISC) from the triplet to the singlet state. Accordingly, the electrogenerated (dark) triplet states are reconverted into (bright) singlets ensuring again 100% efficiency. The name TADF comes from the behavior of photoluminescence of these systems: upon photoexcitation, only the singlet state is populated. A portion of the excited population will emit light, in the so-called prompt fluorescence (typically in the ns timescale), but a portion of the population will be transferred to the triplet (ISC) and back to the singlet (rISC) from where a delayed fluorescence will be observed, typically in the microsecond timescale. After the original suggestion by Adachi [7, 8],

a lot of research activity was initiated in the field,[9–13] leading to several strategies towards optimal TADF emitters, including through bond structures [8, 14–18] and donor-acceptor (DA) space structures,[19–21] multiresonant structures [22–25] and more complex strategies, such as, e.g. hyperfluorescent systems.[26–28] Even limiting the attention to the basic through-bond DA structures, the physics of TADF is far from trivial: the two basic requirements for TADF, i.e. a small ΔE_{ST} and a sizable spin-orbit coupling (SOC) matrix element, are indeed mutually exclusive. The minimization of ΔE_{ST} is in fact based on the minimization of the overlap between the frontier orbitals on the D and A molecular fragments.[29, 30] In this way, the lowest excited singlet and triplet states are almost degenerate, both having a predominant charge transfer (CT) character, D^+A^-, with two unpaired electrons in virtually disconnected molecular moieties. However, in these conditions, according to the El-Sayed rule,[31] the SOC matrix element between the two states is vanishingly small. Efficient TADF emitters then require the active involvement of local excited (LE) triplet states [10, 32–35] as well as vibronic coupling.[18, 33, 36–40]

The scenario is made even more complex by environmental effects: the medium polarity affects in different ways the energies and the nature of CT and LE states, with a direct impact on SOC and ΔE_{ST}.[12, 40–42] Moreover, the medium rigidity affects the conformational structure and mobility of the dye, then profoundly altering its photophysics.[43–47] In this chapter, an extensive computational analysis is

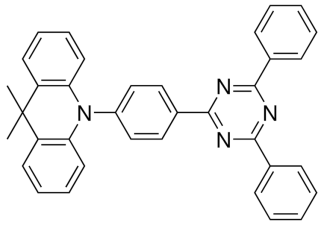

Figure 1.1: Molecular structure of DMAC-TRZ.

reported on two families of TADF dyes of interest for OLED applications. Both families of compounds are related to the prototypical 10-(4-(4,6-Diphenyl-1,3,5-triazin-2-yl)phenyl)-9,9-dimethyl-9,10-dihydroacridine (DMAC-TRZ, see Fig. 1.1) dye that has been extensively investigated in the host laboratory.[48, 49] The first family of molecules addresses two topics: the effect of incorporating a second nitrogen atom into the acridan scaffold and the effect of the removal of the phenylene unit bridging the D and A molecular moieties. This study was performed in collaboration with the research groups of Prof. Eli Zysman-Colman (St. Andrew University) and Prof. Stefan Bräse (Karlsrue Institute of Technology), who provided the materials, and with Prof. Andrew Monkman (Durham University), who is responsible for the spectroscopic measurements. The second family of molecules addresses a delicate issue, showing that marginal variations of peripheral groups in the donor or acceptor units may alter the geometry of the system with profound and somewhat unexpected effects on the photophysics of the system. This work was done in collaboration with Prof. Hironori Kaji (Kyoto University), who provided the materials. The spectroscopic characterization was performed in the host laboratory Dr. Ottavia Racchi, under the supervision of Prof. Cristina Sissa.

1.2 Radiative vs rISC rate: How a Bridging Phenyl Controls Everything in TADF molecules

Fig. 1.2 shows the molecular structures of interest. Specifically, starting from DMAC-TRZ, a second nitrogen atom is introduced in the acridan structure to get the donor residue dubbed as 4AzaDMAC. Moreover, the DMAC- and 4AzaDMAC-donor units are attached to an acceptor that may have or may not have the phenyl brigde, resulting into the -TRZ or -DPT acceptor, respectively.

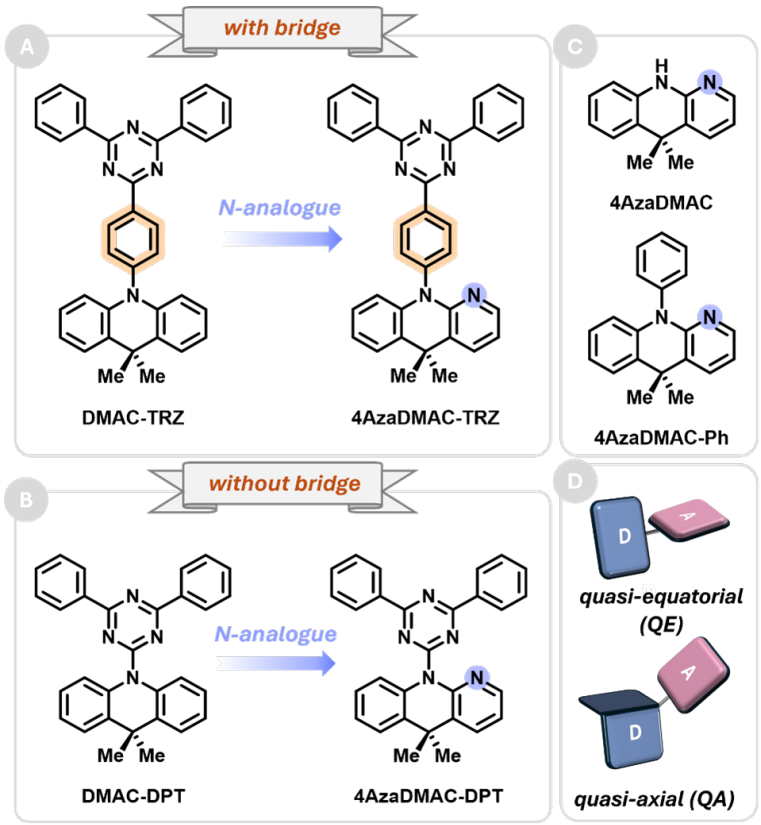

Figure 1.2: (A–C) Molecular structures of interest: **DMAC–TRZ** (10-(4-(4,6-diphenyl-1,3,5-triazin-2-yl)phenyl)-9,9-dimethyl-9,10-dihydroacridine), **4AzaDMAC–TRZ** (10-(4-(4,6-diphenyl-1,3,5-triazin-2-yl)phenyl)-5,5-dimethyl-5,10-dihydrobenzo[b][1,8]naphthyridine), **DMAC–DPT** (10-(4,6-diphenyl-1,3,5-triazin-2-yl)-9,9-dimethylacridine), **4AzaDMAC–DPT** (10-(4,6-diphenyl-1,3,5-triazin-2-yl)-5,5-dimethylbenzo[b][1,8]naphthyridine), **4AzaDMAC** (5,5-dimethyl-10H-benzo[b][1,8]naphthyridine), and **4AzaDMAC–Ph** (5,5-dimethyl-10-phenylbenzo[b][1,8]naphthyridine). (D) The two possible conformational states of the dyes.

1.2.1 Crystal structures

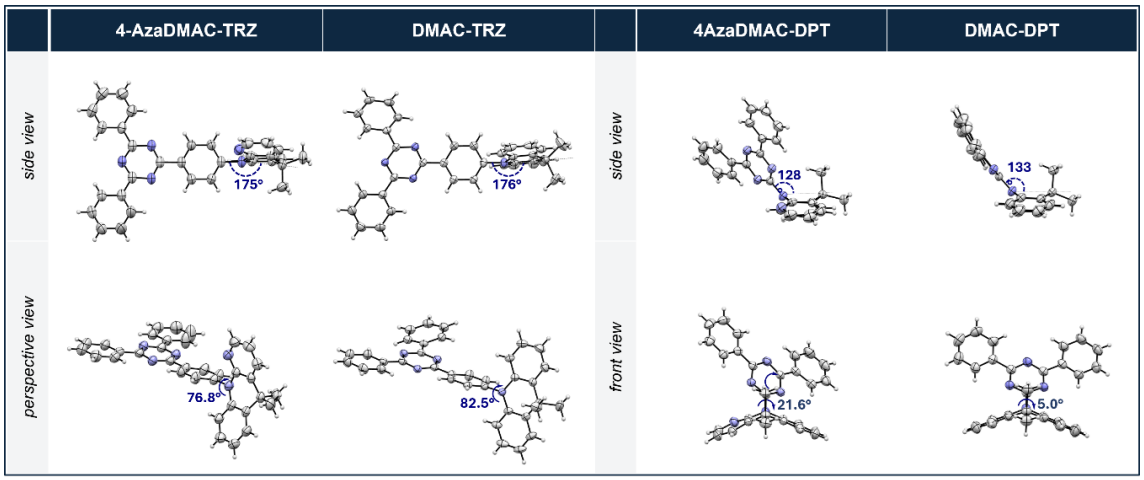

Figure 1.3: Crystal structures of 4AzaDMAC-TRZ, DMAC-TRZ, 4AzaDMAC-DPT and DMAC-DPT.

The ground state molecular configurations of the compounds were determined by X-ray diffraction measurements on single crystals (Fig. 1.3). While the phenyl bridged compounds adopt a quasi-equatorial (QE) conformation, the short diphenyltriazine substituted compounds are in the quasi-axial (QA) conformation. For 4AzaDMAC-TRZ and DMAC-TRZ, the donors and phenyl triazine acceptor are twisted by 76.8° and 82.5°, respectively, with the donors being nearly planar. Without the phenyl bridge, the structures adopt a less twisted structure, with a dihedral angle of 21.6° and 5.0° for 4AzaDMAC-DPT and DMAC-DPT, respectively. In these QA structures, the bending angles are large, amounting to 128° for 4AzaDMAC-DPT and 133° for DMAC-DPT, as shown in the right panel of Fig. 1.3.

1.2.2 Photophysical analysis

Steady-state absorption and emission spectra were measured in toluene to map the excited state properties (Fig. 1.4). When a strong acceptor is connected to 4AzaDMAC via a phenyl group (in 4AzaDMAC-TRZ), a broad absorption band is seen at $\sim 370\,\text{nm}$, which is not present in either the donor 4AzaDMAC (or 4AzaDMAC-Ph), or the TRZ acceptor[48]. This band therefore is safely ascribed to a charge transfer (CT) state. It shows a marginal solvatochromism, as expected for an emitter with a largely neutral ground state (Fig. 1.5).[42, 50] A similar observation holds true for DMAC-TRZ[48]. The CT band of DMAC-TRZ is red-shifted compared to the 4AzaDMAC-TRZ, due to the stronger donor character of DMAC, compared to 4AzaDMAC. When the phenylene bridge is removed, the absorption spectra changes significantly, with both 4AzaDMAC-DPT and DMAC-DPT showing a very weak CT absorption band, if any.

As for emission, both 4AzaDMAC-TRZ and DMAC-TRZ show a minimal Stokes shift in non-polar or weakly polar solvents (Fig. 1.4b), suggesting that the emission originates from the same CT state responsible for the absorption. The CT origin

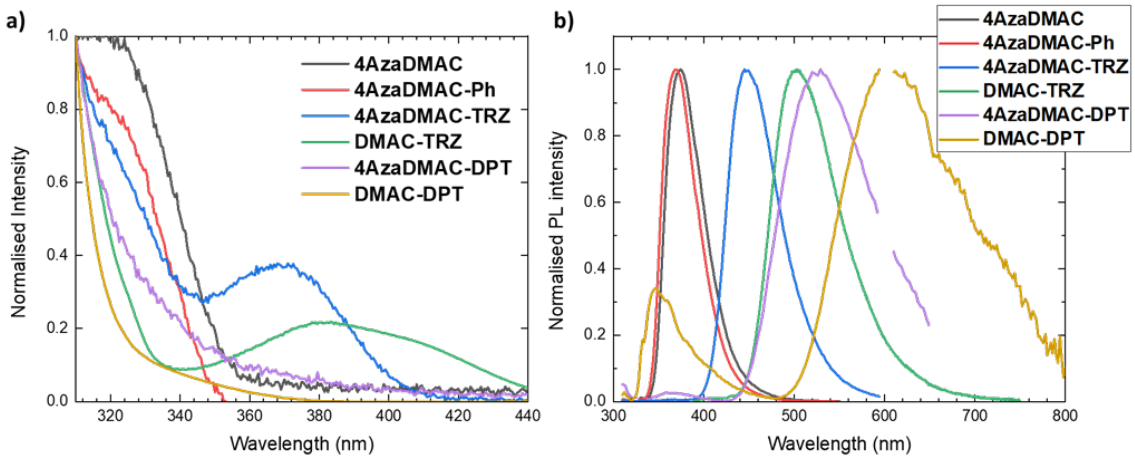

Figure 1.4: a) Normalized steady-state absorption spectra of the compounds from Fig. 1.2, as 20 µM toluene solutions at room temperature, normalized at 310 nm. b) Normalized steady-state emission spectra of the compounds in toluene (20 µM) at room temperature, 300 nm excitation.

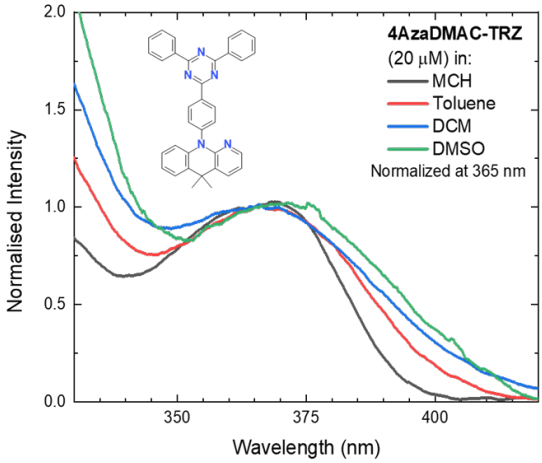

Figure 1.5: Absorption spectrum of 4AzaDMAC-TRZ in different solvents.

of the emission of 4AzaDMAC-TRZ is also confirmed by its clear solvatochromism (Fig. 1.6b), similar to that observed in DMAC-TRZ, but blue-shifted by 309 meV in toluene. An emission band with CT nature is also observed for 4AzaDMAC-DPT and DMAC-DPT, as confirmed by the well pronounced solvatochromism (Figs. 1.6c and 1.6d). As with the TRZ-analogues, the PL of 4AzaDMAC-DPT is blue-shifted compared to DMAC-DPT (312 meV energy difference in toluene, a summary of these emission shifts in different solvents is shown in Tab. 1.1 – the energy difference decreases in polar solvents). This shift indicates that 4AzaDMAC has a weaker donor strength than DMAC, however, the phenyl bridge appears to be decoupled from the donor and not affecting its donor strength, as demonstrated by the almost identical emission spectra of the two molecular fragments, 4AzaDMAC and 4AzaDMAC-Ph, implying that there is marginal extended conjugation into the phenyl bridge.

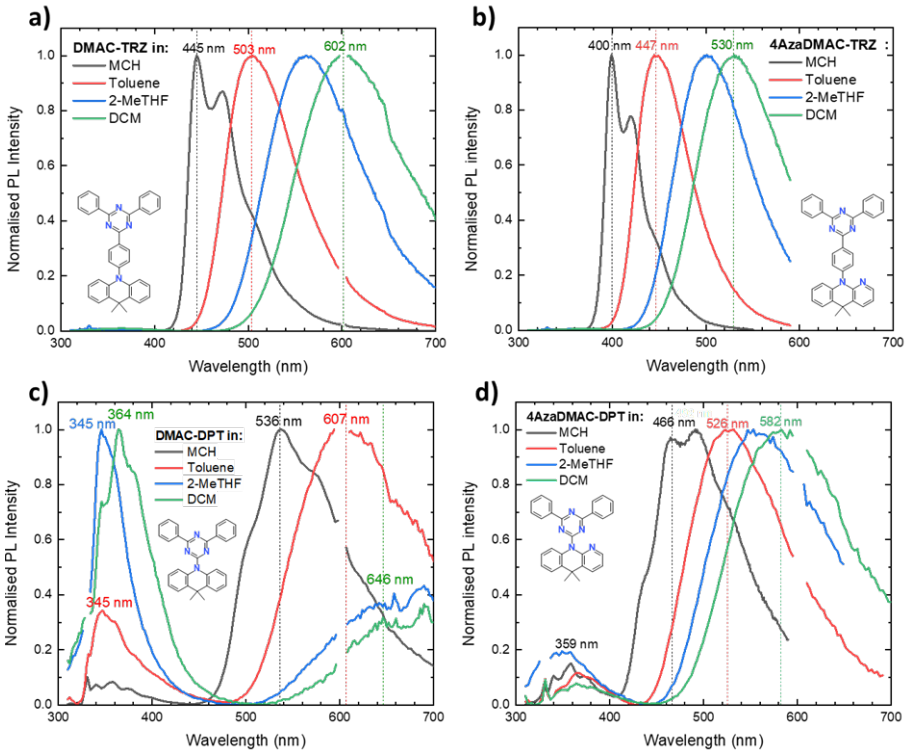

Figure 1.6: Normalized room temperature steady-state emission spectra of a) DMAC-TRZ, b) 4AzaDMAC-TRZ, c) DMAC-DPT, and d) 4AzaDMAC-DPT in a range of different solvents at 20 µM concentration, measured in air ($\lambda_{exc} = 300$ nm).

Emitter	**MCH**		**Toluene**		**2-MeTHF**		**DCM**	
	λ, nm	ΔE, meV	λ, nm	ΔE, meV	λ, nm	ΔE, meV	λ, nm	ΔE, meV
4AzaDMAC-TRZ	400	313	446	309	501	269	530	280
DMAC-TRZ	445		502		562		602	
4AzaDMAC-DPT	466	347	527	312	557	305	582	211
DMAC-DPT	536		607		646		646	

Table 1.1: Emission maximum wavelengths and energy difference between 4AzaDMAC and DMAC series in different solvents.

A large Stokes shift is observed for 4AzaDMAC-DPT and DMAC-DPT, that is explained by the almost undetectable CT absorption band of the two molecules. Indeed, crystallographic data suggest that the two molecules are in the QA conformation, where a large conjugation between the donor and acceptor moieties leads to a large blue-shift of the CT band, as to bury it below (or mix it strongly with) the intense local excitations observed at higher energy. The observation of a CT emission suggests a large conformational rearrangement after photoexcitation with the molecules acquiring a QE conformation, a hypothesis that is nicely confirmed by the computational analysis reported below. This hypothesis would also explain the red-shifted emission observed for 4AzaDMAC-DPT and DMAC-DPT when compared with the -TRZ analogues. In 4AzaDMAC-DPT and DMAC-DPT,the emission (a vertical process) occurs from the QE conformation ending up in a QE conformation of the ground state, corresponding to a high energy state. More puzzling is

the largely decreased intensity of the emission observed for 4AzaDMAC-DPT and DMAC-DPT compared to the parent TRZ-analogues. In particular, in both systems, a residual emission from the localized transition on the donor moieties is seen, due to the very large ratio of the emission probability from the localized state compared to the CT transition[51]. We will address this topic in the computational section.

1.2.3 PLQYs and phosphorescence

Photoluminescence quantum yields (PLQYs) in 20 µM toluene solution ($\Phi_{solution}$) and as 10 wt.% doped films in DPEPO (Φ_{film}) were measured, exciting at 320 and 300 nm respectively (summary of the photophysical performance is given in Tab. 1.2, and the PL spectra of 4AzaDMAC-TRZ and 4AzaDMAC-DPT in DPEPO using $\lambda_{exc} = 300$ nm is shown in Fig. 1.7).

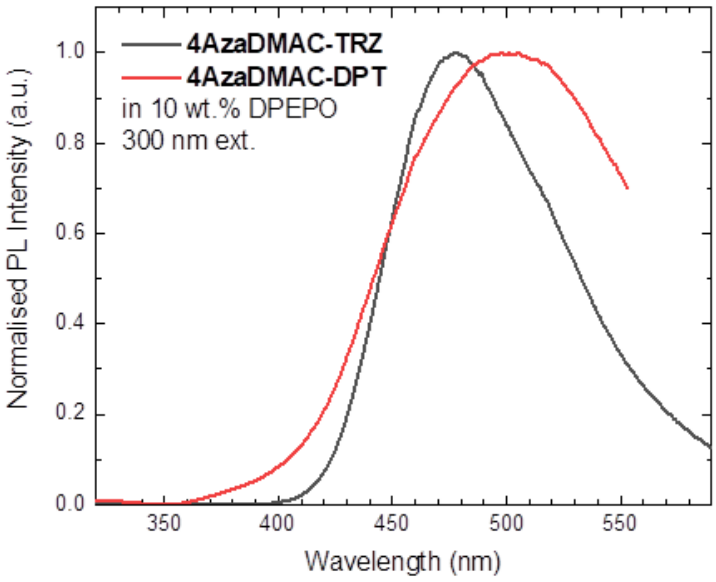

Figure 1.7: Normalized steady-state emission spectra of 4AzaDMAC-TRZ and 4AzaDMAC-DPT in 10 wt.% DPEPO films, $\lambda_{exc} = 300$ nm.

Compound	$\Phi_{solution}$ Ar$^{(a)}$ (air), %	Φ_{film} N$_2^{(b)}$ (air), %	S_1^c, eV	T_1^d, eV
DMAC-TRZ	100 (31)	86 (75)	2.98	2.71
4AzaDMAC-TRZ	85 (54)	84 (66)	3.20	2.87
4AzaDMAC-DPT	20 (6)	17 (13)	3.01	3.16
DMAC-DPT	3.4 (2.7)	7 (6)	3.19	3.03
4AzaDMAC-Ph	-	-	3.63	3.21
4AzaDMAC	-	-	3.63	3.01

Table 1.2: Photophysical properties of the compounds. [a]Measured in 20 µM toluene solution, degassed using argon ($\lambda_{exc} = 320$ nm). The measurement error is ±10%. [b]Measured in 10 wt.% doped films in DPEPO ($\lambda_{exc} = 300$ nm). [c]Measured in 1 wt.% zeonex films at room temperature, steady-state. [d]Measured in zeonex at 80 K temperature, time-resolved (75 ms time delay, 10 ms gate time).

The highest Φ_{film} is seen for DMAC-TRZ (86% in N_2 and 75% in air), with 4AzaDMAC-TRZ having similar Φ_{film} under N_2 (84%), but being more strongly quenched in air (66 %). However, the Φ_{film} of 4AzaDMAC-DPT and DMAC-DPT are much smaller (17% in N_2/13% in air for 4AzaDMAC-DPT and 7% in N_2/6% in air for DMAC-DPT). Similar trends in $\Phi_{solution}$ were observed, DMAC-TRZ and DMBN-TRZ having significantly higher values than their shorter analogues DMAC-DPT and 4AzaDMAC-DPT.

In aerated solution, 4AzaDMAC-TRZ has a higher PLQY than DMAC-TRZ, while showing the opposite trend in degassed solution. This is because, in air, only the prompt emission is effectively measured, while the delayed emission is efficiently quenched by oxygen, therefore, once degassed, the $\Phi_{solution}$ of DMAC-TRZ is higher. Normalized room temperature solid-state emission spectra of all 4AzaDMAC-based compounds in zeonex films show that, much as it occurs in liquid solvents, the 4AzaDMAC-DPT emission is significantly red-shifted if compared with 4AzaDMAC-TRZ, a result that suggests a larger geometrical relaxation upon excitation.

1.2.4 Time-resolved measurements

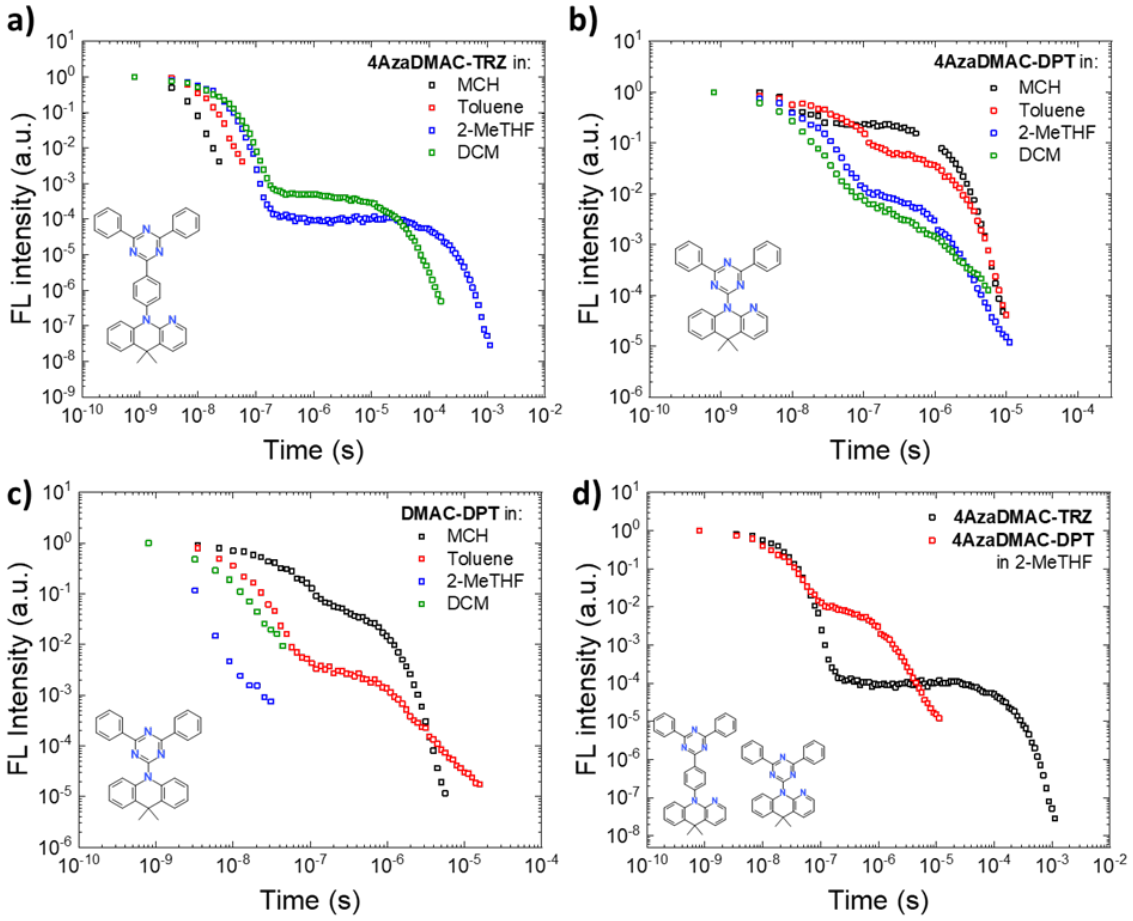

Figure 1.8: Normalized time-resolved photoluminescence decays at room temperature of a) DMBN-TRZ, b) 4AzaDMAC-DPT and c) DMAC-DPT in different solvents (20 µM); d) comparison of 4AzaDMAC-TRZ and 4AzaDMAC-DPT in 2-MeTHF. Measured under vacuum conditions (λ_{exc} = 355 nm).

Time-resolved spectroscopy (TRS) was performed to investigate the time-dependent emission behaviour of the emitters in increasing polarity solvents. Fig. 1.8 shows (in a logarithmic scale) the time evolution of the integrated fluorescence intensity as collected for the four dyes of interest in different solvents. Typically, the first decay of the fluorescence intensity occurs in the nanoseconds time range ($10^{-9} - 10^{-7}s$), due to the de-population of the first singlet excited state by prompt fluorescence. If a pathway for the re-population of the fluorescent state exists, then it is also possible to observe a delayed emission, occurring at longer timescales ($10^{-6} - 10^{-3}s$). Delayed fluorescence is heavily affected both the chemical nature of the dye, as well as by its environment. For 4AzaDMAC-TRZ, delayed fluorescence is not observed in the non-polar solvents methylcyclohexane and toluene, 4AzaDMAC-DPT, on the other hand, shows strong delayed fluorescence in non-polar solvents. Comparing the two emitters, 4AzaDMAC-DPT has a faster delayed emission decay than 4AzaDMAC-TRZ, implying a significantly faster rISC rate and thus a more efficient triplet harvesting. The decay rate constants are given in Tab. 1.3 and the kinetic fitting model of the decays[52] in Fig. 1.9.

Emitter	**Solvent**	$\tau_{\mathbf{prompt}}$ **(ns)**	$\tau_{\mathbf{delayed}}$ **(μs)**	$k_{\mathbf{F}}^{\mathbf{a}} \times 10^7$ **(s^{-1})**	$k_{\mathbf{ISC}}^{\mathbf{b}} \times 10^7$ **(s^{-1})**	$k_{r\mathbf{ISC}}^{\mathbf{b}} \times 10^7$ **(s^{-1})**
4AzaDMAC-TRZ	MCH	3.7	-	27.03	-	-
	Toluene	9.2	-	11	-	-
	2-MeTHF	17	14	5.5	1.6	0.0076
	DCM	22	18	4.6	1.8	0.0084
DMAC-TRZ	Cyclohexane	9.8 [48]	0.08 [48]	10	1.3 [49]	0.0060 [49]
	Toluene	27 [53]	5.5 [53]	1.5 [53]	2.5 [53]	0.051 [53]
	Chloroform	14 [48]	0.12 [48]	6.9	1.8 [49]	0.27 [49]
4AzaDMAC-DPT	MCH	-[c]	1	-	6.6	1.1
	Toluene	81	1.22	1.2	1.5	0.3
	2-MeTHF	20	0.96	5	2.2	0.22
	DCM	14	1.5	7.3	3.1	0.25
DMAC-DPT	MCH	59	0.46	1.7	1.1	0.32
	Toluene	13	0.16	7.8	2.5	0.11
	2-MeTHF	1.4	-	0.69	-	-
	DCM	6.9	-	14.5	-	-

Table 1.3: Summary of rate constants. [a] $k_F = \tau_{prompt}^{-1}$. [b] Calculated using N. Haase et al. method [52]. [c] The prompt emission of 4AzaDMAC-DPT in MCH is too fast to be fitted properly.

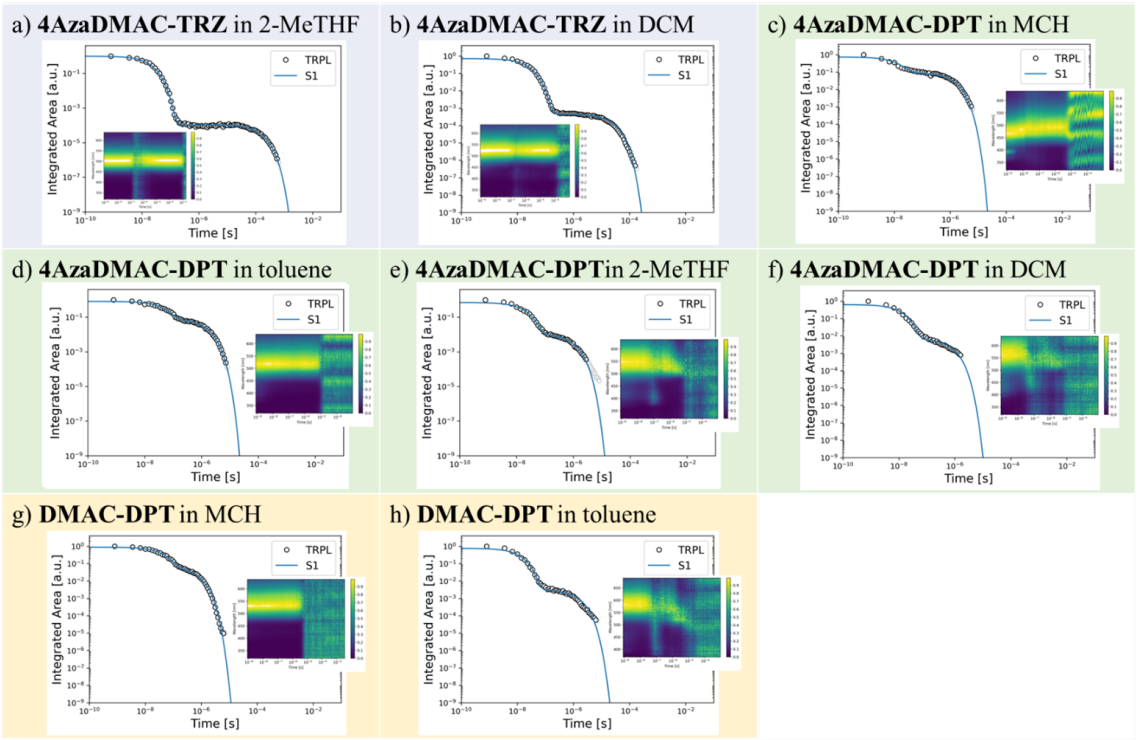

Figure 1.9: Fittings of the decays in different solutions. Insets: contour plots of the measurements; x axis – time, y – wavelength.

Time-resolved decay of DMAC-TRZ in toluene is shown in Fig. 1.10.

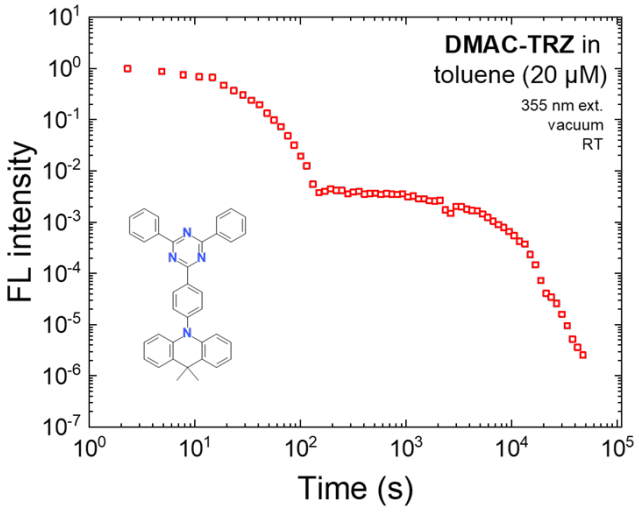

Figure 1.10: Normalized time-resolved photoluminescence decay of DMAC-TRZ in toluene. Measured at room temperature, $\lambda_{exc} = 355\,\text{nm}$.

1.2.5 Computational analysis

All ab-initio calculations are performed using the Gaussian 16 package[54]. Density functional theory (DFT, M06-2X/6-31G(d) level of theory) were performed in gas phase and in selected implicit solvents (Polarizable Continuum Model, hereafter PCM) for the energy minimization in the ground state. Relaxed energy scans for

the ground state were performed with all the coordinates free to relax while scanning the dihedral angle linking the donor to the acceptor groups, as illustrated in Fig. 1.11. Results in Fig. 1.12 and 1.13 demonstrate marginal environmental effects on the ground state geometry. The ground states potential energy surfaces (PES) of the -DPT molecules suggest that only the QA conformation is populated at room temperature, fully in line with the crystallographic data. On the opposite, for the -TRZ counterparts, the QE conformation is the most populated one, even if some amount of a QA (30°) structure could be expected for 4AzaDMAC-TRZ. As for DMAC-TRZ, the possibility of a minor fraction of QA conformation cannot be excluded.

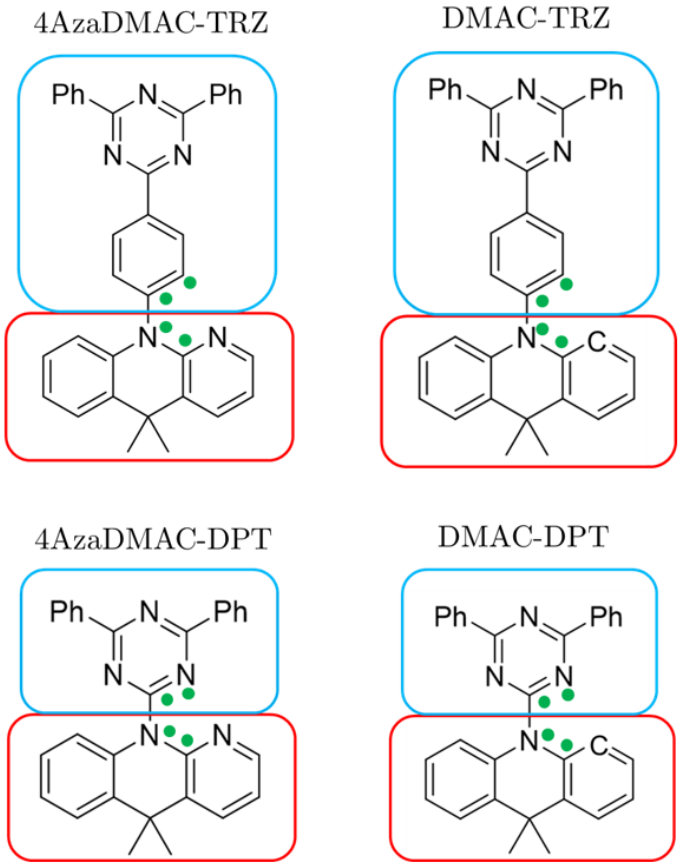

Figure 1.11: The molecular structure of the four molecules considered in this section. The green dots mark the atoms involved in the dihedral angle linking the donor (red box) to the acceptor (cyan box) group.

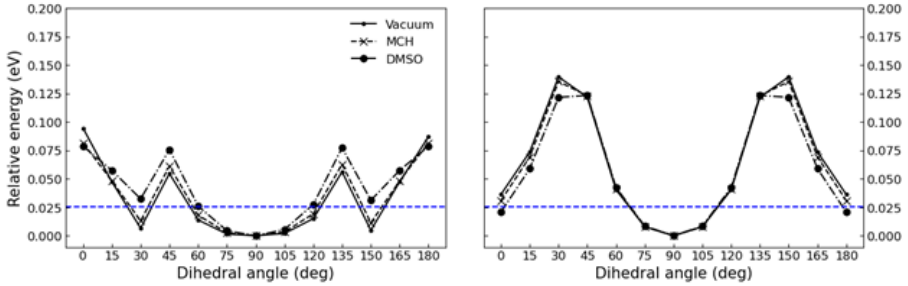

Figure 1.12: The energy scan for 4AzaDMAC-TRZ (left panels) and DMAC-TRZ (right panels). The black curves show the energy of the ground state computed in vacuum (straight line), in Methylcyclohexane (dashed line) and Dimethyl sulfoxide (dash-dotted line). Solvation was treated using the PCM model as implemented in the Gaussian 16 package. The blue dashed line shows the thermal energy at T = 300 K.

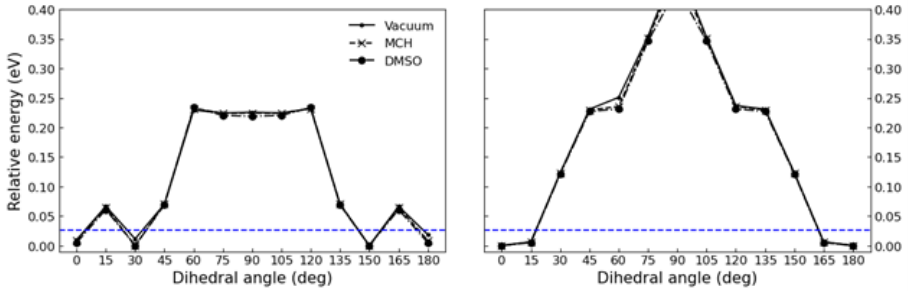

Figure 1.13: The energy scan for 4AzaDMAC-DPT (left panel) and DMAC-DPT (right panels). The black curves show the energy of the ground state computed in vacuum (straight line), in Methylcyclohexane (dashed line) and Dimethyl sulfoxide (dash-dotted line). Solvation was treated using the PCM model as implemented in the Gaussian 16 package. The blue dashed line shows the thermal energy at T = 300 K.

To address the excited states, we make resort to TD-DFT, M06-2X/6-31G(d) level of theory in the Tamm-Dancoff approximation,[48] limiting the attention to the gas-phase results, in view of the limitations of current implementations of implicit solvent models, that are particularly serious when addressing excited states.[55]

Figs. 1.14 and 1.15 show the (gas phase) energy scans for the ground and excited states of the two TRZ-analogues and of the two DPT-analogues, respectively. Fig. 1.15 shows the analogous results for 4AzaDMAC-DPT and DMAC-DPT.

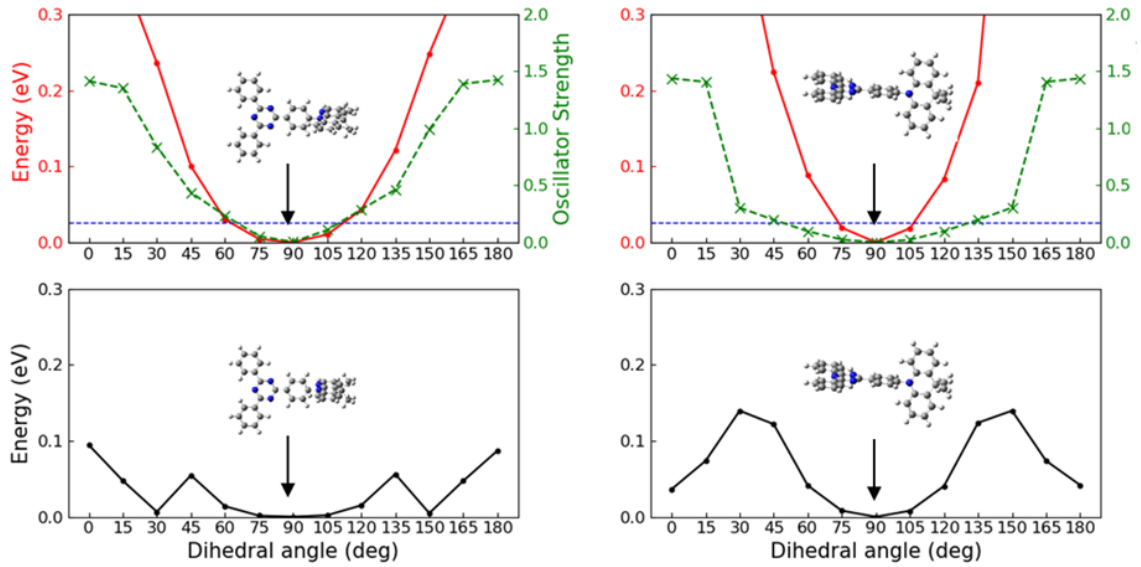

Figure 1.14: Lower panels show the energy of the ground state as a function of the torsional angle (relaxed scan on the ground state geometry). Upper panels show the energy of the lowest excited state (S_1) in red and the corresponding oscillator strength in green. Left and right panels refer to 4AzaDMAC-TRZ and DMAC-TRZ, respectively. In each panel, a sketch of the geometry relevant to the lowest energy configuration is shown.

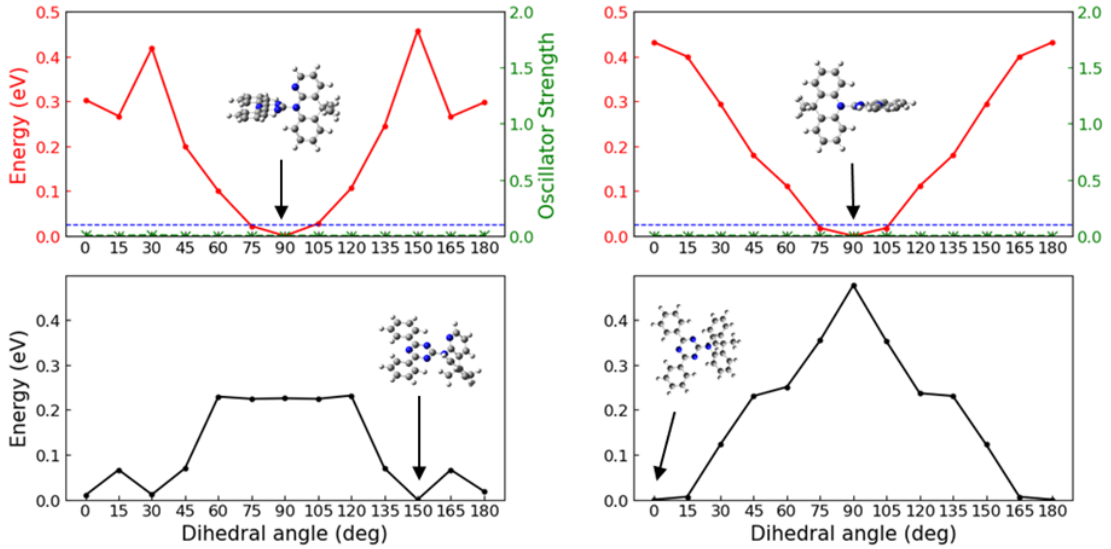

Figure 1.15: Lower panels show the energy of the ground state as a function of the torsional angle (relaxed scan on the ground state geometry). Upper panels show the energy of the lowest excited state (S_1) in red and the corresponding oscillator strength in green. Left and right panels refer to 4AzaDMAC-DPT and DMAC-DPT, respectively. In each panel, a sketch of the geometry relevant to the lowest energy configuration is shown.

Quite interestingly, irrespective of the ground state structures, for all the systems, the excited state is only stable in the QE conformation. This results explains why a CT emission is seen in the -DPT-analogues even if for these dyes the CT absorption is not discernible. We notice that the $\sim$ 0.4-0.5 eV red-shift observed for the emission

when going from 4AzaDMAC-TRZ and DMAC-TRZ to the -DPT analogues roughly agrees with the energy required to deform the ground state of 4AzaDMAC-DPT and DMAC-DPT from the stable QA conformation to the QE conformation.

Emitter	**Vertical absorption**			**Vertical emission**		
	ΔE **(eV)**	λ **(nm)**	f_{osc}	ΔE **(eV)**	λ **(nm)**	f_{osc}
4AzaDMAC-TRZ	3.88	319	0.0003	3.38	366	0.0032
DMAC-TRZ	3.45	359	0	2.96	418	0
4AzaDMAC-DPT	4.52	274	0.015	2.92	424	0.0016
DMAC-DPT	4.36	285	0.0109	2.79	443	0.065

Table 1.4: Gas phase TD-DFT results. Transition energies and oscillator strengths for the lowest energy transition. Absorption data refer to the ground state equilibrium geometry, emission data to the S_1 equilibrium geometry.

Table 1.4 summarizes the transition energies and oscillator strengths calculated for the absorption and emission processes of the four compounds. All the molecules have essentially vanishing oscillator strength both in absorption and emission. Indeed, for 4AzaDMAC-TRZ and DMAC-TRZ. the lowest energy transition has a clear CT character (Fig. 1.16), both in absorption and emission, in line with negligible oscillator strengths. As it will be discussed below, the experimental observation of CT absorption and emission bands in these systems is related to the conformational disorder.

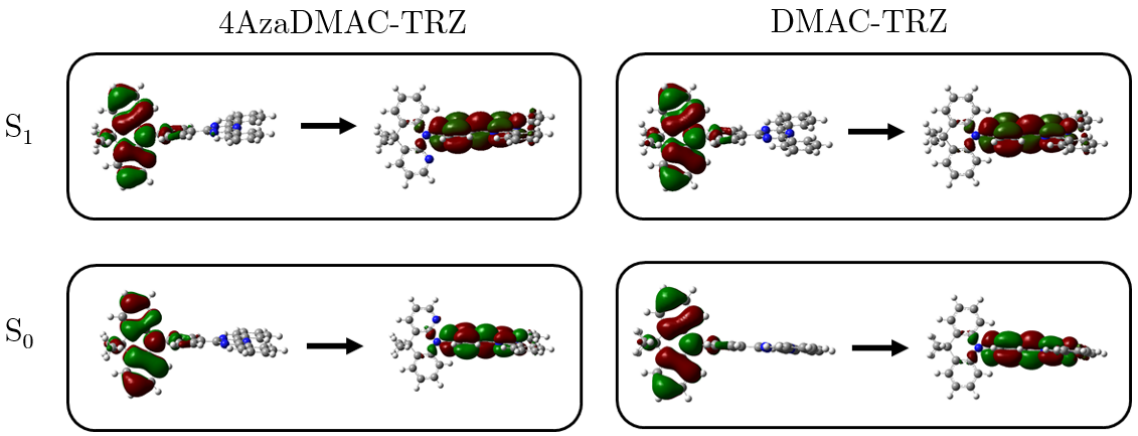

Figure 1.16: Natural transition orbitals (NTOs) of the first excited singlet state computed at the ground state (lower panel) and excited states geometry (upper panel) for the 4AzaDMAC-TRZ (left plots) and DMAC-TRZ (right plots).

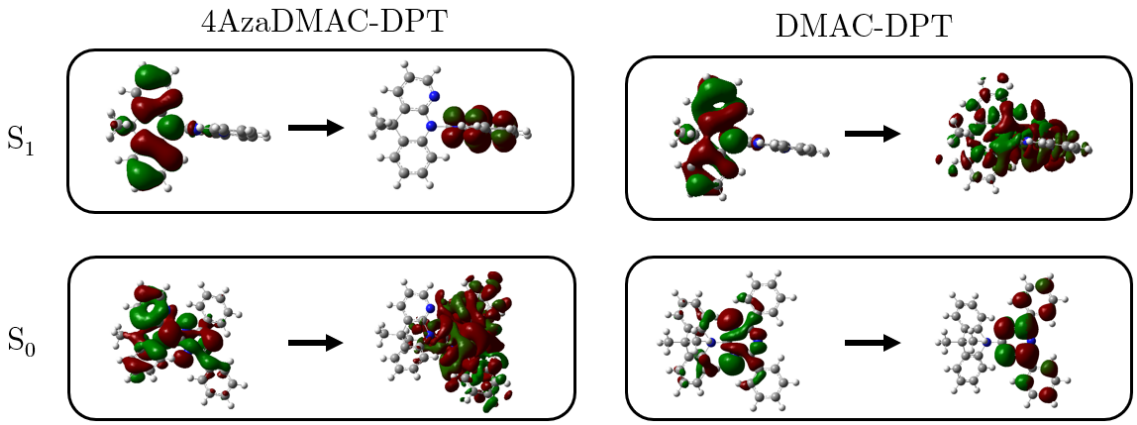

Figure 1.17: Natural transition orbitals (NTOs) of the first excited singlet state computed at the ground state (lower panel) and excited states geometry (upper panel) for the 4AzaDMAC-DPT (left plots) and DMAC-DPT (right plots). For some transitions the NTOs are difficult to visualize as a result of the nature of the transition that involves a mixture of CT and LE transitions.

The transition of 4AzaDMAC-TRZ is slightly blue-shifted if compared with DMAC-TRZ, since 4AzaDMAC has a weaker donating character than DMAC, as expected and in line with the experiment. This is confirmed by data in Tab. 1.5, showing the energies of HOMO and LUMO for the four emitters, calculated in the QE conformation. In this conformation, the conjugation between the donor and acceptor moieties is broken and the HOMO and LUMO energies are a reliable proxy for the donating/accepting character of the two fragments, respectively. The data also confirm that the phenyl ring does not significantly alter the donor/acceptor character of the two molecular moieties.

Emitter	**HOMO (eV)**	**LUMO (eV)**
4AzaDMAC-TRZ	-0.235	-0.037
DMAC-TRZ	-0.226	-0.042
4AzaDMAC-DPT	-0.237	-0.037
DMAC-DPT	-0.218	-0.046

Table 1.5: HOMO and LUMO energies of the emitters.

For the DPT-counterparts, the lowest absorption band is located at much higher energy than for the TRZ-analogues, a result that cannot be ascribed to the different nature of the donor or acceptor groups, indeed the HOMO and LUMO energies in Tab. 1.5 are essentially the same for the two families of molecules. What makes the difference is the different ground state conformation of the DPT-analogues when compared to the TRZ-counterparts. In the QA conformation, characteristic of the short molecules, a stronger conjugation between the donor and acceptor groups moves the CT state at higher energy and the corresponding transition is buried in the UV bands associated with the LE states. For these emitters, the S_1 state has a mixed CT and LE nature. In the excited state, instead, the QE conformation effectively breaks the conjugation relaxing the CT state to lower energies: the S_1 state, relevant to emission, has a clear CT character (c.f. Figs. 1.16 and 1.17).

The experimental shapes of the fluorescence bands confirm a marginal structural rearrangement upon photoexcitation for both 4AzaDMAC-TRZ and DMAC-TRZ, whose vibronic progression is dominated by the 0-0 band. The emission band shape of the short counterparts is more complex, in line with a large conformational rearrangement upon photoexcitation. This rearrangement is also responsible for the considerable redshift of the emission in the short dyes: in these systems, the emission process indeed ends in a highly destabilized vertical QE ground state.

The CT absorption bands in 4AzaDMAC-TRZ and DMAC-TRZ are calculated at slightly higher energies than experimentally observed, an issue that can be ascribed to solvation effects, as discussed below. More striking is the vanishing oscillator strength associated with these transitions, that are instead clearly seen experimentally, even though they have weak intensities. As discussed in Ref. [48] and as is clear from data in Fig. 1.14, at room temperature, a distribution of conformations with slightly different torsional angles around the equilibrium QE geometry is populated: as soon as the dihedral angle deviates from orthogonality, the conjugation between the donor and acceptor moieties is turned on, giving sizable, though still small, oscillator strength to the CT transition. An analogous reasoning applies to the emission intensity.

As for the DPT counterparts, the situation is qualitatively different. As discussed above, the CT absorption is not seen due to the QA conformation of the ground state. The weaker emission of the two DPT-based dyes compared to the TRZ-analogues can be understood from the data in Fig. 1.15. Indeed, the calculated oscillator strength of the lowest energy transition is negligible for these dyes for all the values of the dihedral angle. Accordingly, conformational disorder cannot induce any significant emission intensity.

This unexpected result is related to the symmetry of the relevant orbitals. Specifically, Fig. 1.18 shows the MO contributing to the $S_0 \rightarrow S_1$ transition for the four molecules in a quasi-planar structure where the TRZ-derivatives have a sizable oscillator strength, while the DPT-counterparts have a negligible oscillator strength. The figure unambiguously demonstrates the important role of the phenyl bridge in allowing the communication between the two molecular moieties. With reference to the main molecular axis, the orbitals that most contribute to the transition have the same symmetry, then allowing for a sizable transition dipole moment. On the opposite, for the DPT-molecules, the relevant orbitals have a different symmetry, leading to a negligible oscillator strength.

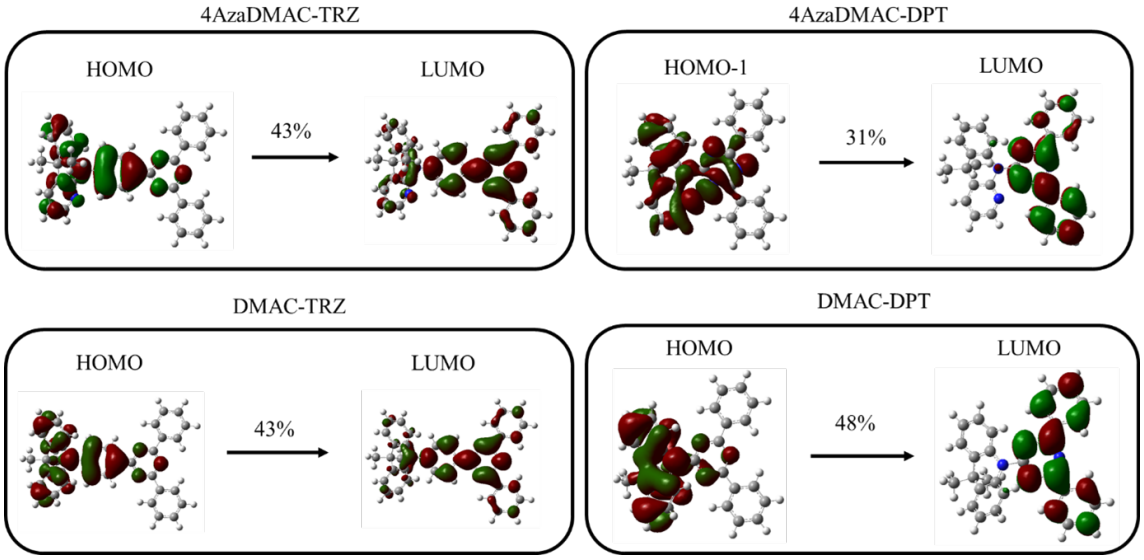

Figure 1.18: The MO that mostly contribute to the $S_0 \rightarrow S_1$ transition as obtained for the four molecules of interest in the QA conformation.

1.2.6 Understanding the role of the solvent

Computational results in the gas phase offer useful clues about the behavior of the molecules of interest, rationalizing the qualitatively different spectral properties of 4AzaDMAC-TRZ and DMAC-TRZ when compared to their DPT-counterparts. However, addressing solvent effects is important to shed light on the TADF behavior and its dependence on the solvent polarity. Current implementation of implicit solvation models[55] poorly address solvation phenomena related to the polarizability of solvent molecules, as described by the medium refractive index, η. The relevant solvent degrees of freedom, related to the electronic polarizability, are indeed faster than the relevant degrees of freedom of the solute, therefore we address them in the antiadiabatic approximation.[55] On the opposite, polar solvation, related to the slow orientational motion of polar solvent molecules, and related to the static dielectric constant, ϵ_{st}, is dealt with in the adiabatic approximation. Following Ref. [48] (see Appendix A for the derivation) the Hamiltonian for the embedded molecule reads:

$$\hat{H}_{tot} = \hat{H}_{el} - \frac{1}{2} r_{el} \hat{\mu}^2 - \hat{\mu} F_{or} + \frac{F_{or}^2}{2 r_{or}} \tag{1.1}$$

where $\hat{H}_{el}$ is the gas phase electronic Hamiltonian and $\hat{\mu}$ is the electric dipole moment operator. The second term accounts for the fast solvation correction. The r_{el} constant is approximated, in the simplifying hypothesis of a spherical solvent cavity hosting the solute, in terms of the solvent refractive index and of the radius of the cavity, a, as follows:

$$r_{el} = \frac{1}{2\pi\epsilon_0 a^3} \left[\frac{\eta^2 - 1}{2\eta^2 + 1} \right] \tag{1.2}$$

The third term in the Hamiltonian describes the interaction of the molecule with the orientational reaction field, F_{or}, the electric field generated by the polar solvent molecules surrounding the solute. Finally, the last term measures the elastic energy

associated to the orientational field, with the constant r_{or} defined as:

$$r_{or} = \frac{1}{2\pi\epsilon_0 a^3}\left[\frac{\epsilon_{st}-1}{2\epsilon_{st}+1} - \frac{\eta^2-1}{2\eta^2+1}\right] \tag{1.3}$$

For each geometry, as relevant to the S_0, T_1 and S_1 states, we diagonalize the electronic Hamiltonian and exploit Multiwfn[56] (version 3.8) to calculate the full matrix associated with the dipole moment operator accounting for excited states up to 7 eV. Following the approach described in Appendix A, we obtain the vertical and adiabatic energies of the relevant states in different solvents. The adopted values of the solvent refractive index and static dielectric constant are listed in Tab. 1.6 and the radius of the cavity is evaluated (in Gaussian 16) as the radius corresponding to a volume inside a contour of 0.001 electrons $\cdot$ Bohr^{-3} density plus 0.5 Å.

Solvent	$\boldsymbol{\eta}$	$\boldsymbol{\varepsilon}_{\mathrm{st}}$
Gas phase	1.000	1.000
MCH	1.423	2.02
Toluene	1.4969	2.38
2-MeTHF	1.407	7.0
DCM	1.4242	8.93

Table 1.6: Refractive index and dielectric constant of the solvents considered in the computations.

4AzaDMAC-TRZ $a = 6.4$ Å			
	λ_{abs} (nm)	λ_{emi} (nm)	ΔE_{ST} (eV)
Gas phase	319	361	0.74
MCH	356	398	0.48
PhMe	362	410	0.42
2-MeTHF	357	534	0.16
DCM	359	556	0.13

DMAC-TRZ $a = 6.2$ Å			
	λ_{abs} (nm)	λ_{emi} (nm)	ΔE_{ST} (eV)
Gas phase	359	418	0.24
MCH	400	469	0.04
PhMe	406	487	0.01
2-MeTHF	391	740	-0.18
DCM	392	796	-0.20

4AzaDMAC-DPT $a = 6.2$ Å			
	λ_{abs} (nm)	λ_{emi} (nm)	ΔE_{ST} (eV)
Gas phase	274	424	0.19
MCH	285	466	-0.073
PhMe	286	478	-0.12
2-MeTHF	287	582	-0.29
DCM	287	596	-0.31

DMAC-DPT $a = 6.1$ Å			
	λ_{abs} (nm)	λ_{emi} (nm)	ΔE_{ST} (eV)
Gas phase	349	465	0.18
MCH	358	481	0.28
PhMe	359	486	0.29
2-MeTHF	356	533	0.33
DCM	356	538	0.33

Table 1.7: Calculated solvent-dependent transition energies and singlet-triplet gap for the four systems considered in the paper.

As expected, the solvent polarity has marginal effects on the position of the absorption band, but when going from the gas phase to non-polar solvents a large redshift is

observed, improving the agreement with the experimental data. As for the emission data, going from gas phase to non-polar solvent leads to a large red-shift, bringing calculated and experimental results in good agreement for both 4AzaDMAC-TRZ, DMAC-TRZ and their DPT-counterparts. More interestingly, the adopted solvation model captures the solvatochromism of the four emitters, whose fluorescence emission shows a progressive red-shift with increasing solvent polarity.

Reliable estimates of the ΔE_{ST} gap are difficult. Indeed, TD-DFT estimate of the excited singlets and even more excited triplets energies are large, leading to uncertainties that are easily larger than the ST energy gap. However, the 4AzaDMAC-TRZ has a fairly large ST gap in gas phase and in non-polar solvents, hindering TADF. The gap decreases in polar solvents, favoring TADF. 4AzaDMAC-DPT is characterized by a small ΔE_{ST} even in the gas phase, that further decreases in polar solvent, suggesting TADF behavior in all solvents, as experimentally observed. The behaviour of DMAC-TRZ is similar to that of 4AzaDMAC-TRZ, while for 4AzaDMAC-TRZ the situation is qualitatively different, with a small ST gap in gas phase that increases with solvent polarity, qualitatively in line with the observation of TADF in non-polar and mildly polar environments.

1.2.7 Conclusions

The phenylene bridging unit significantly affects the photophysics of the investigated compounds: compared to the TRZ-analogues, there is no CT absorption band for the DPT-analogues, that also show a weak and redshifted emission. As for the absorption, the qualitatively different behavior of the TRZ- vs the DPT-based dyes is related to the different ground state geometry: in the TRZ-molecules, the QE conformation dominates, ensuring a low-energy CT state with negligible oscillator strength at the equilibrium conformation. However, the thermally-induced conformational disorder is responsible for the weak observed CT absorption band. In contrast, the QA conformation of the DPT-analogues in the ground state moves the CT state high in energy, so that it is buried below and mixed with local excited state absorption. Interestingly, our computational results show that after photoexcitation, all the studied molecules adopt a QE conformation, explaining the observation of a CT emission in all dyes. The large geometric relaxation that accompanies photoemission in the DPT-analogues explains the observed large Stokes shifts for these molecules as well as the much red-shifted emission of the DTP-analogues compared to those of the TRZ-analogues.

The calculated oscillator strengths at the QA geometry are all vanishingly small, as expected due to the poor conjugation of the D and A fragments in this geometry. The observation of small yet finite absorption and emission bands for the TRZ-analogues is explained by thermal disorder. Specifically, at finite temperature, a distribution of states is populated with the dihedral angle spreading around the equilibrium value. These states have a finite oscillator strength and then contribute to the observed small but finite absorption and emission intensities. Our calculations also explain a puzzling experimental result: the largely suppressed emission intensity of the DPT-analogues compared to the TRZ-analogues. Indeed, the symmetry of the orbital involved in the CT transition results in a negligible oscillator strength for the DPT–based molecules across all dihedral angles, so that, in these molecules, thermal disorder is very less effective in increasing the emission intensity.

Solvation effects on the transition energies are very well addressed in the adopted computational approach, which introducing electronic solvation in an antiadiabatic approach, overcomes the limitations of current implementation of implicit solvation models.[55] The estimates of the singlet-triplet energy gap are more delicate, due to the several sources of uncertainties. On one side, the geometry of the triplet state and hence its energy are hard to fix. Solvation effects are similarly difficult to estimate. More generally, sizable uncertainties on the calculated singlet and triplet energy sum up leading to uncertainties that are often as large as the tiny gap that we would like to estimate.[57]

1.3 Structure-property relationships of thermally activated delayed fluorescent dyes

In the framework of a collaboration with Prof. Hironori Kaji (Kyoto University), we conducted a detailed study on the molecules reported in Fig. 1.19. The photophysics of the prototypical TADF dye, DMAC-TRZ (shown in the center of the figure) is well understood.[48, 49] Starting from this structure, Prof. Kaji designed and synthesized four different molecules, where either the donor or the acceptor fragments are decorated with different side groups. Specifically, the DMAC donor is substituted with 10H-spiro[acridine-9,9'-fluorene] (FA) or 9,9-diphenyl-9,10-dihydroacridine (PA) and the TRZ acceptor with 2,4-di-(adamantan-1-yl)-6-phenyl-1,3,5-triazine (TA) and 2-phenyl-1,3,5-triazine (TH). A joint theoretical and experimental study is undertaken to understand how the conformational degrees of freedom associated with peripheral groups, seemingly marginally involved in the TADF process, may indeed largely affect the delicate TADF photophysics.

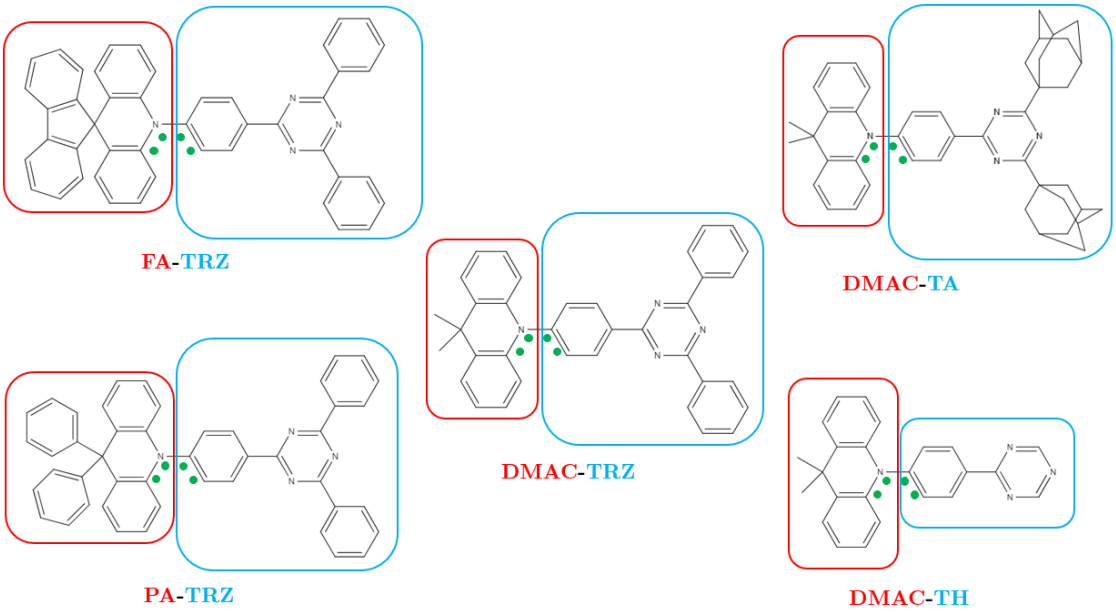

Figure 1.19: The structures of the molecules discussed in this section. The green dots mark the four atom that in each molecule define the dihedral angle of interest.

1.3.1 Spectroscopic characterization

UV-Vis absorption spectra, fluorescence spectra and lifetime decay measurements were recorded for the different compounds dissolved in cyclohexane, toluene and chloroform. In order to avoid inner filter effects in fluorescence spectra, solutions were prepared with absorbance less than 0.1. Absorbance and fluorescence spectra were acquired using a quartz cuvette with an optical path length of 1 cm. The fluorescence quantum yields were determined vs quinine sulfate dissolved in a 0.05 M H_2SO_4 solution as reference ($\phi_f = 0.55$ as reported in ref. [58]), and the results obtained are reported in Tab. 1.8. Two complementary techniques were employed

to analyze the excited states dynamics over a 200 µs time scale. For the initial decay phase, the Time-Correlated Single Photon Counting (TCSPC) technique was utilized with a laser pulse period of 2 µs. For the intermediate time scale, the same technique was applied with an extended laser pulse period of 20 µs. To capture longer time scales, the Multi-Channel Scaling (MCS) technique was adopted, using a laser pulse period of 200 µs.

	Cyclohexane	**Toluene**	**Chloroform**
DMAC-TRZ	0.22	0.18	0.23
PA-TRZ	0.20	0.21	0.17

Table 1.8: Photoluminescence quantum yields for DMAC-TRZ and PA-TRZ in different solvents.

Fig. 1.20 collects absorption and fluorescence spectra of FA-TRZ, PA-TRZ, DMAC-TA and DMAC-TH dissolved in cyclohexane, toluene, and chloroform (spectra of DMAC-TRZ can be found in Ref. [48]). The main spectroscopic features are listed in Tab. 1.9.

Steady-state spectra of the four dyes are qualitatively similar to those of the parent DMAC-TRZ molecule. All the dyes show a non-solvatochromic absorption band and a strongly solvatochromic emission, as expected for dyes with a largely neutral ground state.[42, 50] DMAC-TH is a much smaller molecule than all other systems: the smaller cavity dimension explains the larger emission solvatochromism observed for this dye when compared to the other species.

Molecule	λ_{max}^{abs} (nm)	λ_{max}^{em} (nm)	ϕ
FA-TRZ	397	484	0.21
PA-TRZ	382	477	0.21
DMAC-TRZ*	382	510	0.18
DMAC-TA	368	473	0.19
DMAC-TH	372	525	0.12

Table 1.9: Spectroscopic data in non-degassed toluene. *From Ref. [48].

The most significant deviation from the well-known behavior of DMAC-TRZ is observed for DMAC-TH whose absorption spectrum in cyclohexane shows, apart from the main peak (at $\sim$ 368 nm) an additional feature at 397 nm. This feature is also seen in toluene, even if it is less prominent, and in toluene and to a lesser extent in DMAC-TA in cyclohexane. To understand the origin of this secondary absorption band, fluorescence, fluorescence excitation and fluorescence anisotropy spectra were collected in glassy 2MeTHF at 77 K (Fig. 1.21). The emission spectrum (black line in Fig. 1.21) shows two well separated peaks. The excitation spectra, collected at the wavelength corresponding to the maxima of the two emission peaks (490 and 395 nm) are distinctively different, demonstrating the presence of two different species in solution that we ascribe to two different conformers. The presence of two conformers for DMAC-TH is also supported by the fluorescence anisotropy spectra

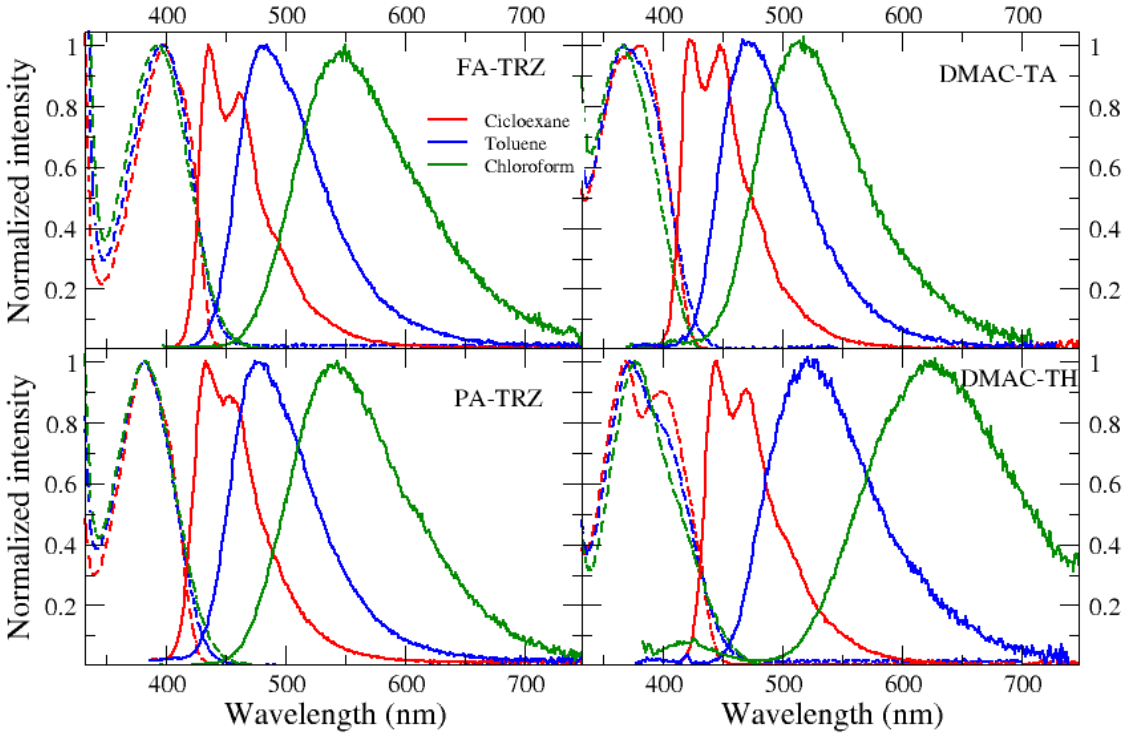

Figure 1.20: Normalized absorbance and fluorescence spectra (dashed and continuous lines, respectively) of the four molecules of interest, collected in cyclohexane, toluene and chloroform.

(Fig. 1.22), that show similar anisotropy values within the excitation band when emission is detected at 395 nm or at 550 nm, as expected for conformers having transitions polarized along the same direction. The presence of two conformers will be confirmed by computational studies, as discussed in the following.

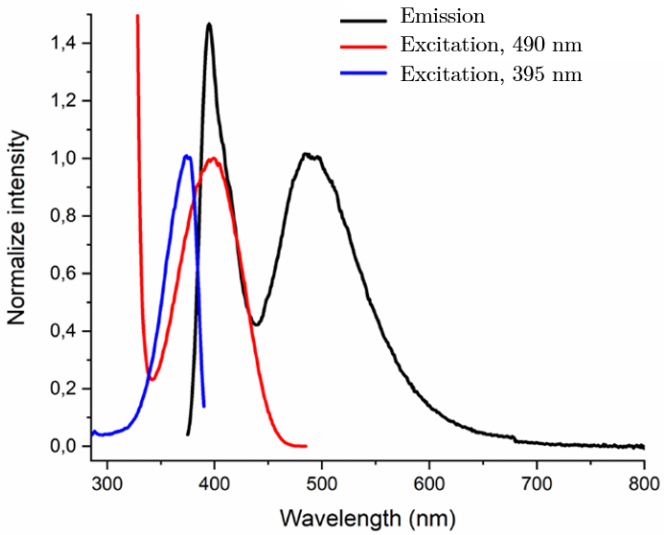

Figure 1.21: Emission and excitation spectra of DMAC-TH in 2MeTHF at 77 K. Black: emission spectrum; Red: excitation spectrum detected at 490nm; Blue: excitation spectrum detected at 395nm.

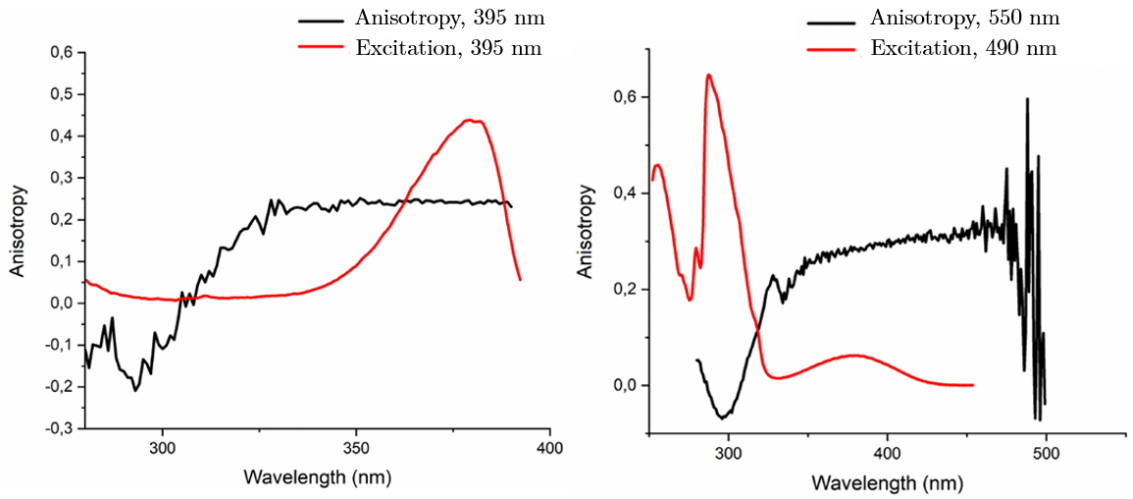

Figure 1.22: Absorption and excitation anisotropy measurements of DMAC-TH at different wavelengths, recorded at 77 K in 2MeTHF.

1.3.2 Computational study

DFT (M062X/6-31g(d)) calculations were performed using Gaussian 16 package[54], both in gas phase and in implicit solvent (PCM) for the five molecules of interest, to address the ground state geometry. The most relevant geometric parameter is the dihedral angle between the donor and the acceptor groups, as illustrated in Fig. 1.19. Therefore, we calculated the ground state energy of the molecules for variable values of the dihedral angle, while relaxing all other coordinates. Relevant results in Fig. 1.23 show that, for all the molecules, much as for DMAC-TRZ[59], the lowest energy minimum corresponds to the orthogonal or quasi-equatorial geometry. With the only exception of FA-TRZ, a quasi-axial conformation for all the compounds is also possible, with marginal variations due to the solvent polarity. However, clear experimental evidence of the presence of the two conformers is found only for DMAC-TH and DMAC-TA in non-polar solvents.
TD-DFT (at the same level of theory) is exploited to address the excited states, limiting the attention to gas-phase results, in view of the limitations of current implementations of implicit solvent models that are particularly serious when addressing excited states.[12, 55, 60] Fig. 1.24 collects results from rigid scans on the four novel molecules, while the results for DMAC-TRZ can be found in Ref.[48].

The excited state PES suggests a very similar situation as for DMAC-TRZ,[48]: for all the system, the S_1 state is stable in a QE conformation (dihedral angle $\sim 90°$), while the T_1 state is slightly distorted, showing two minima at dihedral angle $\sim 60°$ and $120°$. In all cases, at $90°$, the D-A conjugation is lost, leading to degenerate S_1 and T_1 states. Interestingly, for PA-TRZ a second triplet state, T_2, is also quasi degenerate with T_1 and S_1. As for SOC matrix element between T_1 and S_1 again all molecules behave essentially as DMAC-TRZ[48], with vanishing (or almost so) $\langle S_1 | H_{SOC} | T_1 \rangle$ at the equilibrium geometry ($90°$), with the notable exception of PA-TRZ that shows a sizable SOC at the equilibrium geometry. For the sake of comparison, Fig. 1.25 shows the SOC calculated from the relaxed scan. The reason for this anomaly lies in the close proximity of the CT triplet (T_1) with

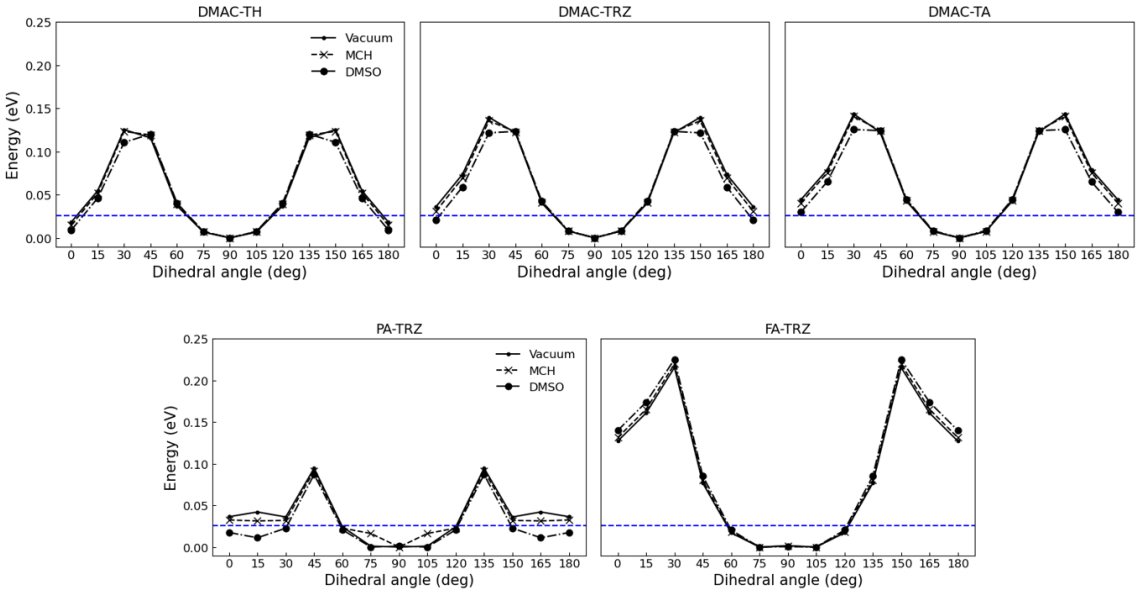

Figure 1.23: The ground state energy calculated as a function of the dihedral angle for DMAC-TH, DMAC-TRZ, DMAC-TA, PA-TRZ and FA-TRZ. Except for the dihedral of interest, all the degrees of freedom are allowed to relax. The blue dashed line defines the thermal energy at room temperature.

a localized triplet (T_2), as shown in Table 1.10. As a result, the two triplet states are largely mixed, leading to enhanced SOC, and this suggests that PA-TRZ can be particularly interesting for TADF applications. Therefore, in the next section, we present a detailed analysis of the time-resolved fluorescence of the PA-TRZ in liquid solvents. For comparison purposes, we also address DMAC-TRZ.

Molecule	$\mathbf{T_1}$	$\mathbf{S_1}$	$\mathbf{T_2}$	$\mathbf{T_3}$	$\mathbf{T_4}$
FA-TRZ	3.50	3.51	3.75	3.78	3.85
MA-TA	3.51	3.52	3.83	3.86	4.03
PA-TRZ	3.69	3.71	3.75	3.97	3.98
MA-TH	3.36	3.36	3.83	3.83	4.04

Table 1.10: Vertical energies (eV) of the five lowest excited states of FA-TRZ, MA-TA, PA-TRZ and MA-TH at the ground state minimum energy geometry.

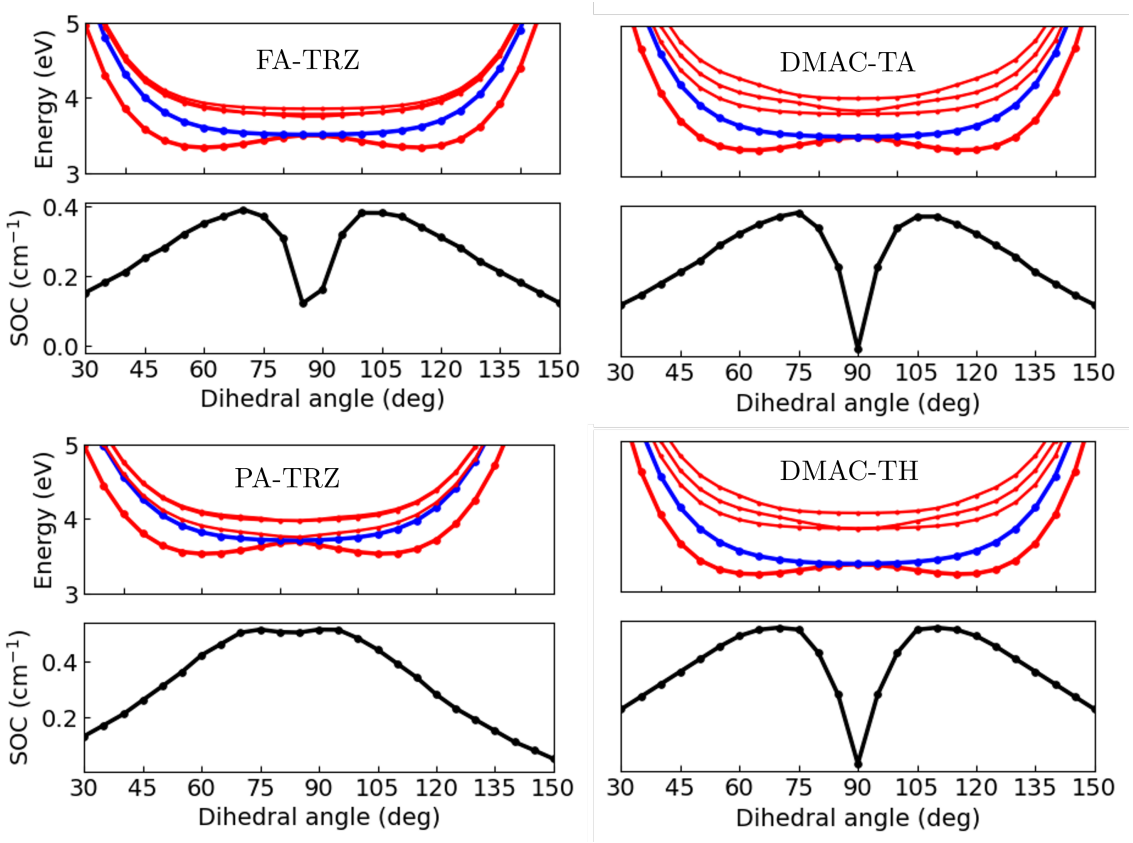

Figure 1.24: The four panels show the results of rigid scan calculations for FA-TRZ, PA-TRZ, DMAC-TA and DMAC-TH. For each molecule, the bottom panel shows the S_1-T_1 SOC and the top panel shows vertical transition energy for the lowest singlet state (S_1, blue trace) and for the four lowest triplet states (red lines).

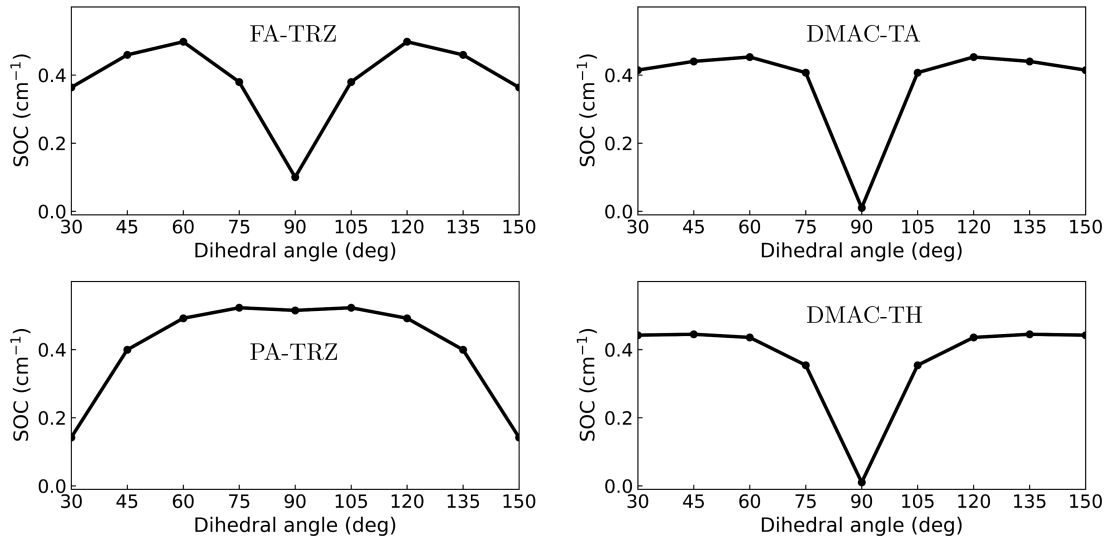

Figure 1.25: The S_1-T_1 SOC computed at the geometries obtained relaxing the ground state geometries of the molecules of interest.

1.3.3 TADF in solution

Fig. 1.26 shows the time evolution of the integrated luminescence intensity measured for DMAC-TRZ and PA-TRZ dissolved in solvents of increasing polarity, cyclohexane, toluene and chloroform. The most obvious difference between the two dyes is seen in cyclohexane, where PA-TRZ hardly shows any TADF behavior.

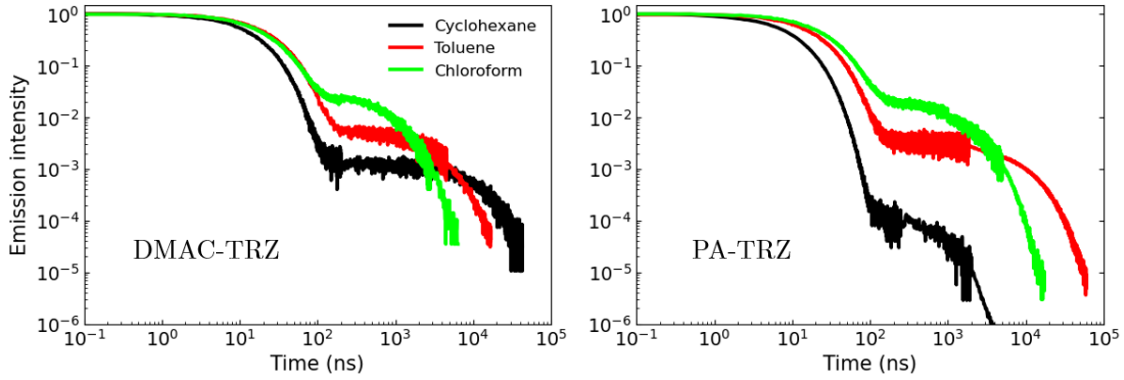

Figure 1.26: Time evolution of the integrated luminescence measured for DMAC-TRZ (left panel) and PA-TRZ (right panel) in three different solvents.

In order to extract the rates relevant to the different processes, a detailed analysis is needed. To start with, the fitting of the emission intensity $I(t)$ as a function of time t is performed, employing a double exponential function:

$$I(t) = A_p \exp(-k_p t) + A_d \exp(-k_d t) \tag{1.4}$$

where A_p and A_d are the pre-exponential factors (we normalize the data by setting $A_p + A_d = 1$), while k_p and k_d are the rates of prompt and delayed emission, respectively. The fitting curves (dashed red lines) are shown in Figs. 1.27 and 1.28 for DMAC-TRZ and PA-TRZ, respectively.

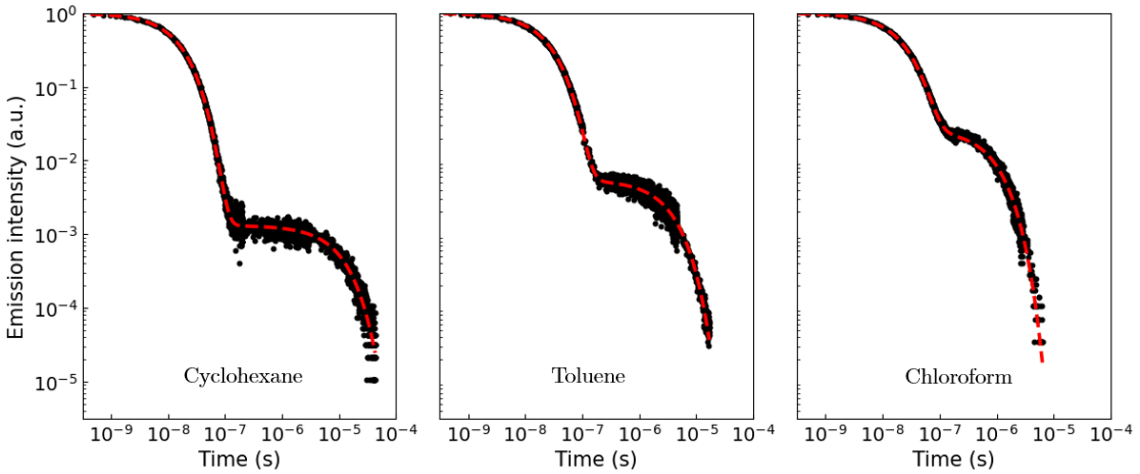

Figure 1.27: Fitting of the emission intensity as a function of time for DMAC-TRZ in different solvents. Black dots and red dashed lines represent the experimental points and the fitted curve, respectively.

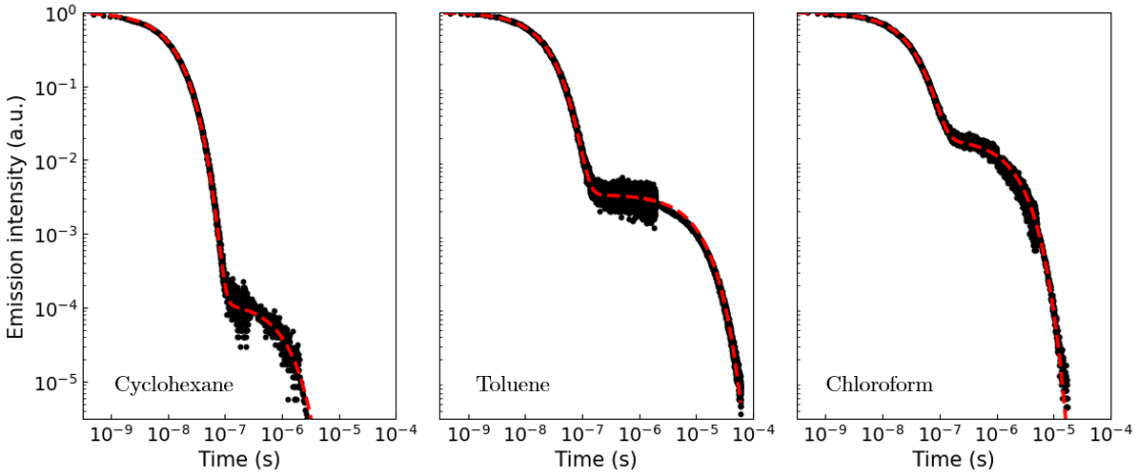

Figure 1.28: Fitting of the emission intensity as a function of time for PA-TRZ in different solvents. Black dots and red dashed lines represent the experimental points and the fitted curve, respectively.

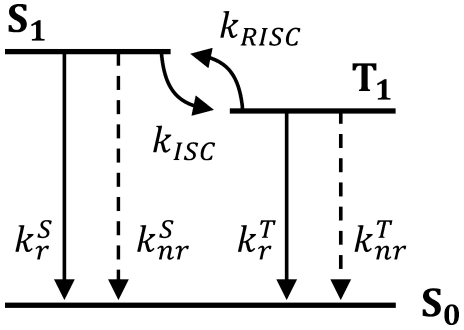

Figure 1.29: Scheme of the photophysical processes for a simple three-state system. Figure adapted from Ref. [61].

	DMAC-TRZ			**PA-TRZ**		
	Cyclohexane	Toluene	Chloroform	Cyclohexane	Toluene	Chloroform
$A_p(\%)$	99.9	99.5	97.3	99.99	99.7	98.0
$A_d(\%)$	0.1	0.05	2.7	0.01	0.3	2.0
$k_p(\mathrm{s}^{-1})$	$6.28 \cdot 10^7$	$3.90 \cdot 10^7$	$4.45 \cdot 10^7$	$9.20 \cdot 10^7$	$4.72 \cdot 10^7$	$3.62 \cdot 10^7$
$k_d(\mathrm{s}^{-1})$	$9.29 \cdot 10^4$	$2.96 \cdot 10^5$	$1.15 \cdot 10^6$	$1.12 \cdot 10^6$	$1.08 \cdot 10^5$	$5.36 \cdot 10^5$

Table 1.11: Results of the double exponential fitting for DMAC-TRZ and PA-TRZ in different solvents.

Tab. 1.11 shows the rates of the different processes, as illustrated in Fig. 1.29, and extracted from the fitting of the curves in Figs. 1.27 and 1.28. Specifically, we adopt the model (entry 2) discussed in Ref. [61], with the following assumptions:

- $k_p \sim k^S$, with $k^S = k_r^S + k_{nr}^S$ measuring the decay rate of the first excited singlet state;
- $R_{DE}^{DF} \approx 1$, where R_{DE}^{DF} is the ratio of the delayed fluorescence vs delayed emission components, it is ~ 1 as long as contributions from the phosphorescence are negligible;

- $\phi_r^S = \phi_{PF} = \frac{k_d(A_p+A_d)}{A_p k_d + A_d k_p}\phi_{PLQY}$, where ϕ_{PF} and ϕ_{PLQY} are the quantum yield of the prompt fluorescence (assumed equal to the quantum yield of the radiative decays of the singlet) and the fluorescence quantum yield, respectively;
- $\phi_{DF} = \frac{A_d(k_p-k_d)}{A_p k_d + A_d k_p}\phi_{PLQY}$, where ϕ_{DF} is the quantum yield of the delayed fluorescence.

With these approximations, the rates of interest are determined by the following set of equations:

$$k_r^S = k_p \phi_{PF} \tag{1.5}$$

$$(k_{nr}^S)^{\max} = k_p \left(1 - \phi_{PF} - \frac{\phi_{DF}}{\phi_{PLQY}}\right) \tag{1.6}$$

$$k_{nr}^T = k_d \left(1 - \frac{\phi_{DF}}{1-\phi_{PF}}\right) \tag{1.7}$$

$$k_{ISC}^{max/min} = \frac{k_p}{2}\frac{\phi_{PLQY}(1-\phi_{PF}) + \phi_{DF} \pm \phi_{PF}(1-\phi_{PLQY})}{\phi_{PLQY}} \tag{1.8}$$

$$k_{rISC}^{max/min} = \frac{k_p}{2}\frac{\phi_{PLQY}(1-\phi_{PF}) + \phi_{DF} \pm \phi_{PF}(1-\phi_{PLQY})}{\phi_{PF}(1-\phi_{PF})} \tag{1.9}$$

where k_r^S and k_{nr}^S are the radiative and non-radiative rates of the first excited singlet state, k_{nr}^T is the non-radiative rate of the first excited triplet state, k_{ISC} and k_{rISC} are the intersystem crossing and the reverse intersystem crossing rates, respectively. The minimum and maximum values of k_{rISC} and k_{ISC} set the relevant error bars. The calculated rates are reported in Tab. 1.12. While in polar solvents similar rISC and ISC rates are estimated for PA-TRZ and DMAC-TRZ, the marginal TADF behavior observed for PA-TRZ in non-polar cyclohexane makes it impossible to extract reliable values for the rates. This result sharply contrasts with the results in Fig. 1.26, that shows a larger SOC for PA-TRZ with respect to DMAC-TRZ and would suggest indeed PA-TRZ as a more efficient TADF dye.

	DMAC-TRZ			**PA-TRZ**		
	Cyclohexane	Toluene	Chloroform	Cyclohexane	Toluene	Chloroform
k_r^S	$7.3 \cdot 10^6$	$4.1 \cdot 10^6$	$5.1 \cdot 10^6$	$1.8 \cdot 10^7$	$4.0 \cdot 10^6$	$2.7 \cdot 10^6$
k_{nr}^S	$2.6 \cdot 10^7$	$1.9 \cdot 10^7$	$1.7 \cdot 10^7$	$7.3 \cdot 10^7$	$1.5 \cdot 10^7$	$1.3 \cdot 10^7$
k_{nr}^T	$8.2 \cdot 10^4$	$2.7 \cdot 10^5$	$1.0 \cdot 10^6$	–	$9.4 \cdot 10^4$	$4.8 \cdot 10^5$
$k_{ISC,max}$	$5.5 \cdot 10^7$	$3.5 \cdot 10^7$	$3.9 \cdot 10^7$	$7.4 \cdot 10^7$	$4.3 \cdot 10^7$	$3.4 \cdot 10^7$
$k_{ISC,min}$	$3.0 \cdot 10^7$	$1.6 \cdot 10^7$	$2.2 \cdot 10^7$	$8.9 \cdot 10^5$	$2.8 \cdot 10^7$	$2.0 \cdot 10^7$
$k_{rISC,max}$	$1.8 \cdot 10^5$	$5.1 \cdot 10^5$	$2.3 \cdot 10^6$	$1.1 \cdot 10^6$	$2.7 \cdot 10^5$	$1.2 \cdot 10^6$
$k_{rISC,min}$	$9.4 \cdot 10^4$	$2.4 \cdot 10^5$	$1.3 \cdot 10^6$	$1.4 \cdot 10^4$	$1.8 \cdot 10^5$	$7.5 \cdot 10^5$

Table 1.12: Experimental rate constants for DMAC-TRZ and PA-TRZ in different solvents.

This inconsistency can be traced back to the flexibility introduced by the two phenyl rings in the PA moiety. As stated above, in the ground state geometry, the phenyl groups introduce several local excited triplet states located in close proximity with

the CT triplet. The resulting mixing explains the large SOC observed in the orthogonal configuration corresponding to the ground state geometry. However, ISC and rISC occur from the S_1 and T_1 states, respectively. The definition of the geometry for the T_1 state of PA-TRZ is non-trivial, since different minima with similar absolute energies are reached depending on the starting geometry, but, as for the S_1 state, we can confidently set the relaxed geometry. As for the main dihedral angle, much as it happens for DMAC-TRZ, it stays in an orthogonal geometry, but, in PA-TRZ, at variance with DMAC-TRZ, other degrees of freedom enter into play, specifically involving the phenyl groups. In the the S_1 state geometry, a rearrangement of the phenyl groups leads to a completely different distribution on triplet state energies, as shown in Fig. 1.30. Concomitantly, the SOC matrix element at the equilibrium geometry for the S_1 state drops down to c.a. 0.05 cm^{-1}.

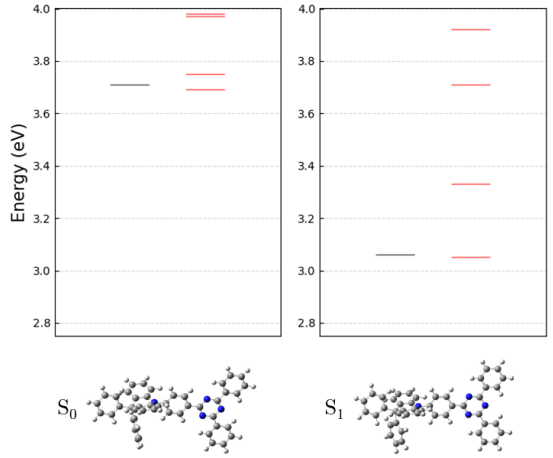

Figure 1.30: Top panels: The absolute energies of S_1 (black) and of the first few triplet states (red) calculated for PA-TRZ at the S_0 and S_1 equilibrium geometries (left and right panel, respectively). Bottom panel, the corresponding geometries.

For a more detailed analysis, the bottom panel of Fig. 1.31 shows the evolution of the S_1-T_1 SOC matrix elements, as obtained in the relaxed scan around the dihedral angle of interest.

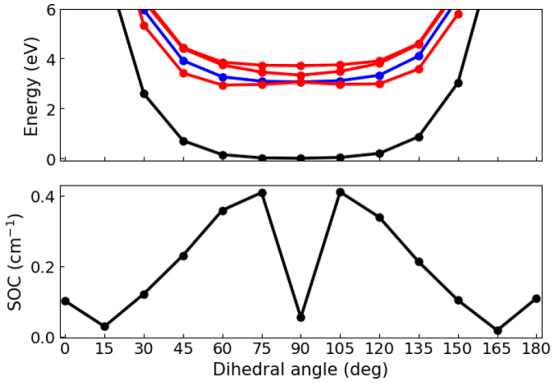

Figure 1.31: Top panel: the energies of the ground state (black) the S_1 state (blue) and the first few triplet states (red) calculated for PA-TRZ as a function of the dihedral angle for the S_1 optimized geometry (rigid scan). Bottom panel: the corresponding SOC matrix element between S_1 and T_1.

The top panel in the same figure shows the corresponding evolution of the ground state energy (black), the S_1 state (blue), and the lowest triplet states (red). The difference with the rigid geometry scan relevant to the ground state (Fig. 1.24 lower left panel) is impressive and brings the PA-TRZ more in line with the DMAC-TRZ. As discussed above, the qualitatively different results obtained for the SOC matrix element in a dihedral angle scan run optimizing the S_0 or the S_1 geometry, as observed in PA-TRZ, is associated with the additional degrees of freedom introduced by the two phenyl substituents. For comparison, Fig. 1.32 shows the S_0 and S_1 scans for DMAC-TRZ, that, as for SOC, show marginal differences.

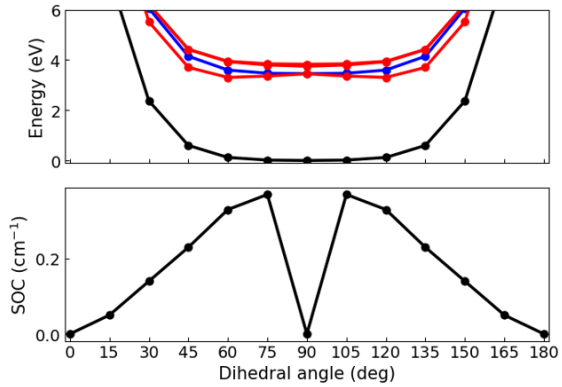

Figure 1.32: Top panel: the energies of the ground state (black) the S_1 state (blue) and the first few triplet states (red) calculated for DMAC-TRZ as a function of the dihedral angle for the S_1 optimized geometry (rigid scan). Bottom panel: the corresponding SOC matrix element between S_1 and T_1.

1.3.4 Discussions and conclusions

TADF is an intriguing but delicate phenomenon that requires a precise energetic alignment of the lowest singlet and triplet states and a sizable SOC. In DA TADF systems, the energy alignment is typically reached by breaking the D-A conjugation as to have the lowest singlet and triplet states with an almost pure CT character. Some degree of conjugation, typically retrieved by some conformational flexibility, is needed to gain whatever tiny oscillator strength, to allow for emission. Local excited triplet states mixed to the CT triplet through relevant conformational degrees of freedom allow for finite SOC. Controlling all these interactions, that are in turn largely affected by the environmental degrees of freedom, is a challenging task.

In this chapter, relying on the detailed understanding reached on the prototypical TADF dye, DMAC-TRZ, we undertook a detailed experimental and theoretical analysis of four related dyes. Out of them, PA-TRZ was singled out for more detailed study due to a comparatively large SOC calculated for the system that suggested this dye as a TADF champion. Experimental results did not confirm this view: PA-TRZ hardly shows TADF behavior in cyclohexane, while, in more polar solvents it behaves like DMAC-TRZ. A more detailed analysis was needed for this system: the two benzene rings, replaced to the methyl groups of the DMAC unit, bring local triplet states close to the CT states, increasing the CT-LE mixing and explaining the large SOC calculated at the ground state equilibrium geometry. However, in the excited state, these flexible units rearrange considerably, effectively decoupling

the local excited triplet states from the CT triplet and reducing the SOC to a tiny value.

The lesson to be learned here is that TADF is a complex phenomenon, with many interactions that must be controlled and accounted for. Among these, the conformational degrees of freedom of the peripheral groups, which are only marginally involved in the main CT process, can significantly alter the delicate interplay between the LE and CT triplets. This interplay is crucial for achieving sizable SOC and, consequently, enabling efficient TADF.

Appendix A

Derivation of the equilibrium Hamiltonian of the solvated system

According to the Hellmann-Feynman theorem, given an eigenstate $|k\rangle$, we can write Eq. 1.1 as

$$\begin{aligned}\frac{\partial E_k}{\partial F_{or}} &= \left\langle \Psi_k \middle| \frac{\partial}{\partial F_{or}} \hat{H}_{tot} \middle| \Psi_k \right\rangle \\ &= \left\langle \Psi_k \middle| \frac{\partial}{\partial F_{or}} \left(\hat{H}_{el} - \tfrac{1}{2} r_{el} \hat{\mu}^2 + \tfrac{F_{or}^2}{2 r_{or}} \hat{I} - \hat{\mu} F_{or} \right) \middle| \Psi_k \right\rangle \\ &= \left\langle \Psi_k \middle| \frac{F_{or}}{r_{or}} \hat{I} - \hat{\mu} \middle| \Psi_k \right\rangle .\end{aligned}$$

where the eigenvalue equation for the total Hamiltonian reads:

$$\hat{H}_{\mathrm{tot}} |k\rangle = E_k |k\rangle. \tag{A.1}$$

At the equilibrium geometry of the k-th state, the derivative $\frac{\partial E_k}{\partial F_{\mathrm{or}}}$ vanishes, so that:

$$\begin{aligned}\left\langle \Psi_k \middle| \frac{F_{\mathrm{or}}}{r_{\mathrm{or}}} \hat{I} - \hat{\mu} \middle| \Psi_k \right\rangle &= 0 \\ \left(\frac{F_{\mathrm{or}}}{r_{\mathrm{or}}} \right)_{\mathrm{eq},k} - \langle \hat{\mu} \rangle_{\mathrm{eq},k} &= 0 \\ F_{\mathrm{or,eq},k} &= \langle \hat{\mu} \rangle_{\mathrm{eq},k} \, r_{\mathrm{or}}\end{aligned} \tag{A.2}$$

The total Hamiltonian corresponding to an equilibrated reaction field for the k-th state can thus be written as:

$$\begin{aligned}\hat{H}_{\mathrm{tot,eq},k} &= \hat{H}_{\mathrm{el}} - \tfrac{1}{2} r_{\mathrm{el}} \hat{\mu}^2 + \langle \hat{\mu} \rangle_{\mathrm{eq},k} \, r_{\mathrm{or}} \left[\tfrac{1}{2} \langle \hat{\mu} \rangle_{\mathrm{eq},k} \hat{I} - \hat{\mu} \right] \\ \hat{H}_{\mathrm{tot,eq},k} &= \hat{H}_{\mathrm{el}} + \sum_j \left[\tfrac{1}{2} \langle \hat{\mu} \rangle_{\mathrm{eq},k,j}^2 \, r_{\mathrm{or}} \hat{I} - \mu_j \langle \hat{\mu} \rangle_{\mathrm{eq},k,j} \, r_{\mathrm{or}} - \tfrac{1}{2} r_{\mathrm{el}} \mu_j^2 \right]\end{aligned} \tag{A.3}$$

where the summation runs over the three cartesian coordinates. Choosing an educated guess for the equilibrium dipole moment $\langle \hat{\mu} \rangle_{\mathrm{eq},k}$ for each of the TADF-interesting states (S_0, S_1 and T_1), we can solve iteratively for the computed permanent dipole moment, $\langle \hat{\mu} \rangle_k = \langle \Psi_k | \hat{\mu} | \Psi_k \rangle$, until convergence is achieved.

Chapter 2

[1]Theoretical estimates of non-radiative rates: basic concepts

2.1 Introduction

In the previous chapter, we have seen that the non-radiative rates, including ISC and rISC rates, are important to define the efficiency of TADF-OLED devices. More generally, the photophysics of molecular systems is governed by the competition between radiative and non-radiative rates.[63, 64] Reliable estimates of non-radiative rates are therefore in demand to understand and possibly control several processes of fundamental and applicative interest including fluorescence, phosphorescence, delayed fluorescence, electroluminescence, etc.[65] Well-established expressions for radiative rates are available,[66] which, relying on the Fermi golden rule (FGR), are conveniently implemented in computational schemes[67–70] to calculate the oscillator strengths of optical transitions, once the energies and the wavefunctions of the relevant states are known.

Non-radiative rates are more delicate and are a central topic in quantum chemistry since the 50's.[71–76] Only in recent years effective computational strategies have been proposed for their estimate.[67, 77–80] The most popular computational approaches to non-radiative rates rely again on the FGR and more precisely on its state-to-state form (ssFGR).[66] A clever transformation of the ssFGR from the frequency to the time domain,[81, 82] leads to closed expressions for a time dependent function, the generating function (GF), that, in the harmonic approximation, allows to account for all vibrational degrees of freedom of a molecular system, without the tedious and computationally demanding task of calculating a very large number of Franck-Condon integrals. However, a very fundamental issue arises here. The ssFGR applies to closed quantum systems, where the energy is strictly conserved. It is therefore perfectly adequate to describe radiative processes where the energy of the global system (matter and radiation) is conserved, or, in other terms, where the energy required for the absorption process or the energy extracted in the emission process is provided from or lent to the radiating field. But, strictly speaking,

[1]This chapter collects the results published in the paper [62], recently published by our research group.

in closed quantum systems, the non-radiative processes can only occur among degenerate states since neither energy sources nor drains are available. Non-radiative transitions between non-degenerate states can only occur in the presence of some mechanisms of energy dissipation. Much as with friction in classical dynamics, these dissipation mechanisms cannot be addressed from first principles, but require some phenomenological models. If large molecules with a very large number of coupled vibrational modes are considered, the issue is somewhat mitigated as the system itself becomes a large reservoir, however, the full equilibration still requires a thermodynamic bath. Strictly speaking, a truly *ab initio* estimate of the non-radiative rates is not possible.

We illustrate this basic but often overlooked concept with reference to the simplest model for non-radiative rates: the displaced harmonic oscillator with a weak and constant coupling between the two states, as to ensure the reliability of the perturbative treatment (underlying the FGR) and of the Condon approximation. In the next section, we introduce the model. Then we shortly review the GF approach in an effort to shed light on the computational strategy that effectively *opens* the closed quantum system described by the ssFGR. We then address the very same problem adopting a truly open quantum system approach, specifically relying on the Redfield approach in the Bloch approximation. We will discuss the basic physics underlying the two approaches, also relying on a blended approach that allows for a direct comparison of the results. Before concluding, we shortly address static disorder.

2.2 The model

The simplest model to address non-radiative transitions accounts for just two diabatic electronic states, dubbed as $|1\rangle$ and $|2\rangle$ (in energy order). N harmonic oscillators are introduced, that, in the approximation of linear electron-vibration coupling, have the same nature and the same frequency in the two states, but displaced minima, as illustrated in Fig. 2.1 for a single mode with frequency ω_j and reorganization energy ϵ_j. We impose the Condon approximation, neglecting the dependence on vibrational coordinates of the matrix element $V = \langle 1|\hat{V}|2\rangle$ that mixes the two diabatic states. The model Hamiltonian reads:

$$\begin{aligned}\hat{H}_0 = &\left[E_{ad} + \sum_{j=1}^{N}\left(\epsilon_j - \sqrt{\hbar\omega_j\epsilon_j}(\hat{a}_j^\dagger + \hat{a}_j)\right)\right]|2\rangle\langle 2| + \\ &+ V\left(|1\rangle\langle 2| + |2\rangle\langle 1|\right) + \sum_{j=1}^{N}\hbar\omega_j\left(\hat{a}_j^\dagger\hat{a}_j + \frac{1}{2}\right)\end{aligned} \tag{2.1}$$

where E_{ad} is the adiabatic energy gap (see Fig. 2.1), and the bosonic creation and annihilation operators are related to the dimensionless coordinate by $\hat{Q}_j = \frac{1}{\sqrt{2}}\left(\hat{a}_j^\dagger + \hat{a}_j\right)$.

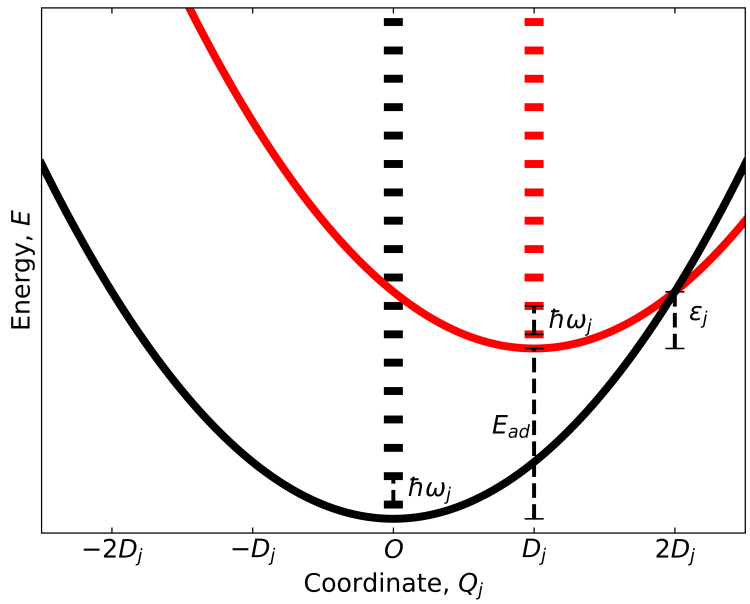

Figure 2.1: Sketch of the potential energy surfaces for the diabatic states $|1\rangle$ (black) and $|2\rangle$ (red), plotted against the vibrational coordinate Q_j. In the linear coupling approximation, the vibrational coordinates and frequencies $\hbar\omega_j$ are the same for the two electronic states, the only difference being the different equilibrium position. The adiabatic energy gap E_{ad} and the vibrational reorganization energy ϵ_j are shown in the figure. On the horizontal axis (arbitrary units), D_j is the displacement of Q_j when going from state $|1\rangle$ to $|2\rangle$. The horizontal lines mark the vibrational eigenstates of the two harmonic oscillators.

2.3 The generating function approach

The GF approach relies on a perturbative treatment of the coupling V, the unperturbed states being simply the product of an electronic state times one of the eigenstates of the relevant harmonic oscillator (centered at $Q_j = 0$ for $|1\rangle$ and at $Q_j = D_j = \sqrt{\frac{2\epsilon_j}{\hbar\omega_j}}$ for $|2\rangle$, see Fig. 2.1). As stated above, the perturbative treatment is reliable when V is small compared to the adiabatic gap. Here we will only explore this regime (when not otherwise specified we set $V = 10^{-4}$ eV). Moreover, we focus mainly on systems with a small adiabatic energy gap, ~ 0.1 eV, as relevant to non-radiative transitions between excited states, including ISC and rISC processes of interest for TADF-OLED applications. The relaxation from an excited to the ground state typically involves much larger gaps, the problem associated with the estimate of relevant rates being discussed in Ref. [83].

An additional hypothesis underlying current implementations of the GF approach is the fast equilibration of the vibrational degrees of freedom in each electronic manifold, so that the rates between the two electronic states are calculated assuming

that the vibrational levels in the initial state manifold ($|2\rangle$ or $|1\rangle$ for the downward or upward transitions, respectively) are populated according to the Boltzmann distribution. In this hypothesis, of course, only comparatively slow processes can be properly described by the GF approach, while the dynamics observed in ultrafast spectroscopy cannot be addressed.

With reference to the simplest case of a single vibrational mode, (the extension to the multimode case is trivial but leads to clumsy expressions), the non-radiative rate is the weighted sum of the rates from each populated vibrational level in the initial states $|I\rangle|l\rangle$ to each vibrational level of the final states $|F\rangle|\tilde{m}\rangle$, where $|I\rangle$ and $|F\rangle$ mark the initial and final electronic states (either $|1\rangle$ or $|2\rangle$), while $|l\rangle$ and $|\tilde{m}\rangle$ are the vibrational states of the harmonic oscillator whose equilibrium geometry corresponds to the initial and final electronic state, respectively. The general rate expression driven by a perturbation with frequency $\omega = E/\hbar$ reads:

$$W_{F\leftarrow I} = \frac{2\pi}{\hbar}|V|^2 \sum_l w_l \sum_m |\langle\tilde{m}|l\rangle|^2 \, \delta\left(E_{F\tilde{m}} - E_{Il} - E\right) \tag{2.2}$$

where the Dirac δ-function ensures energy conservation. Here and in the following, when a single mode is considered, we drop the index j that identifies the mode. For non-radiative transitions, $E = 0$, and only transitions between strictly degenerate $|I\rangle|l\rangle$ and $|F\rangle|\tilde{m}\rangle$ states are allowed. The rate depends on the temperature (set to 300 K in the following), due to the thermal population of the vibrational levels in the initial state:

$$w_l = Z^{-1} \exp\left\{-\left(l + \frac{1}{2}\right)\beta\hbar\omega\right\} \tag{2.3}$$

where the inverse partition function of the harmonic oscillator is

$$Z^{-1} = 1 - \exp\left(-\beta\hbar\omega\right) \tag{2.4}$$

with $\beta = (k_B T)^{-1}$ and k_B the Boltzmann constant. Following the original suggestion from Lax and Kubo,[81, 82] the Fourier transform (FT) of the rate in Eq. 2.2 can be written as follows:

$$\begin{aligned} g_{F\leftarrow I}(t) &= \frac{2\pi|V|^2}{\hbar}\int_{-\infty}^{+\infty}\left[\sum_l w_l \sum_{\tilde{m}} |\langle\tilde{m}|l\rangle|^2 \, \delta\left(E_{F\tilde{m}} - E_{Il} - E\right) e^{-\frac{itE}{\hbar}}\right] dE \\ &= \frac{2\pi|V|^2}{\hbar}\sum_l w_l \sum_{\tilde{m}} |\langle\tilde{m}|l\rangle|^2 \exp\left\{-\frac{it(E_{F\tilde{m}} - E_{Il})}{\hbar}\right\} \end{aligned} \tag{2.5}$$

Exploiting the relation $E_{F\tilde{m}} - E_{Il} = E_{ad} + (m - l)\hbar\omega_j$, one finally gets

$$g_{F\leftarrow I}(t) = \frac{2\pi|V|^2}{\hbar}\exp\left\{-\frac{itE_{ad}}{\hbar}\right\} f(t) \tag{2.6}$$

where $f(t)$ is the FT of the Frank-Condon weighted density of states, the so-called GF:

$$f(t) = \sum_l w_l \sum_{\tilde{m}} |\langle\tilde{m}|l\rangle|^2 \exp\{-it(\tilde{m} - l)\omega\} \tag{2.7}$$

The double summation in Eq. 2.7 is easily calculated for the illustrated case of a single vibrational mode, but when the number of modes increases, the calculation of all Franck-Condon factors $|\langle\tilde{m}|l\rangle|^2$ becomes too computationally demanding. Closed analytical expressions for the time-dependent GF are available for any number of coupled oscillators, accounting for linear and quadratic coupling (*i.e.* accounting for the displacement of the harmonic oscillators as well as for their different frequencies and for the Dushinsky rotation),[70, 79, 84–89] as well as for anharmonic (Morse-like) oscillators.[83] If, as in our case, only linear electron-vibration coupling is accounted for, the general GF expression for the multimode case becomes:

$$f(t) = \prod_{j=1}^{N} \exp\left\{ -\frac{D_j^2}{2} \left(\sinh(it\omega_j) + \coth\left(\frac{\beta\hbar\omega_j}{2}\right)(1 - \cosh(it\omega_j)) \right) \right\} \tag{2.8}$$

The inverse FT of the GF gives the Frank-Condon weighted density of states:

$$F(E) = \frac{1}{2\pi\hbar} \int_{-\infty}^{+\infty} f(t)\, e^{\frac{itE}{\hbar}} dt \tag{2.9}$$

and the transition rates are finally obtained as a function of the adiabatic gap (we dub these functions as *rate-spectra*):

$$W_{1\leftarrow 2}(E_{ad}) = \frac{2\pi}{\hbar}|V|^2 F(E_{ad}) \qquad\qquad W_{2\leftarrow 1}(E_{ad}) = \frac{2\pi}{\hbar}|V|^2 F(-E_{ad}) \tag{2.10}$$

In the general case, when quadratic coupling is taken into account, two different GFs are calculated for the downward and upward transitions, whereas, in the linear coupling approximation, the two GFs coincide.

Figs. 2.2A and 2.3A show the GF calculated for the simplest case of a single coupled mode with a low ($\hbar\omega = 0.024\,\text{eV}$) and a high ($\hbar\omega = 0.12\,\text{eV}$) frequency, respectively. As expected, the GF oscillates in time, with a period matching the vibrational frequency. The rates calculated as a function of the adiabatic gap are obtained from the inverse Fourier transform of the GF. Unavoidably, the inverse FT of the full GF (extending over the whole time-axis), would lead to spiky rate-spectra, recovering the δ functions of the ssFGR and restoring the energy conservation. Non-radiative rates would stay undefined in these conditions, being infinite at the energy conserving points and zero everywhere else. The area below the peaks, the analogous of the oscillator strength for optical transitions, is of course well defined, but it does not correspond to a rate (it has not the proper dimensions), that corresponds instead to the value of the rate-spectrum function calculated at the adiabatic gap.

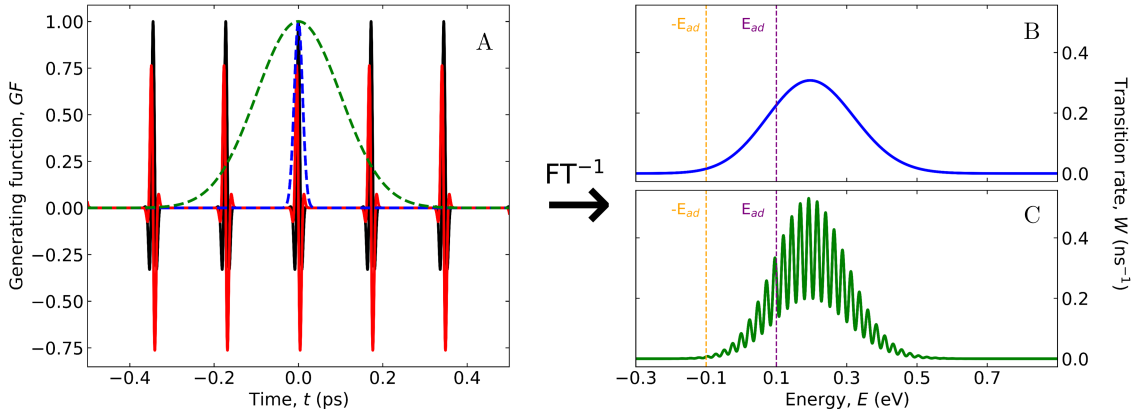

Figure 2.2: Generating function of a single fast mode system $\hbar\omega = 0.024$ eV, $\epsilon = 0.2$ eV versus time. Real and imaginary parts are shown in black and red, respectively. The blue and green dashed lines show two gaussian apodization functions, $t_{r,1} = 10$ fs and $t_{r,2} = 100$ fs, respectively. (B) and (C) show the rates as a function of the energy, calculated with the apodization functions with $t_{r,1}$ and $t_{r,2}$, respectively. The GF in panel A and the resulting rate-spectra in panels B and C apply irrespective of the adiabatic gap. The downward and upward rates are estimated for a specific value of the adiabatic gap from the rate value at $E = E_{ad}$ and $E = -E_{ad}$, respectively, as illustrated in the figure for $E_{ad} = 0.1$ eV with the violet vertical dotted line (downward rate) and the yellow line (upward transition).

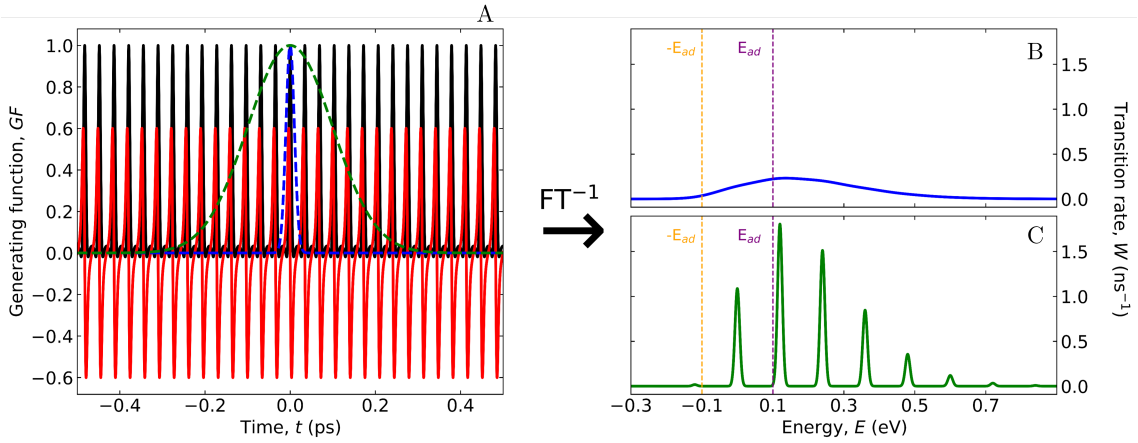

Figure 2.3: Generating function of a single fast mode system $\hbar\omega = 0.12$ eV, $\epsilon = 0.2$ eV versus time. Real and imaginary parts are shown in black and red, respectively. The blue and green dashed lines show two gaussian apodization functions, $t_{r,1} = 10$ fs and $t_{r,2} = 100$ fs, respectively. (B) and (C) show the rates as a function of the energy, calculated with the apodization functions with $t_{r,1}$ and $t_{r,2}$, respectively. The GF in panel A and the resulting rate-spectra in panels B and C apply irrespective of the adiabatic gap. The downward and upward rates are estimated for a specific value of the adiabatic gap from the rate value at $E = E_{ad}$ and $E = -E_{ad}$, respectively, as illustrated in the figure for $E_{ad} = 0.1$ eV with the violet vertical dotted line (downward rate) and the yellow line (upward transition).

To obtain a smoother behavior, and hence meaningful estimates of the rates, the constraint of energy conservation must be released. However, as also discussed in Ref. [83], this crucial step is often not fully appreciated. Typically, the GF is calculated on a finite time interval (usually set to a default value in computational

codes), broadening the δ functions of the ssFGR by an amount proportional to the inverse width of the observation time window, as shown in Fig. 2.4.[90]

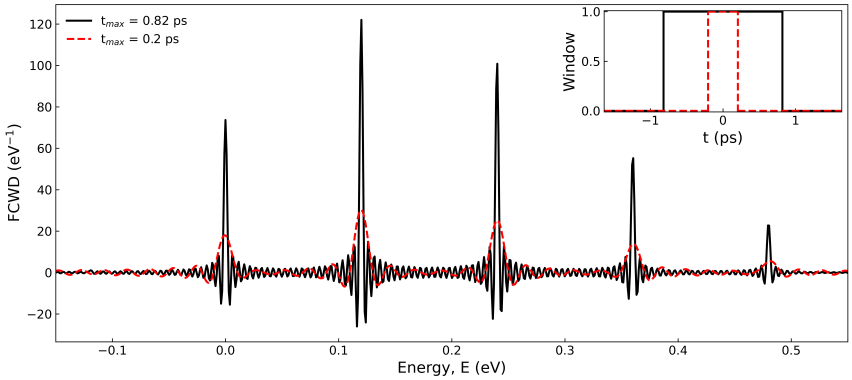

Figure 2.4: Rate spectra computed as the inverse FT of the GF relevant to the system described in Fig. 2.3. The black and red curves refer to results obtained considering two different observation windows (boxcar apodization) with $t_{max} = 0.82\,\text{ps}$ and $t_{max} = 0.233\,\text{ps}$, respectively, as shown in the inset.

The choice of the time interval limits the window within the generating function is observed, playing the role of an effective damping, *opening* in the roughest way the closed quantum system of the ssFGR. It also originates some baseline noise that is reduced using well-designed apodization functions (see Fig. 2.5). Specifically, the sharp edges of the "boxcar" window, defined as

$$f_{BC}(t) = \begin{cases} 1, & -t_{\max} \leq t \leq t_{\max} \\ 0, & \text{otherwise} \end{cases} \tag{2.11}$$

are smoothed out weighting the signal by a function, like, e.g. a gaussian or a lorentzian function, that cuts the observation window erasing the baseline noise. The apodization itself leads to a further broadening of the transformed signal.[90] Figs. 2.5 and 2.6 illustrate how the choice of apodization function used in the inverse Fourier transform can influence the calculated transition rates.

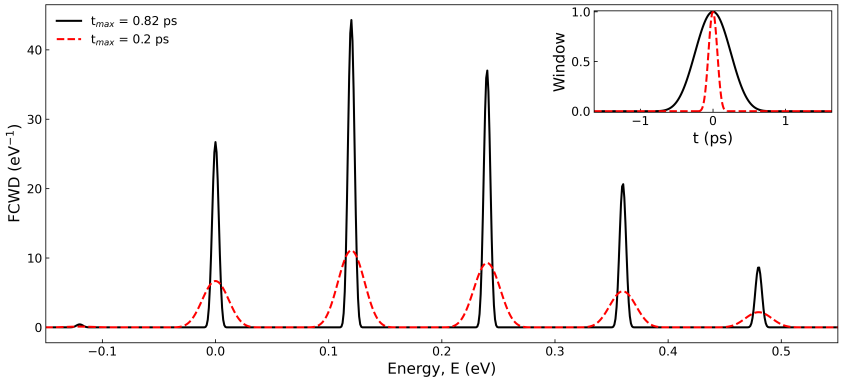

Figure 2.5: Rate spectra computed as the inverse FT of the GF relevant to the system described in Fig. 2.3. The black and red curves refer to results obtained upon apodization with a Blackman-Harris function[2] with $t_{max} = 0.82\,\text{ps}$ and $t_{max} = 0.233\,\text{ps}$, respectively. The apodization functions, shown in the inset, correspond to the observation window set in Fig. 2.4.

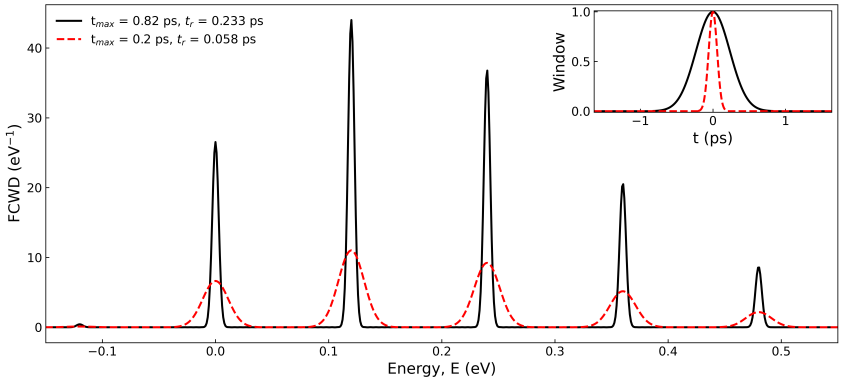

Figure 2.6: Rate spectra computed as the inverse FT of the GF relevant to the system described in Fig. 3 (main text). The black and red curves refer to results obtained upon apodization with a gaussian functions with $t_{max} = 0.82\,\text{ps}$ and $t_{max} = 0.233\,\text{ps}$, respectively. The apodization functions, shown in the inset, are selected as to best compare with the Blackman-Harris functions in Fig. 2.5.

The time-dependent GF functions are reported in panels A of Figs. 2.2 and 2.3 in a wide time window, as to visualize several of their typical recurrences.

To illustrate the effect of cutting the signal, we weight the GF adopting two gaussian functions with different widths, as measured by t_r:

$$G(t, t_r) = \exp\left[-\frac{1}{2}\left(\frac{t}{t_r}\right)^2\right] \tag{2.12}$$

[2]The Blackman-Harris function is defined as:

$$BH(t) = 0.35875 - 0.48829\cos\left(\frac{2\pi t}{t_{\max}}\right) + 0.14128\cos\left(\frac{4\pi t}{t_{\max}}\right) - 0.01168\cos\left(\frac{6\pi t}{t_{\max}}\right)$$

Panels B and C in Figs. 2.2 and 2.3 show, for the same systems, the rate-spectra calculated for two different widths of the gaussian apodization function. The inverse FT of the GF depends only on the energy and not on the adiabatic gap of the system, so that the evaluation of the rates constants of the upward and downward transitions can be performed once $F(E)$ is known at $E = -E_{ad}$ and $E = E_{ad}$, respectively, as illustrated in Figs. 2.2 and 2.3 for the case of $E_{ad} = 0.1\,\text{eV}$. Reliable estimates of the rates can only obtained when the observation window defined by the apodization function quickly damps the oscillations leading to broad rate-spectra, i.e. to rates that smoothly vary with the energy. Indeed, the spiky rate-spectra in Fig. 2.2C and, even worse, in Fig. 2.3C would lead to excessively large uncertainties in the rates, since even tiny variations in the adiabatic gap can cause enormous changes in the estimated values.[91]

The situation is similar, even if less obvious, in the multimode case. Figs. 2.7 and 2.8 show the results obtained for a system where the overall relaxation energy is distributed among five oscillators with different frequencies, as specified in the captions of the figures. In Fig. 2.7, both high and low frequency frequency modes are included, while in Fig. 2.8 only high frequency modes are considered. In the multimode case, when only high frequency modes are coupled to the electronic system, broad spectra are only obtained when a fast enough damping is ensured by a sufficiently narrow observation window (Fig. 2.8). On the opposite, when low-frequency modes are present, calculated spectra are broad, hence leading to acceptable results, even with fairly wide gaussian apodization functions ($t_r = 100\,\text{fs}$, cf. Fig. 2.7C). However, low frequency modes are often related to strongly anharmonic conformational modes, shedding doubts on the reliability of standard GF approaches in this regime.[83]

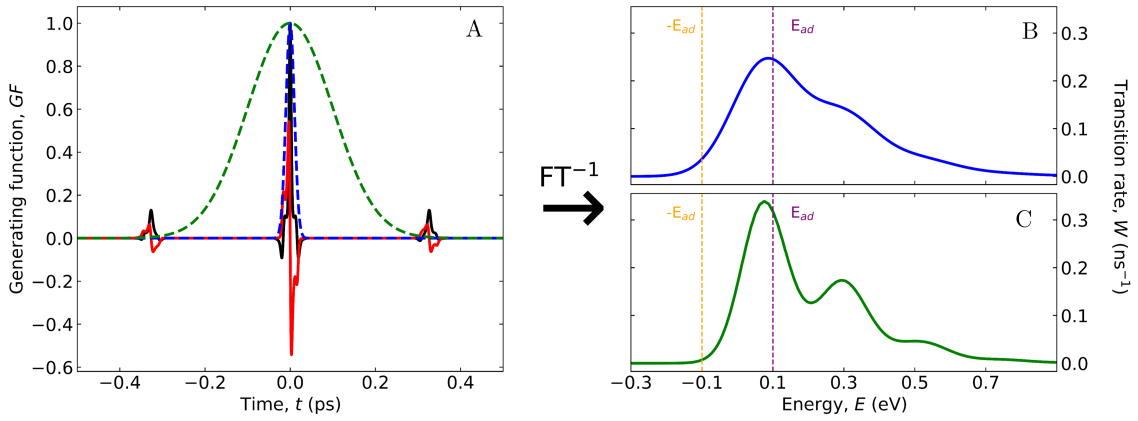

Figure 2.7: The same as Fig. 2.2, but for a system with five coupled modes with frequencies $\hbar\omega = 0.012, 0.027, 0.19, 0.23, 0.25\,\text{eV}$ and total relaxation energy $\epsilon_{tot} = 0.2\,\text{eV}$ equipartitioned among the five modes.

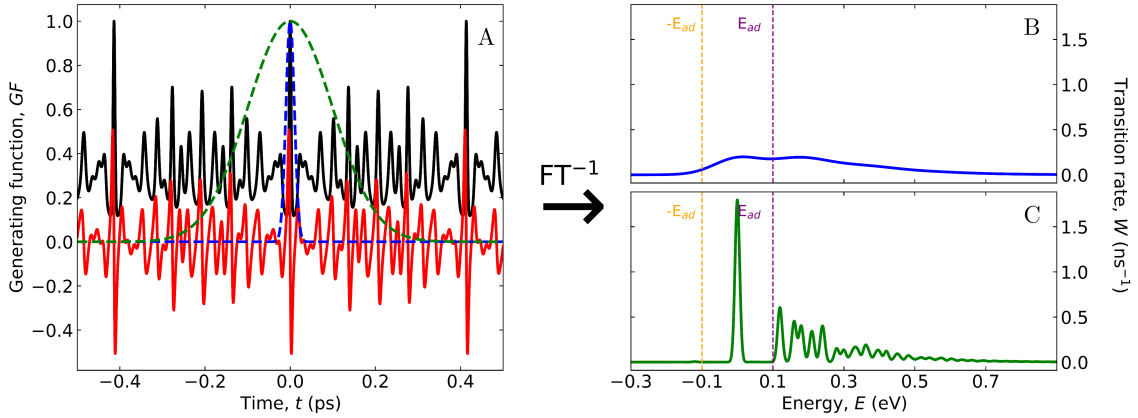

Figure 2.8: The same as Fig. 2.2, but for a system with five coupled modes with frequencies $\hbar\omega = 0.12, 0.16, 0.18, 0.21, 0.24\,\text{eV}$ and total relaxation energy $\epsilon_{tot} = 0.2\,\text{eV}$ equipartitioned among the five modes.

To further illustrate this point, Fig. 2.9 shows the dependence of the calculated rates on the width of the apodization function for the multimode cases in Fig. 2.7 and 2.8). In the multimode system with low-frequency modes (left panels of Figs. 2.9), the specific choice of the apodization functions is not that critical, since rates are marginally affected by the specific choice of t_r in a fairly large window of t_r values. This defines the window of t_r values where reliable results for the rates can be obtained, as also demonstrated by the ratio between upward and downward transition rates that, in this interval, properly converges to the thermodynamic limit:

$$\frac{W_{2\leftarrow 1}}{W_{1\leftarrow 2}} = \exp\left(-\beta E_{ad}\right) \tag{2.13}$$

In contrast, when only high-frequency modes are coupled to the electronic system (right panels of Fig. 2.9), a wild dependence of the rates on the apodization function makes the approach hardly reliable.

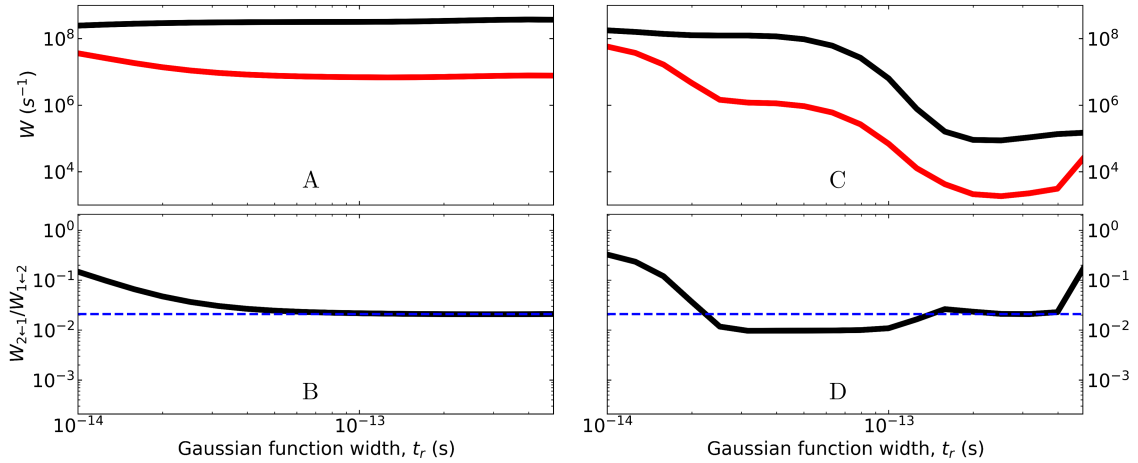

Figure 2.9: Rate dependence on the width of the gaussian apodization function, t_r, calculated for the multimode systems described in Fig. 2.7 and Fig. 2.8, left and right panels, respectively, for $E_{ad} = 0.1\,\text{eV}$. Top panels show the estimated $1 \leftarrow 2$ and $2 \leftarrow 1$ rates (black and red curves, respectively). Bottom panels show the ratio of the two rates, compared to the thermodynamic limit (blue dashed line).

The GF approach is very powerful as it allows, with little computational effort, to estimate the non-radiative rates of molecular systems accounting for all the vibrational modes, as extracted from *ab initio* calculations, also for fairly large molecules with a very large number of vibrational modes. General expressions are available for more complex models than addressed here, including *e.g.* quadratic terms in the electron-vibration coupling, Herzberg-Teller corrections and non-adiabatic coupling.[78, 80, 84, 86, 87, 92–94] Several variants of the methods are implemented in different computational codes,[69, 70, 77, 95–97] whose popularity is booming. When many coupled modes are present, including low-frequency modes and the treatment is extended to account for vibronic coupling beyond the linear term, calculated rate-spectra are very busy so that even a tiny broadening of the bands as related to fairly large observation window are enough to lead to smooth shapes and reliable rates. While, again, an exact FT transform of the whole GF would unavoidably lead to rate-spectra made of a series of Dirac-δ, the extremely long recurrence time associated with many vibrational degrees of freedom would make this limiting behavior irrelevant. On medium size molecules, where only few vibrations to the electronic degrees of freedom, the choice of the observation window becomes crucial and may actually dominate the calculated rates.[83]

Most often, the subtleties associated with the choice of the apodization functions are overlooked and the damping of the GF function is introduced just as a numerical trick and very little consideration is given to its fundamental role as a way to *open* the closed quantum system described by the ssFGR. Defining a finite observation time-window for the GF (*i.e.* selecting a specific width of the apodization function) amounts to assign a finite lifetime to the molecular eigenstates, a fundamental issue that requires careful consideration. Typical relaxation times of vibronic eigenstates of simple molecules in solution are estimated in the 100 fs range.[98] Care should be taken in systems where much faster damping is needed to get smooth rate-spectra and hence reliable rate estimates. Of course, as obvious from the previous discussion, reliable rates can only be obtained if the rate spectrum is fairly broad, so that the rates vary smoothly with the adiabatic gap[91] and are roughly independent of the width of the apodization function in a reasonably wide range. These conditions are easily recovered for large flexible molecules, where many modes, including low-frequency modes, are coupled to the electrons.

2.4 An open quantum system approach

The Hamiltonian in Eq. 2.1 describes a closed quantum system, *i.e.* a system that cannot exchange energy with the environment, so that, strictly speaking, neither downward nor upward non-radiative transitions are allowed. The damping of the GF function is an effective way to assign a finite lifetime to the signal and hence to the states of the system, implementing in a rough way the physics of open quantum systems. More refined open quantum system approaches are available to better

describe the excited states dynamics of molecular systems. The price to be paid is a much more expensive calculation, so that, while the GF approach can deal with a very large number of coupled vibrations, in the proposed open quantum system approach, only few vibrational modes can be accounted for. Accordingly, the open quantum system model is useful for comparison purposes but, as it stands, it does not represent a viable alternative to the GF approach. On the other hand, while the GF approach works well for harmonic potentials, accounting for linear and quadratic coupling at most, the proposed open quantum system approach works, at the same (high) computational cost for harmonic or anharmonic potential energy surfaces, being not limited to second order expansions.

In open quantum system approaches, the system of interest, defined in our case by the Hamiltonian in Eq. 2.1, is coupled to a thermal bath, most often a collection of harmonic oscillators, so that the total (system+bath) Hamiltonian reads:

$$\hat{H} = \hat{H}_0 + \sum_k \hbar\omega_k \left(\hat{b}_k^\dagger \hat{b}_k + \frac{1}{2}\right) + \sum_{j=1}^{N} \sum_k \frac{g_{jk}}{2} \left(\hat{a}_j^\dagger + \hat{a}_j\right) \left(\hat{b}_k^\dagger + \hat{b}_k\right) \tag{2.14}$$

where j and k run on the system and bath oscillators, respectively. The second term in the above equation describes the bath as a collection of harmonic oscillators. The system-bath coupling Hamiltonian (the third term in the above equation) introduces a linear coupling between each vibrational mode of the system and the vibrational modes of the bath and, following Ref. [99], each vibrational mode is coupled to an independent thermal bath, with g_{jk} measuring the strength of the coupling between the j-th mode of the system and the k-th mode of the bath. We make the simplifying hypothesis that all the modes of the system are coupled with the same strength to each bath mode, setting $g_{jk} = g_k$. Since the frequencies of the bath oscillators are distributed over a continuum, the strength of the coupling is defined by the spectral density:

$$\mathcal{S}(\omega) = \sum_k |g_k|^2 \delta(\omega - \omega_k). \tag{2.15}$$

In the following, for the sake of simplicity, we set the spectral density to a constant value and introduce a friction coefficient, $\gamma = \pi\mathcal{S}(\omega)/\hbar^2$, that controls the strength of the system-bath coupling.[100] Other commonly used spectral density functions are the Debye spectral density:

$$\mathcal{S}(\omega) = \frac{2\gamma\hbar^2}{\pi} \frac{\frac{\omega}{\omega_c}}{1 + \left(\frac{\omega}{\omega_c}\right)^2} \tag{2.16}$$

and the Ohmic spectral density:

$$\mathcal{S}(\omega) = \frac{\gamma\hbar^2}{\pi} \frac{\omega}{\omega_c} \exp\left\{1 - \frac{\omega}{\omega_c}\right\} \tag{2.17}$$

where ω_c is the cutoff frequency. A plot of the three functions versus the energy is sketched in Fig. 2.10. As it was also shown in a previous paper from our research group in Parma,[101] the choice of a specific spectral density function gives marginally different results.

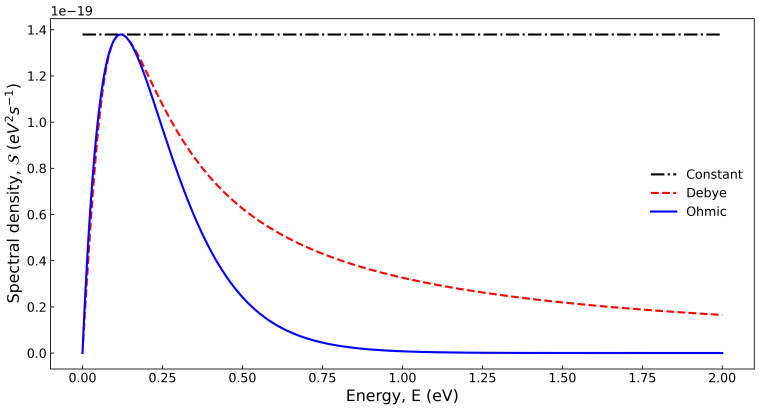

Figure 2.10: Energy dependence of the three commonly used spectral densities: constant (black dash-dotted line), Debye (red dashed line), Ohmic (blue solid line). We set the friction coefficient and the cutoff frequency to $\gamma = 3.16\,\mathrm{ps}^{-1}$ and $\hbar\omega_c = 0.12\,\mathrm{eV}$, respectively.

In order to address the dynamics of the system, we start with the full non-adiabatic diagonalization of the system Hamiltonian, H_0 in Eq. 2.1, to get the system eigenstates $|a\rangle$ and energies E_a. To such an aim, the Hamiltonian is written on the basis obtained as the direct product of the two electronic states, $|1\rangle$ and $|2\rangle$, times the eigenstates of the harmonic oscillator associated with state $|1\rangle$. The infinite basis of the harmonic oscillator is truncated to include states within 1.5 eV from the bottom of the lower PES, in order to ensure convergence of the results. The large number of non-adiabatic states makes the open quantum system approach computationally demanding, so that a very small number of vibrational modes can be explicitly described, especially when low-frequency vibrations enter into play. Since V is very small, the vibronic eigenstates $|a\rangle$ closely resemble the $|I\rangle\,|l\rangle$ and $|F\rangle\,|\tilde{m}\rangle$ states discussed in the previous section.

The Redfield equation[102] describes the dynamics of a system coupled to external thermal baths. The Redfield theory applies in the hypothesis that the thermal baths responds much faster than relevant degrees of freedom of the system itself. Accordingly, they describe homogeneous broadening phenomena and not the inhomogeneous broadening associated with disorder and with slow environmental degrees of freedom. The mathematical formulation of the Redfield equation reads:

$$\frac{d}{dt}\rho_{ab}(t) = -i\omega_{ab}\rho_{ab}(t) + \sum_{c,d} R_{ab,cd}\rho_{cd}(t) \tag{2.18}$$

where $\rho_{ab} = \langle a|\,\hat{\rho}\,|b\rangle$ is an element of the reduced density matrix on the basis of the eigenstates of H_0. The first term in the above equation describes the Liouville dynamics of the system, with $\omega_{ab} = \frac{E_a - E_b}{\hbar}$. The second term accounts for the relaxation dynamics, with $R_{ab,cd}$ being an element of the Redfield tensor [99, 100]:

$$R_{aa,cc}(\gamma_k) = -\delta_{a,c}\sum_e \left[\Gamma^+_{ae,ec}(\gamma_k) + \Gamma^-_{ce,ea}(\gamma_k)\right] + \Gamma^+_{ca,ac}(\gamma_k) + \Gamma^-_{ca,ac}(\gamma_k)$$

and

$$R_{ab,ab}(\gamma_k) = -\sum_e \left[\Gamma^+_{ae,ea}(\gamma_k) + \Gamma^-_{be,eb}(\gamma_k)\right]$$

The relaxation tensors Γ^+ and Γ^- are defined as:

$$\Gamma^+_{db,ac}(\gamma_k) = \gamma_k \begin{cases} \langle d|\hat{Q}|b\rangle\langle a|\hat{Q}|c\rangle\langle n(\omega_{ac})\rangle_{bath} & \omega_{ac} > 0 \\ \langle d|\hat{Q}|b\rangle\langle a|\hat{Q}|c\rangle\langle n(\omega_{ca})+1\rangle_{bath} & \omega_{ac} < 0 \end{cases} \tag{2.19}$$

$$\Gamma^-_{db,ac}(\gamma_k) = \gamma_k \begin{cases} \langle d|\hat{Q}|b\rangle\langle a|\hat{Q}|c\rangle\langle n(\omega_{bd})\rangle_{bath} & \omega_{bd} > 0 \\ \langle d|\hat{Q}|b\rangle\langle a|\hat{Q}|c\rangle\langle n(\omega_{db})+1\rangle_{bath} & \omega_{bd} < 0 \end{cases} \tag{2.20}$$

where $\langle n(\omega)\rangle$ is the Bose-Einstein distribution function:

$$\langle n(\omega)\rangle = (\exp(\beta\hbar\omega) - 1)^{-1} \tag{2.21}$$

We integrate the Redfield dynamics (Eq. 2.18) in the Bloch approximation (RB dynamics). Within this approximation, the dynamics of populations and coherences is decoupled and is described by the following equations:

$$\frac{\partial}{\partial t}\rho_{aa}(t,\gamma_k) = \sum_c R_{aa,cc}(\gamma_k)\,\rho_{cc}(t) \tag{2.22}$$

$$\rho_{ab}(t,\gamma_k) = \rho_{ab}(0)\,e^{\left(R_{ab,ab}(\gamma_k) - i\omega_{ab}\right)t} \tag{2.23}$$

The Eq. 2.22 has the analytical solution

$$\rho_{aa}(t,\gamma_k) = \sum_{cc} u^{(aa)}_{cc} p_{cc} e^{\lambda_{cc}(\gamma_k)t} \tag{2.24}$$

where $\boldsymbol{u}$ and $\boldsymbol{\lambda}(\gamma_k)$ are the eigenvectors and eigenvalues of the matrix containing the $R_{aa,cc}$ elements, respectively. The vector $\boldsymbol{p}$ can be evaluated once the initial conditions are set, by solving the linear system of equation:

$$\rho_{aa}(0) = \sum_{cc} u^{(aa)}_{cc} p_{cc} \tag{2.25}$$

To estimate rates, the population of the diabatic states is calculated as the expectation values of the operators $|1\rangle\langle 1|$ and $|2\rangle\langle 2|$. Specifically:

$$P_1(t) = \mathrm{Tr}\{\hat{\rho}(t)\,|1\rangle\langle 1|\} \qquad P_2(t) = \mathrm{Tr}\{\hat{\rho}(t)\,|2\rangle\langle 2|\} \tag{2.26}$$

Fig. 2.11 illustrates results obtained for a system with a single coupled high frequency mode. In this case, the thermally equilibrated $|1\rangle$ state has sizable population only in the lowest vibrational state, so that the impulsive excitation generates a coherent state that evolves on the potential relevant to state $|2\rangle$, showing the characteristic coherent oscillations.[100]

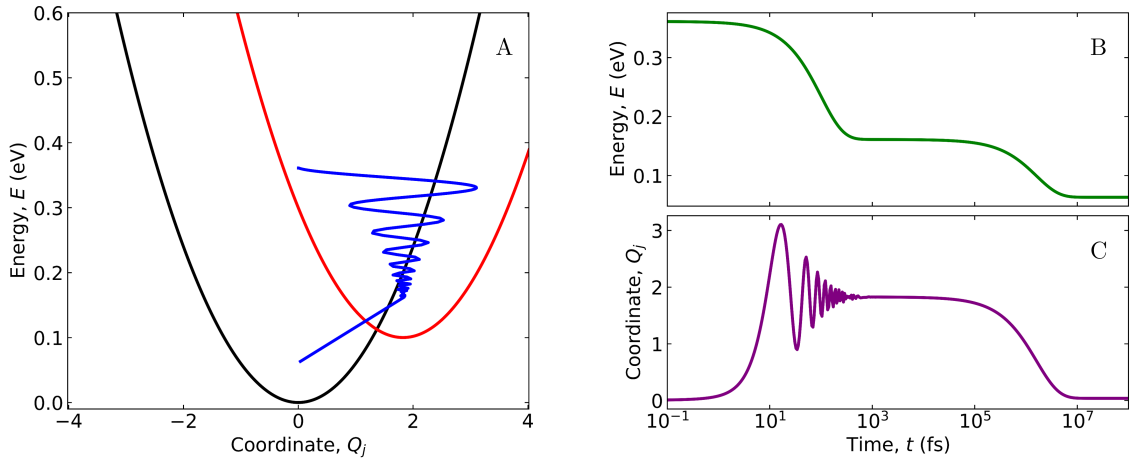

Figure 2.11: The Redfield-Bloch trajectory of a system with a single vibrational mode with $\hbar\omega = 0.12\,\text{eV}$, $\epsilon = 0.2\,\text{eV}$ and $E_{ad} = 0.1\,\text{eV}$. The friction coefficient is set to $\gamma = 0.01\,\text{fs}^{-1}$. Panel A: the two diabatic PES and, in blue the system trajectory shown as energy vs the vibrational coordinate. Panels B and C show the time evolution of the energy and of the vibrational coordinate, respectively.

The vibrational relaxation energy (0.2 eV in the figure) is lost in the first few hundreds of femtoseconds. After that, the system stays in the lowest vibrational eigenstate of $|2\rangle$, corresponding to the thermally equilibrated state, for a long time and finally reaches state $|1\rangle$ in the nanosecond time-window. To address the non-radiative rates, the system is prepared in $|1\rangle$, the lowest energy state, assuming a thermal distribution on relevant vibrational levels. At time zero, the system is instantaneously excited to state $|2\rangle$ and from there the Redfield-Bloch (RB) dynamics is calculated.

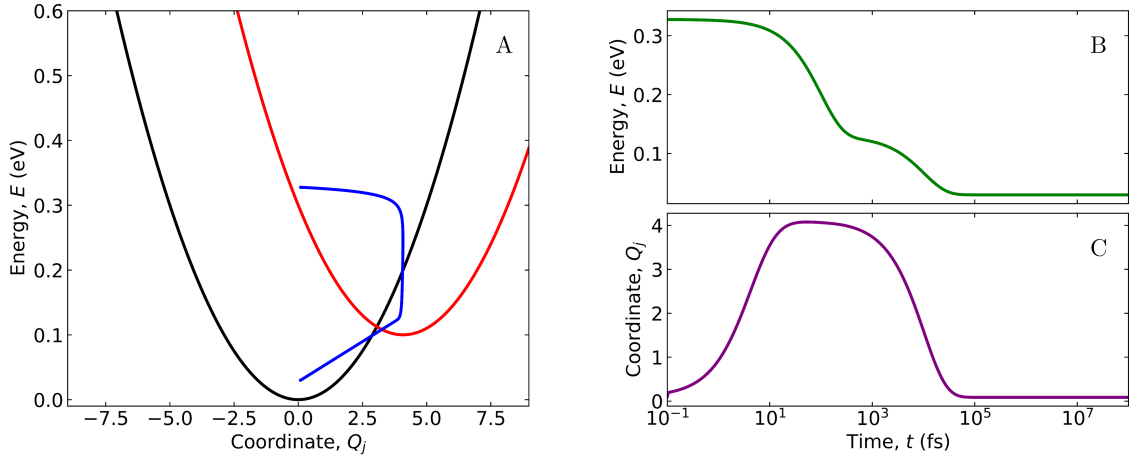

Figure 2.12: The same as Fig. 2.11 but for a different value of the frequency of the coupled mode, $\hbar\omega = 0.024\,\text{eV}$.

Similar results are shown in Fig. 2.12, where a single low-frequency mode is coupled to the electronic system. The main difference from the previous case arises from the starting state, which is not a coherent state, due to the thermal population of several vibrational levels. Accordingly, the coherent oscillations in the early dynamics are lost. Moreover, we observe that the system stays in the lowest vibronic state in

the upper state manifold, a shorter interval of time if compared with the system with a high frequency mode (Fig. 2.11), the descent to the ground state occurring in $\sim$ 100 ps. The faster relaxation towards the ground state observed when the coupled mode has a low frequency is related to the choice of a constant spectral density. Indeed the density of states of the thermal bath is large at low frequency, so that, for a constant spectral density, a faster relaxation is expected, when driven by a low frequency mode compared to a high frequency mode.

In Figs. 2.13 and 2.14 we show that adopting a Debye spectral density, which properly vanishes in the zero frequency limit, the relaxation dynamics of the system with a low-frequency coupled vibration considerably slows down, while the dynamics of the system with a high-frequency mode is marginally affected. These results

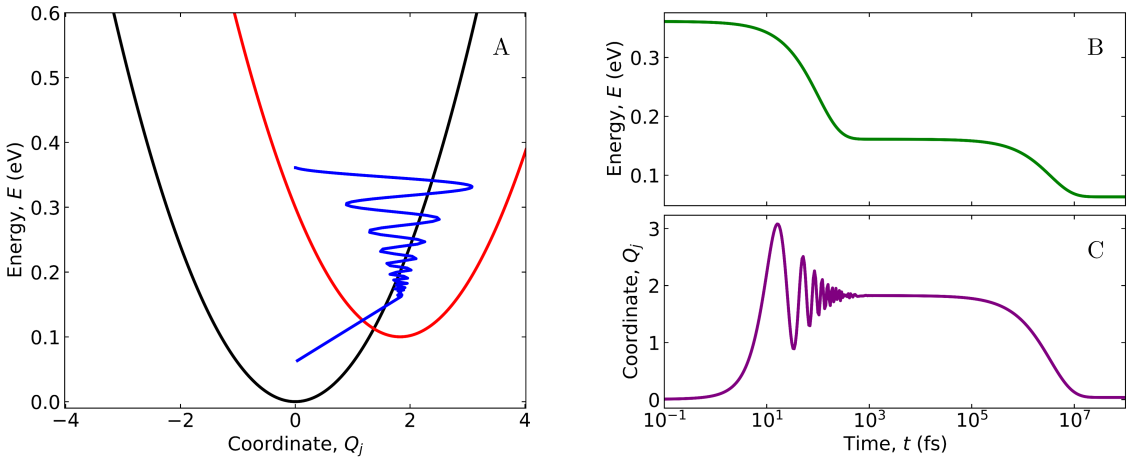

Figure 2.13: Same as in Fig. 2.11, adopting a Debye spectral density, with $\hbar\omega_c = 0.12\,\text{eV}$ and $\gamma = 0.01\,\text{fs}^{-1}$.

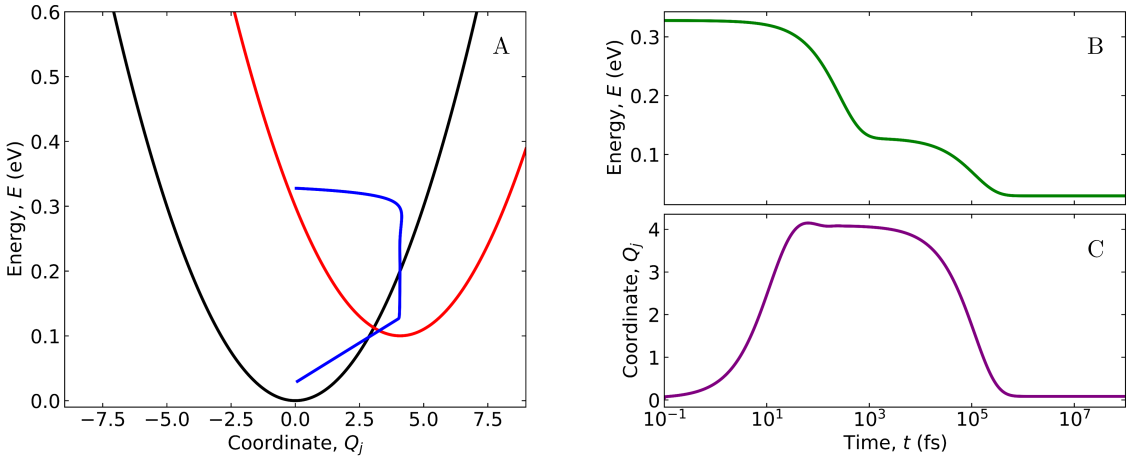

Figure 2.14: Same as in Fig. 2.12, adopting a Debye spectral density with $\hbar\omega_c = 0.12\,\text{eV}$ and $\gamma = 0.01\,\text{fs}^{-1}$.

illustrate the potential of the RB approach: the complete dynamics of the system can be calculated, addressing not just the $|1\rangle \leftarrow |2\rangle$ conversion, as in the GF approach, but also the vibronic relaxation occurring when the initial state is not

thermally equilibrated. Indeed FGR-based approach can be generalized to describe the dynamics from states that are not thermally equilibrated,[103, 104] relying on semiclassical approximations. More to the point, here we only address systems with tiny V coupling, ensuring at the same time the applicability of the FGR and a good separation of the timescales of the vibronic and electronic relaxation, so that the system lives a sizable time interval in the lowest vibronic state in the upper state manifold. In these conditions, the FGR and hence the GF approach can be applied. However these approaches are bound to fail for large V, when the two dynamics get entangled. In these situations, open quantum system approaches are instead robust.[99, 100]

For a more stringent comparison with the GF results, we now extract non-radiative rates from the Redfield dynamics. Fig. 2.15 shows the time evolution of the populations of the two electronic states, calculated for the same system in Fig. 2.11 for two different choices of the friction coefficient: of course the populations change faster with increasing γ, *i.e.* when the system-bath coupling is stronger. The initial vibronic relaxation is silent in these figures, since it does not affect the population of the electronic states. The rates for the downwards and upwards dynamics can then be calculated from the fitting of the diabatic populations.

Specifically, we adopt the following kinetic model:

$$|1\rangle \rightleftharpoons |2\rangle$$

so that the dynamics of the diabatic states obeys the following system of equations:

$$\begin{cases} \frac{dP_2(t)}{dt} + W_{1\leftarrow 2}P_2(t) - W_{2\leftarrow 1}P_1(t) = 0 \\ \frac{dP_1(t)}{dt} - W_{1\leftarrow 2}P_2(t) + W_{2\leftarrow 1}P_1(t) = 0 \\ 1 - P_2(t) - P_1(t) = 0 \end{cases} \tag{2.27}$$

which is solved analytically as:

$$\begin{cases} P_1(t) = P_1(0)e^{Bt} + C\left(1 - e^{Bt}\right) \\ P_2(t) = P_2(0)e^{Bt} + (1 - C)\left(1 - e^{Bt}\right) \end{cases} \tag{2.28}$$

where $P_1(0)$ and $P_2(0)$ are the initial populations of the diabatic states, while B and C (both depending on the value of γ_k) are fitting parameters defined as:

$$B = -\left(W_{1\leftarrow 2} + W_{2\leftarrow 1}\right) \qquad C = \frac{W_{1\leftarrow 2}}{W_{1\leftarrow 2} + W_{2\leftarrow 1}} \tag{2.29}$$

Finally, the rates of the downward and upward processes are finally obtained as:

$$W_{1\leftarrow 2} = -BC \qquad W_{2\leftarrow 1} = B\left(C - 1\right) \tag{2.30}$$

A delicate issue here is the definition of the strength of the system-bath coupling, measured in our approach by the friction coefficient γ. We set $\gamma \sim 10^{-2}\,\mathrm{fs}^{-1}$ in Figs. 2.11 and 2.12, as to complete the vibronic relaxation in the first few hundreds of femtoseconds.[98] Fig. 2.16 shows how the $|1\rangle \leftarrow |2\rangle$ and $|2\rangle \leftarrow |1\rangle$ rates vary with the friction coefficient for a system with a single vibrational mode that mimics the five-mode system in Fig. 2.7 in terms of a single coupled mode with average frequency

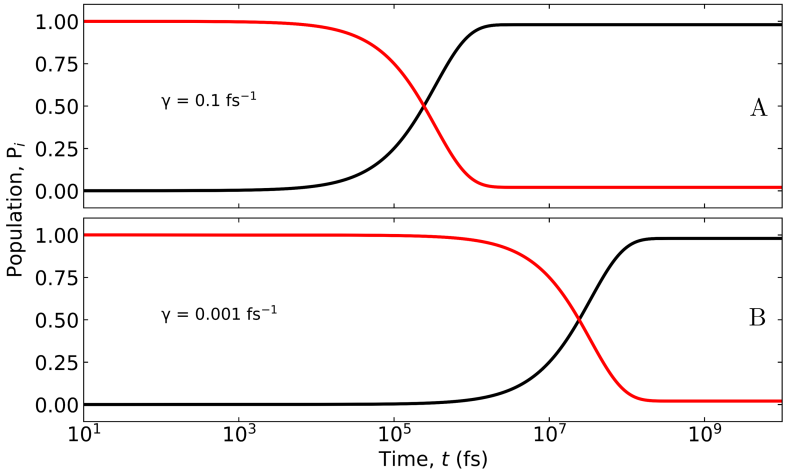

Figure 2.15: Black and red curves show the time-dependence of the population of the diabatic $|1\rangle$ and $|2\rangle$ states, respectively, calculated for the system in Fig. 2.11. The friction coefficients are set to $\gamma = 0.1\,\mathrm{fs}^{-1}$ in panel A (for the sake of comparison) and to $\gamma = 0.001\,\mathrm{fs}^{-1}$ in panel B (as in Fig. 2.11).

$\hbar\omega = 0.14\,\mathrm{eV}$ and accounting for the total relaxation energy ($\epsilon_{tot} = 0.2\,\mathrm{eV}$). Quite interestingly, setting the friction coefficient to $\sim 0.001\,\mathrm{fs}^{-1}$ both the upward and downwards rates calculated in the GF approach for this multimode system can be reproduced by the RB model with a single vibration.
Before closing this section, we mention that if a single coupled mode is accounted for, the Hamiltonian in Eq. 2.14 coincides with the Hamiltonian originally proposed in Ref. [106]. Closed expressions for non-radiative rates, relying again on the FGR, were proposed for this Hamiltonian by Sun and Geva (SG).[105] Fig. 2.17 shows that the SG rates compare very favourably with the rates obtained in the RB approach, adopting the same spectral density. At variance with SG, the RB approach, while limited to the regime of weak system-bath couplings, can also be applied in the strong coupling regime ($V > E_{ad}$) and can be easily extended to account for a few coupled modes, for non-linear electron-vibration coupling as well as for anharmonicity. The comparison with GF results is difficult, since a specific relation between the spectral-density and the apodization function is missing.

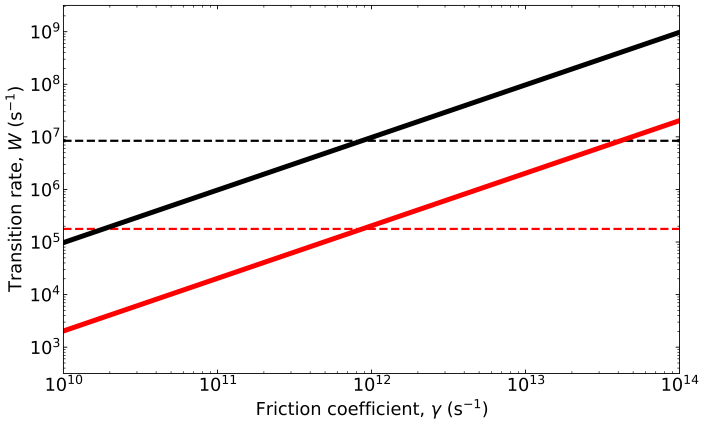

Figure 2.16: Continuous lines: transition rates of the single mode system: $E_{ad} = 0.1\,\text{eV}$, $V = 10^{-4}\,\text{eV}$, $\hbar\omega = 0.14\,\text{eV}$, $\epsilon = 0.2\,\text{eV}$ as a function of the spectral density, computed using the open quantum systems approach. Dashed lines: transition rates of the system as in Fig. 2.7, computed using the generating function approach in the reliable range of the damping parameter. Black and red lines refer to the downward and upward transitions, respectively.

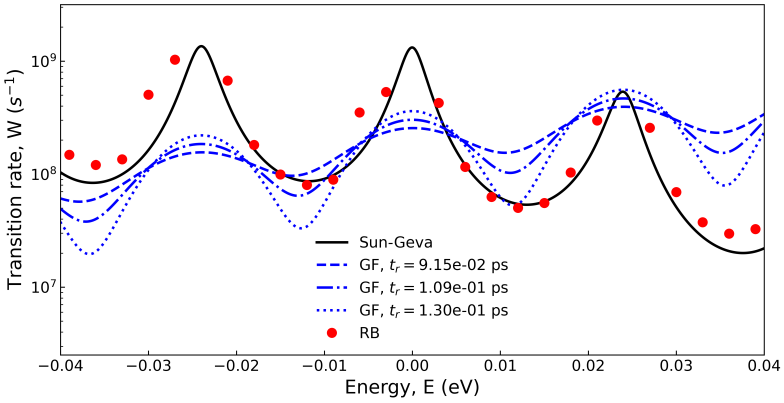

Figure 2.18: Rate spectra calculated following Sun-Geva[105] (black line) and from the RB trajectories (red dots), for the model Hamiltonian in Eq. 2.14 with $V = 10^{-4}\,\text{eV}$, $\hbar\omega = 0.024\,\text{eV}$, $\epsilon = 0.2\,\text{eV}$. A Ohmic spectral density is introduced with $\hbar\omega_c = 0.12\,\text{eV}$ and $\gamma = 10^{-3}\,\text{fs}^{-1}$. The Bloch approximation fails when the adiabatic gap coincides with a multiple of the vibrational frequency, relevant points are therefore suppressed in the graphic. The blue line show rate spectra calculated in the GF approch: the comparison with Sun Geva or RB results is qualitative, the GF spectra are multiplied by a factor 3.2×10^8 to facilitate the comparison. The GF function is damped by an gaussian apodization function with different t_r.

Figs. 2.17 and 2.18 compare the SG and RB rates with the GF rates (on a arbitrary scale for the rates) calculated with different apodization functions. Some similarity is seen between the SG or RB results and the GF results since all rate-spectra show peaks at energies corresponding to multiples of the vibrational frequencies, as dictated by the Frank-Condon factors and therefore are qualitatively similar to optical spectra, but should not be confused with them, as relevant states and interactions are different. Looking in more detail, the GF results show an overall upward shift upon increasing the adiabatic gap, while the SG and RB results show a downward

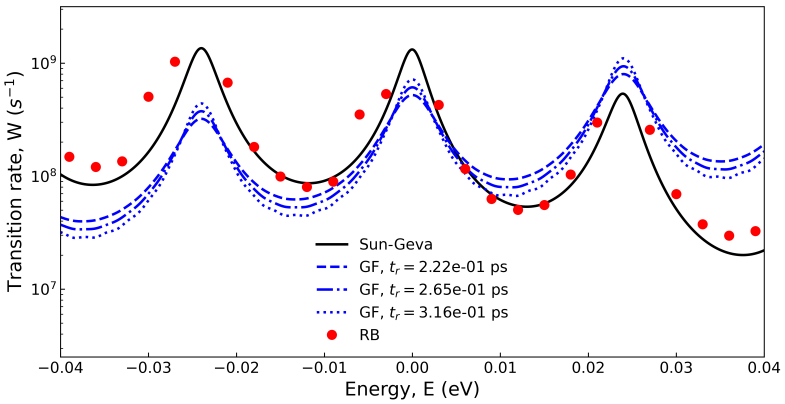

Figure 2.17: Rate spectra calculated following Sun-Geva[105] (black line) and from the RB trajectories (red dots), for the model Hamiltonian in Eq. 2.14 with $V = 10^{-4}\,\text{eV}$, $\hbar\omega = 0.024\,\text{eV}$, $\epsilon = 0.2\,\text{eV}$. A Ohmic spectral density is introduced with $\hbar\omega_c = 0.12\,\text{eV}$ and $\gamma = 10^{-3}\,\text{fs}^{-1}$. The Bloch approximation fails when the adiabatic gap coincides with a multiple of the vibrational frequency, relevant points are therefore suppressed in the graphic. The blue line show rate spectra calculated in the GF appproch: the comparison with Sun Geva or RB results is qualitative, the GF spectra are multiplied by a factor 3.2×10^8 to facilitate the comparison. The GF function is damped by an exponential function $\exp(-|t/t_r|)$ with different t_r.

shift, pointing again to a limited reliability of GF rates.

2.5 Dissipative origin of the damped generating function

Comparing rates obtained in the GF approach with those obtained from the RB trajectories is tricky. The strength of the system-bath coupling is defined in the RB model by the spectral density, while in the GF approach the same information is hidden in the width of the apodization function. The relation between the two quantities is however not obvious. In this section, in order to establish a meaningful comparison we introduce a *naturally-damped* (ND) GF function. The oscillating terms in Eq. 2.5 share the same time-dependence as dictated by the Liouvillian dynamics for the off-diagonal elements of the density matrix, the so-called coherences: $\rho_{\tilde{m}l}(t) \propto \exp\left\{\frac{it}{\hbar}\left(E_{Il} - E_{F\tilde{m}}\right)\right\}$. To account for the dissipation, we then correct these oscillating terms introducing the same relaxation dynamics as dictated for coherences by the RB model, getting the naturally damped form of Eq. 2.5:

$$g^{(ND)}_{F\leftarrow I}(t) = \frac{2\pi|V|^2}{\hbar}\sum_l w_l \sum_{\tilde{m}} |\langle\tilde{m}|l\rangle|^2 \exp\left\{\frac{it}{\hbar}\left(E_{Il} - E_{F\tilde{m}}\right)\right\}\exp\{R_{\tilde{m}l}t\} \qquad (2.31)$$

where $R_{\tilde{m}l}$ are the elements of the RB tensor. In the above expression, each oscillating term is damped by a different exponential, as determined by the specific choice

of the system-bath coupling.

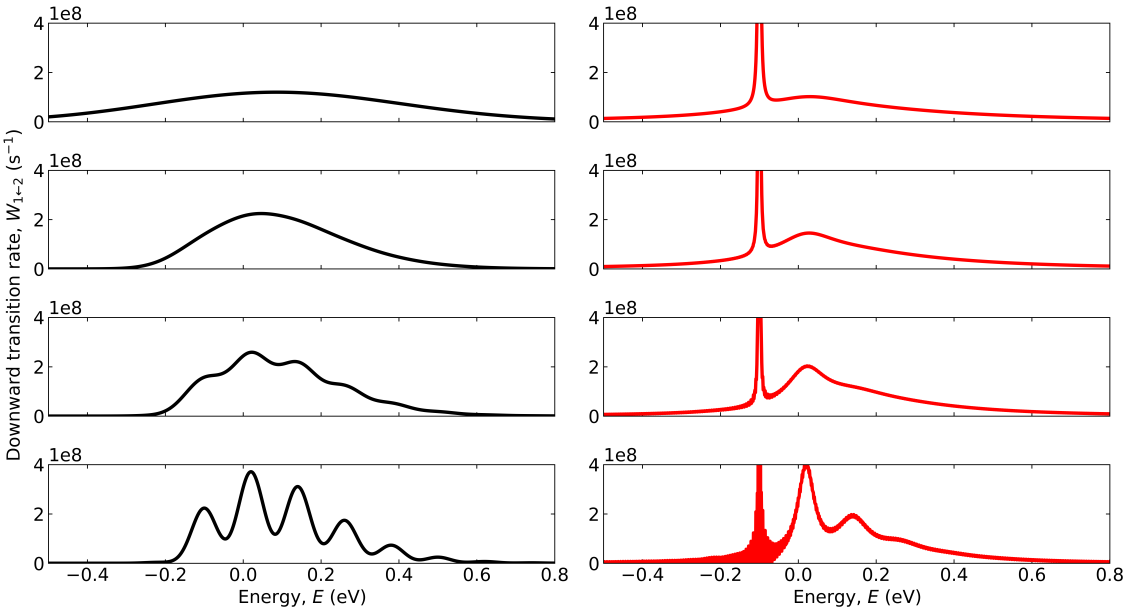

Figure 2.19: The rate spectra calculated as a function of the energy for the system with a single high frequency mode (model parameters as in Fig. 2.3). Left panels show results obtained in the GF approach with (from top to bottom) $t_r = 2.51, 7.94, 12.6, 20.0$ fs. Right panels show results obtained in the mixed approach, with (from top to bottom) $\gamma = 0.398, 0.251, 0.200, 0.0794$ fs^{-1}. Please notice that the oscillations appearing in the two lower right panels are a numerical artifact, due to the finite observation window.

Fig. 2.19 compares the results obtained with the GF approach for different choices of the width of the gaussian apodization function with the results from the ND approach proposed in this section for different values of the friction coefficient. Of course, the calculated rate-spectra become more resolved upon increasing the width of the apodization function (left panel from top to bottom) or when decreasing the friction coefficient (right panel from top to bottom). But the two approaches show qualitative differences. Most dramatically, a very narrow spike associated with the 0-0 line appears in the ND approach. We believe that the reason for this sharp feature is the very long relaxation time associated with the lowest energy vibrational level on each surface. Indeed, when V is set to zero, in either the lower or higher energy PES, the lowest vibrational eigenstate can only depopulate going upwards, a very unlikely process when high frequency modes are involved. In the adopted Bloch approach to the relaxation dynamics, without any source of pure dephasing (*i.e.* in the absence of inhomogeneous broadening), the relaxation of coherences is related to the lifetimes of the two states, through the relation:

$$R_{ab,ab} + \frac{\zeta_a^{-1} + \zeta_b^{-1}}{2} = 0 \tag{2.32}$$

where $\zeta_p = \left(\sum_{c \neq a} R_{cc,pp}\right)^{-1}$ is the lifetime of the eigenstate p. Accordingly, the relaxation of coherences involving very long lived states is very slow, justifying the appearance of the 0-0 spike in the rate spectra in the right panel of Fig. 2.19.

However, the apodization of the GF practically imposes the same lifetime on all vibronic states, leading to vibronic bands with equal width.

The situation is less dramatic when the coupled mode has a low frequency, as shown in Fig. 2.20.

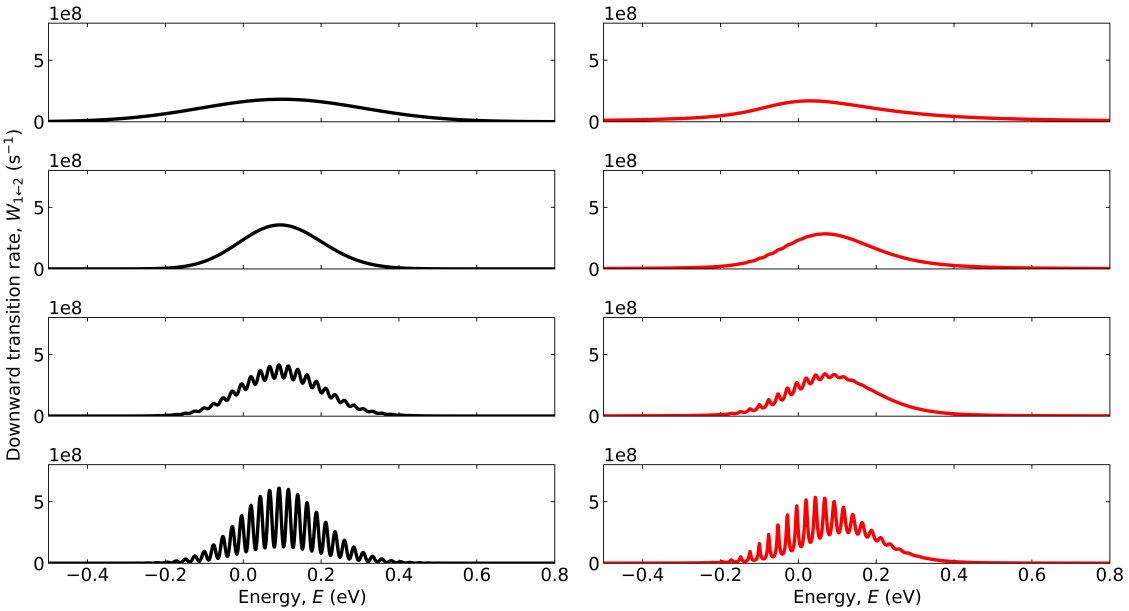

Figure 2.20: The rate spectra calculated as a function of the energy for the system with a single low frequency mode (model parameters as in Fig. 2.2). Left panels show results obtained in the GF approach with (from top to bottom) $t_r = 3.98, 31.6, 79.4, 125.9\,\mathrm{fs}$. Right panels show results obtained in the ND approach, with (from top to bottom) $\gamma = 0.0200$, 6.31×10^{-3}, 2.51×10^{-3}, $1.00 \times 10^{-3}\,\mathrm{fs}^{-1}$.

In this case, the contribution of the 0-0 line is negligible due to a fairly large Huang-Rhys factor and the two approaches lead to similar results. However, a difference should be mentioned: while in the GF approach all vibronic lines have the same width as imposed by the use of a generic apodization function, in the ND approach each line has its own width, since each coherence follows a different relaxation dynamics. Specifically, coherences involving states with high vibrational quantum numbers relax faster, leading to broader feature in the high-frequency portion of the rate spectrum.

The GF approach is not only used to calculate rates, indeed it is very well suited to calculate the shape of optical spectra.[67, 84, 92] Indeed, if in our equations V is substituted with the transition dipole moment, the rate-spectra become optical spectra (in the Condon approximation). A direct relation between the GF approach and the Heller approach[107] to absorption spectra is easily drawn. Specifically, starting with the reduced density matrix $\rho^{(0)}$ corresponding to the thermalized initial state:

$$\rho^{(0)} = \sum_l w_l \left|I, l\right\rangle \left\langle I, l\right| \tag{2.33}$$

To follow the dynamics of the system, the population is transferred to the final state

through an impulsive perturbation:

$$\hat{H}'(t) = \lambda \hat{V} \delta(t) \tag{2.34}$$

where λ is a constant parameter, that preserves the energy dimension of $\hat{V}(t)$. The subsequent dynamics (up to the first order in perturbation theory) leads to the following form for the coherences[108]:

$$\rho_{\tilde{m}l}(0) \approx \rho^{(0)}_{\tilde{m}l} + \lambda \frac{i}{\hbar} \left[\rho^{(0)}(0), \hat{V} \right]_{\tilde{m}l} = \lambda V \frac{i}{\hbar} \langle \tilde{m} | l \rangle \tag{2.35}$$

So that Eq. 2.31 becomes

$$g^{(ND)}_{F \leftarrow I}(t) = \frac{2\pi\hbar}{\lambda^2} \sum_l w_l \sum_{\tilde{m}} \rho_{l\tilde{m}}(0) \rho_{\tilde{m}l}(t) = \frac{2\pi\hbar}{\lambda^2} \langle \rho(0) \rho(t) \rangle_0 \tag{2.36}$$

where $\langle . \rangle_0$ defines the average over the thermally equilibrated initial state. The above equation demonstrates that the function $g^{(ND)}_{F \leftarrow I}(t)$ is just the autocorrelation function of the density matrix traced over the initial equilibrated state. Therefore it is not by chance that the rate spectra calculated via the GF approach closely resemble in shape the optical spectra.

However an issue arises here. Optical spectra are governed by the coherences (the off-diagonal elements of the density matrix), but rates are actually related to the population dynamics. This difference is not so subtle as it could appear: should some source of disorder be present, inhomogeneous broadening would affect coherences, and hence optical spectra, but it should be irrelevant to the population dynamics. This suggests that the proper way to calculate rates should rely on truly open quantum system approaches, as in the previous section, tracking the time evolution of the populations. A direct comparison of the rates obtained in the RB approach with the rates obtained in the ND approach is enlightening in this respect: precisely the same relaxation model is adopted in the two approaches, but in the ND approach coherences are addressed instead of populations.
Fig. 2.21 compares the rates obtained in the two approaches for the system with a low (panel A) and a high (panel B) frequency mode, both having the same adiabatic gap $E_{ad} = 0.1\,\text{eV}$. In both cases, the rates calculated in the RB approach increase with the friction coefficient, a sensible result since upon increasing the strength of the system-bath coupling a faster energy dissipation and hence a faster relaxation is expected. The situation is trickier in the ND approach with a non-monotonous behavior of the rates with the friction coefficient in the case of a coupled high frequency mode and a net decrease of the rates with the friction coefficient when a single low-frequency mode is accounted for. Both results are hardly acceptable on physical ground.

While one can argue that the unphysical results obtained in the ND model derive from its blended nature, we maintain that it represents just an effective way to introduce state-specific relaxation coefficients for each coherence into the GF approach, while allowing for a direct comparison with the RB approach. Indeed, inconsistencies are also apparent in the standard GF approach. Taking as reference the multimode system in Fig. 2.7 (the one that gives best results in the GF approach),

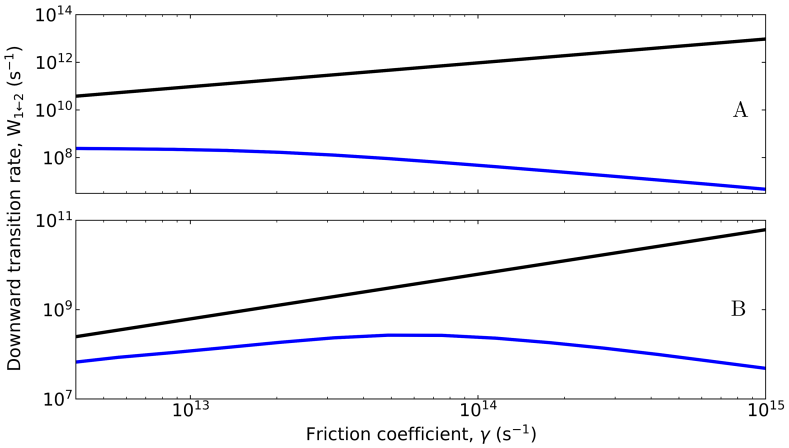

Figure 2.21: The downward rates calculated as a function of the friction coefficient for the systems described in Fig. 2.2 (panel A) and in Fig. 2.3 (panel B), respectively, with $E_{ad} = 0.1\,\text{eV}$. The black and the blue lines refer to the results obtained with the RB model and in the ND approach, respectively.

Fig. 2.22 shows the dependence of the downward rates calculated as a function of the width of the apodization function for different values of the adiabatic gap. Of course, the rates vary with the adiabatic gap, but what is disturbing is the different dependence on the width of the observation window, t_r, of the rates calculated for different values of the adiabatic gap. Again, t_r measures how fast the GF decays in time, accounting in a rough way for the system-bath coupling. Therefore, higher rates would be expected for smaller t_r, but this is not always the case. Moreover, the detailed balance, intrinsic to the RB approach, guaranties the proper ratio of the upward to the downward ratio, a condition that is not always respected in the GF approach (Fig. 2.9).

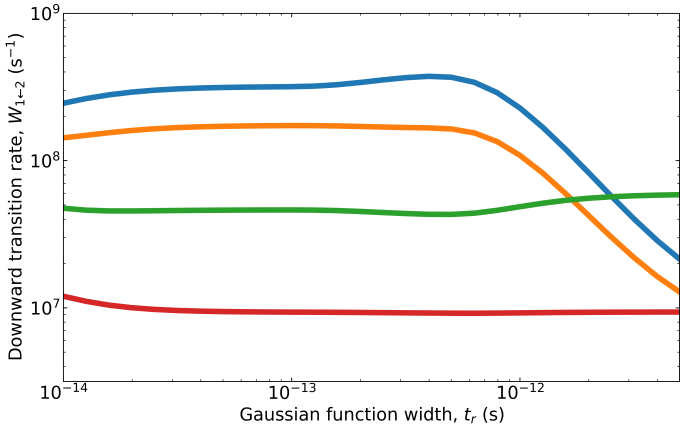

Figure 2.22: The downward rates calculated for the system in Fig. 2.7 as a function of the width of the apodization function, computed using different values of E_{ad} (in eV): 0.1 (blue), 0.3 (orange), 0.5 (green), 0.7 (red).

2.6 Introducing disorder

In the RB approach as discussed above, the system is only coupled to fast degrees of freedom, disregarding any effect due to static or quasi-static disorder. When addressing optical spectra, disorder enters the RB model as pure dephasing, introducing an additional relaxation channel for coherences.[109] Since optical spectra are governed by coherences, this simple approach works well at least for linear optical spectra (more subtle phenomena occurs for non-linear optical spectra). To address non-radiative rates, however, we need information on the population dynamics and, since in the Bloch approximation coherence and population dynamics are effectively decoupled, the pure dephasing approach that works well for optical spectra is totally ineffective on non-radiative rates, as shown in Fig. 2.23. In the same figure, results obtained by a full-Redfield trajectory (*i.e.* without decoupling coherences and populations) also show that adding pure-dephasing does not appreciably affects non-radiative rates.

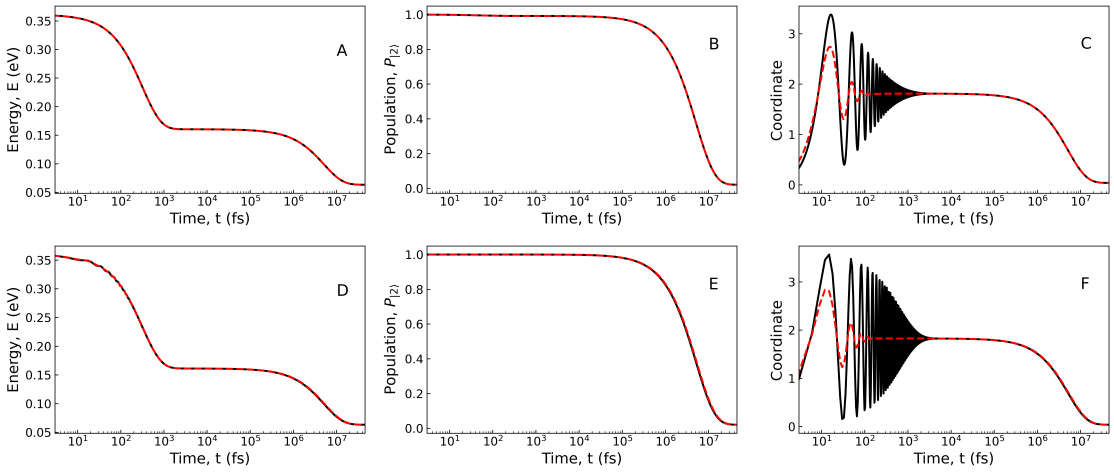

Figure 2.23: Introducing pure dephasing in the RB (top panels) and full Redfield (bottom panels) calculations. Black lines show standard RB or full Redfield dynamics, without any source of pure dephasing. Red dashed lines show dynamics obtained introducing dephasing is accounted in terms of a damping of the coherences (specifically adding a term -10γ to the $R_{ab,ab}$ terms of the Redfield tensor). The time evolution of the system energy, of teh population of state $|2\rangle$ and of the vibrational coordinate (C, F) are shown in the left, middle and right panles, respectively. Results refer to a system with $E_{ad} = 0.1\,\text{eV}$, $\hbar\omega = 0.12\,\text{eV}$, $\epsilon = 0.2\,\text{eV}$, adopting a constant spectral density with $\gamma = 3.16 \times 10^{-3}\,\text{fs}^{-1}$.

More accurate approaches are needed to properly account for disorder in the calculation of non-radiative rates in the Redfield or RB approaches. For static disorder, the relevant dynamics should be calculated on several replicas of the system to properly sample the disorder. Dealing with slow dynamic disorder is even more complex and typically requires mixed approaches where the system quantum dynamics is coupled with the classical dynamics associated with the slow coordinate. Polar solvation is a well-known source of inhomogeneous broadening and its dynamics is well captured by the Smoluchowsky equation:[109] a mixed Redfield-Smoluchowsky approach proved adequate to describe time-dependent optical spectra of polar dyes in

solution or amorphous matrices.[42, 110] Of course, these approaches rely on specific models for disorder.

Slow environmental degrees of freedom or slow molecular motions not explicitly included in the GF equation are possible sources of disorder to be considered in the GF approach. Several properties of the system can be affected, including *e.g.* vibrational frequencies and displacements, the adiabatic gap, etc. Again, once a proper model for the disorder is defined, a lengthy but reliable approach would rely on the calculation of the GF function averaging over an ensemble of replicas, representative of the disorder.

In the specific case where static disorder only affects the adiabatic gap, the inhomogenously broadened rate-spectra can be obtained by simply convoluting the bare spectra by a proper function representative of disorder, typically a gaussian function for white noise. Quite interestingly, this amounts to a gaussian apodization of the GF function, suggesting that, when a gaussian or an *equivalent* Blackman-Harris function is adopted, one implicitly imposes a white noise on the adiabatic gap. Fig. 2.24 shows the rate-spectra obtained convoluting the bare spectra in Figs. 2.3 and 2.7, respectively, with those obtained upon convolution with gaussian functions of different widths. As expected, the spectra become broader with increasing disorder, but the important point is that the calculated rates vary considerably depending on the amount of disorder introduced in the model. Again, damping the GF signal (or in other terms, apodizing it) is not an innocent numerical trick; it has a very fundamental physical meaning as it accounts for homogeneous and/or inhomogeneous broadening. Educated choices of the damping function are needed that cannot be left to the default choices of computational codes.

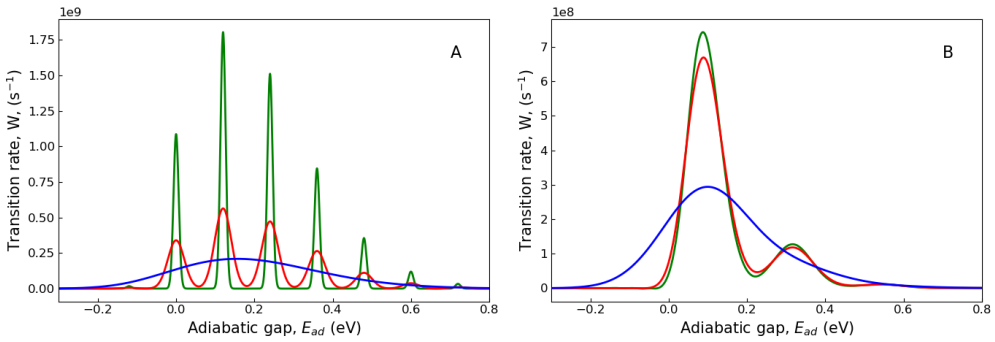

Figure 2.24: Panels A and B show rate-spectra calculated for the system in Fig. 2.3 and in Fig. 2.7, respectively. Green lines: bare spectra, red lines: spectra convoluted by a gaussian with $\sigma = 0.02\,\text{eV}$, blue lines: spectra convoluted by a gaussian with $\sigma = 0.10\,\text{eV}$.

2.7 Conclusions

Non-radiative rates govern the fate of excited states and hence the photophysics of molecular systems and must be properly addressed to model several processes of fundamental and technological relevance, including fluorescence, delayed fluorescence, phosphorescence, excited state absorption spectra, etc. Estimating non-radiative rates unavoidably requires to deal with open quantum systems. The popular GF approach, as implemented in several software packages, relies on the ssFGR that, strictly speaking, applies to closed quantum system and hence would only allow for non-radiative transitions between degenerate states. The computational strategy to overcome this issue goes via a FT and a inverse-FT and, in the process, the introduction of an apodization function makes the trick of opening the closed quantum system. Relying on the displaced oscillator model as the simplest model for non-radiative rates, we discussed how rates can be obtained in the RB approach, a truly open quantum system approach, following the population/de-population dynamics of relevant states. A direct comparison between the GF and RB results is tricky. A blended approach, ND, is then introduced to better compare the physics underlying the GF and RB approaches. Specifically, recognizing that the oscillating terms of the FT in the FGR expression are the coherences of the density matrix, we applied, to each oscillating term, the same exponential damping obtained from the RB approach. The comparison between the two approaches sheds light on the need to account for different relaxation times for different coherences at least in systems where inhomogeneous broadening can be neglected. The GF approach, either in its original version or in the ND version proposed here, suffers of some inconsistency, that shows up with an anomalous dependence of the rates on the width of the apodization function. Fast apodization implies faster relaxation and hence stronger system-bath coupling. Indeed, the RB dynamics shows rates that consistently increase with the strength of system-bath coupling. This is not always the case in GF-based approaches, where deviations of the ratio of the upward and downward rates from the thermodynamic limit are also observed in some parameter range.

Inhomogeneous broadening, as due to the interaction with static or quasi-static environmental degrees of freedom, represents another source of spectral broadening. We showed that the standard approach adopted to simulate optical spectra in the RB approach does not apply to rates. More to the point, reliable approaches to inhomogeneous broadening require specific models for disorder. In the GF approach, a gaussian apodization of the signal corresponds to a gaussian convolution of the rate-spectra and offers a very simple way to account for disorder in terms of a (gaussian) distribution of the energy of the adiabatic gap.

The problems related to the GF approach are definitely over-emphasized in the displaced oscillator model discussed here. The GF of large and flexible molecules, where many vibrational modes are coupled (possibly to the second order) to the electronic system, have very long recurrence times, so that the precise choice of the apodization function can be less critical. However, it is important to recognize that a truly *ab initio* estimate of non-radiative rates is not possible for some very fundamental reason: transitions occurring between non-degenerate states in fact require the interaction of the system with the environment as to allow for energy exchange

and this interaction, quite unavoidably, enters the model in a phenomenological way. In the GF approach, the system-bath interaction is hidden in the inverse FT step from the GF to the rate-spectra and, specifically, on the definition of the observation time-window (or in other terms in the choice of the apodization function). Once this fundamental issue is understood, educated choices for the apodization function can be made, to simulate in a rough way homogeneous and/or inhomogeneous broadening as relevant to the system at hand.

Chapter 3

2D IR Spectroscopy

3.1 The technique

Two-dimensional infrared spectroscopy (in short 2D IR spectroscopy) is an interesting technique that, measuring the nonlinear third order response function, provides important information, well beyond standard vibrational spectroscopic techniques like infrared absorption or Raman scattering. In 2D IR spectroscopy, infrared spectra are spread into a second dimension, offering information on vibrational couplings and homogeneous/inhomogeneous dynamics, providing a powerful tool for studying molecular structures, environmental dynamics driven by the surrounding medium, and structural kinetics of isomerization processes or fast atomic motions between chemical species. The environment also affects the system by changing its characteristic frequencies, and these tiny fluctuations can be explored through this technique.

2D IR exploits three excitation pulses (I, II, III as schematically illustrated in Fig. 3.1) to generate a nonlinear polarization in the sample. The first two pulses (I and II) are used to excite the sample, while the third pulse (III) probes the sample. More in detail, a double Fourier transform on t_1 and t_3 spreads the signal on two frequency axes, ω_1, the so called pump frequency, and ω_3, the probe frequency. The 2D spectra are typically recorded as a function of t_2, the so-called waiting time. It is the evolution of the spectra along t_2 that provides information on the dynamics of the system.

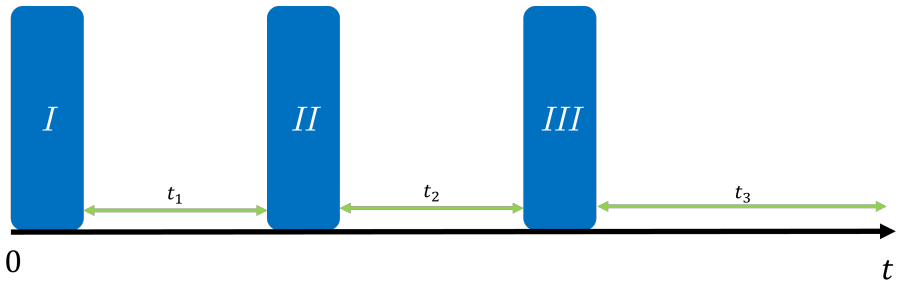

Figure 3.1: Pictorial scheme of a typical three pulses 2D experiment.

In a 2D IR experiment, overtone and combination bands can be observed along with the fundamental transitions of the system, so that detailed information about

the anharmonicity of the vibrational modes is obtained. Furthermore, vibrational modes concerning physically close atoms are correlated and information about the couplings can be obtained by analyzing the cross peaks of the 2D IR spectra. Of special interest for this work is the sensitivity of vibrational modes to the polarity of the environment[42, 111–113]: investigating the effect of the surrounding on the 2D-IR spectra offers important information on the delicate solute-solvent interplay and on its dynamics. However, in this context, available theoretical approaches to 2D-IR suffer important limitations. Specifically, the inhomogenous broadening induced by polar solvation is most often accounted for in terms of line-broadening, missing the subtleties of a phenomenon that may offer important information on the dynamics of the relaxation of the environment (either a solution or a solid matrix). In this chapter, we will set the basis to develop an original approach to the simulation of 2D IR. The idea is to calculate the evolution of the density matrix in the waiting time, exploiting the Redfield-Smoluchowski approach, a strategy developed in the host laboratory to calculate the intertwined dynamics of the molecular system and its environment[42, 99, 114].

3.2 Theoretical approaches

3.2.1 Direct approach to the third order NLO response

To simulate the 2D IR spectra, the time-evolution of the third order macroscopic polarization must be calculated, typically relying on the calculation of the time-evolution of the density matrix of the system, which interacts with a well defined sequence of infrared laser pulses. The general time-dependent Hamiltonian reads:

$$\mathbf{H}(t') = \mathbf{H}_0 + \mathbf{V}(t') \tag{3.1}$$

where $\mathbf{H}_0$ is the Hamiltonian of the system and $\mathbf{V}(t')$ describes the interaction of the system with the light. In the dipole (long-wavelength) approximation the light-matter interaction is written as:

$$\mathbf{V}(t') = -\boldsymbol{\mu} \cdot \mathbf{F}(t') \tag{3.2}$$

where $\boldsymbol{\mu}$ and $\mathbf{F}(t')$ are the dipole moment vector and the electric field vector, respectively. The dynamics of the system can be described in terms of the density matrix $\boldsymbol{\rho}(t)$ that obeys the Liouville–von Neumann equation:

$$\frac{\partial \boldsymbol{\rho}(t)}{\partial t} = -\frac{i}{\hbar}\left[\mathbf{H}(t), \boldsymbol{\rho}(t)\right] \tag{3.3}$$

The density matrix $\boldsymbol{\rho}(t)$ at time t can be written as a perturbative expansion:

$$\boldsymbol{\rho}(t) = \boldsymbol{\rho}^{(0)}(t) + \boldsymbol{\rho}^{(1)}(t) + \boldsymbol{\rho}^{(2)}(t) + ... + \boldsymbol{\rho}^{(n)}(t) + ... \tag{3.4}$$

where $\boldsymbol{\rho}^0(t)$ is the density matrix before the application of the perturbation. The generic correction to the *n-th* order, $\boldsymbol{\rho}^{(n)}(t)$ can be calculated from the *(n-1)-th* order correction, as follows:

$$\boldsymbol{\rho}^{(n)}(t) = \left(\frac{1}{i\hbar}\right) \int_0^t [\mathbf{V}(t'), \boldsymbol{\rho}^{(n-1)}(t')] dt' \tag{3.5}$$

where $\mathbf{V}(t')$ is the perturbation acting during the time interval $[0, t]$.

Once the analytical form of the electric field and the initial conditions of the system (i.e. $\boldsymbol{\rho}^{(0)}(t)$) are defined, the time evolution of the density matrix to any perturbative order can be calculated. In the simplest approach, the electric field is modeled as an impulsive perturbation, so that the perturbative Hamiltonian in Eq. 3.2 reads:

$$V(t') = -\hat{\mu}_F F_0 \delta(t' - t_0) \tag{3.6}$$

where $\hat{\mu}_F$ is the component of the dipole moment operator along the direction of the applied field, F_0 is the field intensity and $\delta(t' - t_0)$ is the Dirac delta function centered at t_0.

To our aims, the linear response to each pulse is enough to get the required third order NLO response. Specifically, in the most direct approach, at each pulse we only account for the linear term of the expansion in Eq. 3.4 and evolve only this term up to the next pulse, obtaining, after the three pulses in sequence, the final density matrix, that, traced over the dipole moment operator gives the needed third order response. Specifically, once the third order density matrix is obtained, $\boldsymbol{\rho}^{(3)}(t_1, t_2, t_3)$, the non-linear response function $R(t_1, t_2, t_3)$ is given by the trace of the matrix obtained as the product of the density matrix and the dipole moment matrix:

$$R(t_1, t_2, t_3) = \mathrm{Tr}[\boldsymbol{\mu}\, \boldsymbol{\rho}^{(3)}(t_1, t_2, t_3)] \tag{3.7}$$

Here and in the following, for the sake of simplicity, we have dropped the indices referring to the direction of the applied field (strictly speaking $\boldsymbol{\rho}^{(3)}$ has three indices, referring to the polarization of the incoming field). Finally, the 2D IR signal is evaluated at different t_2 waiting times as the double inverse Fourier transform of the response function, multiplied by the imaginary unit, as follows:

$$S(\omega_1, t_2, \omega_3) = \int_0^{+\infty} \int_0^{+\infty} iR(t_1, t_2, t_3) e^{i\omega_1 t_1} e^{i\omega_3 t_3} dt_1 dt_3 \tag{3.8}$$

The interpretation of such spectra is complicated by the peak broadening, which induces the so-called *phase twist*. This issue becomes particularly pronounced in systems with multiple vibrational modes. A possible way to simplify the analysis is to remove the phase by taking the absolute value of spectra, at the price of possible appearance of interferences.[115]

To address this issue, it is recommended to plot, at each t_2 waiting time, the purely absorptive 2D spectrum obtained as the real part of the sum of $S(-\omega_1, \omega_3)$ and $S(\omega_1, \omega_3)$, canceling out the phase twists:

$$S_{abs}(\omega_1, \omega_3) = \mathrm{Re}\{S(-\omega_1, \omega_3) + S(\omega_1, \omega_3)\} \tag{3.9}$$

3.2.2 Direct approach in the case of a two-level system

Here we show the form of the response function for a two-level system characterized by an energy gap $\hbar\omega$ and by the following dipole moment matrix

$$\boldsymbol{\mu} = \begin{pmatrix} 0 & \mu_{01} \\ \mu_{10} & 0 \end{pmatrix} \tag{3.10}$$

To simplify the math without losing physical meaning, we adopt the following assumptions:

I. The system is prepared with the whole population in the ground state;

II. $\mu_{01} = \mu_{10}$;

III. The perturbation induced from the electric field is treated as a Dirac delta pulse;

IV. The density matrix expansion is truncated to the first perturbative order;

V. During the t_1, t_2, t_3 time evolution steps, coherences undergo dephasing while population relaxation is neglected, so that the populations of the states do not change in time.

Given a generic density matrix

$$\boldsymbol{\rho}^{(0)} \equiv \begin{pmatrix} a & b \\ c & d \end{pmatrix} \tag{3.11}$$

the first order correction to the density matrix is evaluated as:

$$\begin{aligned} \boldsymbol{\rho}^{(1)} &= \left(\frac{1}{i\hbar}\right) \int_{-\infty}^{t} \left[-\boldsymbol{\mu} F_0 \delta(t' - t_0), \boldsymbol{\rho}^{(0)}\right] dt' \\ &= -F_0 \mu_{10} \left(\frac{1}{i\hbar}\right) \int_{-\infty}^{t} \delta(t' - t_0) \left[\begin{pmatrix} 0 & 1 \\ 1 & 0 \end{pmatrix}, \begin{pmatrix} a & b \\ c & d \end{pmatrix} \right] dt' \\ &= iF_0 J \mu_{10}/\hbar \begin{pmatrix} c-b & d-a \\ a-d & b-c \end{pmatrix} \end{aligned} \tag{3.12}$$

where J is the following integral

$$J = \int_{-\infty}^{t} \delta(t' - t_0) dt' \tag{3.13}$$

Gathering all prefactors in the dimensionless term A, we write:

$$A = \frac{J F_0 \mu_{10}}{\hbar} \tag{3.14}$$

and the first order correction to the generic density matrix can be written as:

$$\boldsymbol{\rho}^{(1)} = iA \begin{pmatrix} c-b & d-a \\ a-d & b-c \end{pmatrix} \tag{3.15}$$

Starting from the system prepared with the whole population in the ground state ($a = 1$, $b = c = d = 0$), after the first pulse, the first order correction reads:

$$\boldsymbol{\rho} = \begin{pmatrix} 0 & -iA \\ iA & 0 \end{pmatrix} \tag{3.16}$$

The time-evolution of the system along t_1 is simplified as:

$$\rho_{ab}(t_1) = \rho_{ab}(t_0) \exp\left\{ \left(i\omega_{ba} t_1 - \frac{t_1}{T_2} \right) \right\} \tag{3.17}$$

$$\rho_{aa}(t_1) = \rho_{aa}(t_0) \tag{3.18}$$

where T_2 is the relaxation time of the coherences. After the first pulse, the density matrix is:

$$\boldsymbol{\rho}(t_1) = \begin{pmatrix} 0 & -iAe^{i\omega t_1 - t_1/T_2} \\ iAe^{-i\omega t_1 - t_1/T_2} & 0 \end{pmatrix} \tag{3.19}$$

and after the second pulse we get:

$$\rho_{00}(t_1) = -A^2 \left(e^{-i\omega t_1 - t_1/T_2} + e^{i\omega t_1 - t_1/T_2} \right) \tag{3.20}$$

$$\rho_{01}(t_1) = \rho_{10}(t_1) = 0 \tag{3.21}$$

$$\rho_{11}(t_1) = 1 + A^2 \left(e^{-i\omega t_1 - t_1/T_2} + e^{i\omega t_1 - t_1/T_2} \right) \tag{3.22}$$

The second pulse turns coherences into populations, so that, during the waiting time, there is no dephasing (we are not accounting for depopulation that would only imply a progressive damping of the signal). Finally, the third pulse leads to:

$$\rho_{00}(t_1) = \rho_{11}(t_1) = 0 \tag{3.23}$$

$$\rho_{01}(t_1) = iA \left[2A^2 (e^{i\omega t_1 - t_1/T_2} + e^{-i\omega t_1 - t_1/T_2}) \right] \tag{3.24}$$

$$\rho_{10}(t_1) = \rho_{01}^{\dagger}(t_1) \tag{3.25}$$

The time evolution of the density matrix along t_3 then gives:

$$\begin{aligned} \rho_{01}(t_1, t_3) &= iAe^{i\omega t_3 - t_3/T_2} \left[2A^2 (e^{i\omega t_1 - t_1/T_2} + e^{-i\omega t_1 - t_1/T_2}) \right] \\ &= 2iA^3 (e^{i\omega t_3 - t_3/T_2})(e^{-t_1/T_2})(2\cos(\omega t_1)) \\ &= \left[4A^3 \cos(\omega t_1) e^{-(t_1+t_3)/T_2} \right] e^{i\omega t_3} \end{aligned} \tag{3.26}$$

$$\rho_{10}(t_1, t_3) = \left[4A^3 \cos(\omega t_1) e^{-(t_1+t_3)/T_2} \right] e^{-i\omega t_3} \tag{3.27}$$

while populations are not changing. Recalling Eq. 3.7, the response function becomes:

$$\begin{aligned} R(t_1, t_3) &= \mu_{10} \left[\rho_{01}(t_1, t_3) + c.c. \right] \\ &= 2\mu_{10} \, \mathrm{Re}\{ \rho_{01}(t_1, t_3) \} \\ &= 8\mu_{10} A^3 \cos(\omega t_1) \cos(\omega t_3) e^{-(t_1+t_3)/T_2} \end{aligned} \tag{3.28}$$

We notice that, if at each pulse we only maintain the linear correction to the density matrix, after the third pulse, only the third order response ($\propto A^3$) is calculated.

The inverse Fourier transform of Eq. 3.28 (multiplied by the imaginary unit), leads precisely to the equations derived by Hamm and Zanni in Ref. [115], for the case of a two-level system.

3.2.3 Propagating the density matrix

The direct approach, described in the previous section, immediately yields the third order NLO response. However, since at each step only the linear correction to the density matrix is accounted for, we do not have access to the full density matrix. Accordingly, the propagation of the density matrix can only be inserted phenomenologically, accounting for an exponential decay of the coherences with characteristic time T_2 and (possibly) an exponential decay of the populations, with a characteristic time T_1. If a more realistic evolution of the density matrix is required, as needed to properly account for the solute-solvent interaction, we need to propagate the full density matrix. We therefore propose a *complete perturbative* approach where, once again at each pulse the density matrix is expanded up to the linear term, but we maintain and propagate the full density matrix, corrected to the first perturbative order $\boldsymbol{\rho}^{(0)} + \boldsymbol{\rho}^{(1)}$. The price to be paid is that, in addition to these contributions to the response, extra terms arise at different perturbative orders, making it necessary to carefully single out the third-order response. Here we illustrate the approach in detail, deriving the expressions for the same two-level system addressed in the previous section via the direct perturbative approach.

Exploiting Eq. 3.15 to calculate the effect of a pulse on the generic density matrix in Eq. 3.11 we obtain the full density matrix corrected up to the first perturbative order, as follows:

$$\boldsymbol{\rho} = \rho^{(0)} + \rho^{(1)} = \begin{pmatrix} a + iA(c-b) & b + iA(d-a) \\ c + iA(a-d) & d + iA(b-c) \end{pmatrix} \tag{3.29}$$

If the system is prepared before the perturbation in the lowest energy state, so that $a = 1$ and $b = c = d = 0$, the density matrix after the first pulse reads

$$\rho = \begin{pmatrix} 1 & -iA \\ iA & 0 \end{pmatrix} \tag{3.30}$$

The time evolution of the density matrix along t_1 gives:

$$\boldsymbol{\rho}(t_1) = \begin{pmatrix} 1 & -iAe^{i\omega t_1 - t_1/T_2} \\ iAe^{-i\omega t_1 - t_1/T_2} & 0 \end{pmatrix} \tag{3.31}$$

and after the second pulse, we get:

$$\rho_{00}(t_1) = 1 - A^2(e^{-i\omega t_1 - t_1/T_2} + e^{i\omega t_1 - t_1/T_2}) \equiv a' \tag{3.32}$$

$$\rho_{01}(t_1) = -2iA \equiv b' \tag{3.33}$$

$$\rho_{10}(t_1) = 2iA \equiv c' \tag{3.34}$$

$$\rho_{11}(t_1) = A^2(e^{-i\omega t_1 - t_1/T_2} + e^{i\omega t_1 - t_1/T_2}) \equiv d' \tag{3.35}$$

The system evolves during t_2 and the density matrix becomes:

$$\boldsymbol{\rho}(t_1, t_2) = \begin{pmatrix} a' & b'e^{i\omega t_2 - t_2/T_2} \\ c'e^{-i\omega t_2 - t_2/T_2} & d' \end{pmatrix} \tag{3.36}$$

The third pulse leads to the final density matrix elements:

$$\begin{aligned}\rho_{00}(t_1,t_2) &= a' + iA\left[c'e^{-i\omega t_2 - t_2/T_2} - b'e^{i\omega t_2 - t_2/T_2}\right] \\ &= 1 - A^2(e^{-i\omega t_1 - t_1/T_2} + e^{i\omega t_1 - t_1/T_2}) + \\ &+ iA\left[2iAe^{-i\omega t_2 - t_2/T_2} + 2iAe^{i\omega t_2 - t_2/T_2}\right] \\ &= 1 - A^2(2\cos(\omega t_1)e^{-t_1/T_2} + 4\cos(\omega t_2)e^{-t_2/T_2}) \\ &\equiv a'' \end{aligned} \tag{3.37}$$

$$\begin{aligned}\rho_{01}(t_1,t_2) &= b'e^{i\omega t_2 - t_2/T_2} + iA(d' - a') \\ &= -2iAe^{i\omega t_2 - t_2/T_2} + iA\left[2A^2(e^{-i\omega t_1 - t_1/T_2} + e^{i\omega t_1 - t_1/T_2}) - 1\right] \\ &= -2iAe^{i\omega t_2 - t_2/T_2} - iA + 4iA^3\cos(\omega t_1)e^{-t_1/T_2} \\ &= iA(4A^2\cos(\omega t_1)e^{-t_1/T_2} - 2e^{i\omega t_2 - t_2/T_2} - 1) \\ &\equiv b'' \end{aligned} \tag{3.38}$$

$$\rho_{10}(t_1,t_2) = \rho_{01}^{\dagger}(t_1,t_2) \tag{3.39}$$

$$\rho_{11}(t_1,t_2) = A^2(2\cos(\omega t_1)e^{-t_1/T_2} + 4\cos(\omega t_2)e^{-t_2/T_2}) \tag{3.40}$$

The density matrix evolution along t_3 then makes the coherences oscillate according to:

$$\rho_{01}(t_1,t_2,t_3) = b''e^{i\omega t_3 - t_3/T_2} \tag{3.41}$$

$$\rho_{10}(t_1,t_2,t_3) = \rho_{01}^{\dagger}(t_1,t_2,t_3) \tag{3.42}$$

while the populations remain constant. The response function is then given by:

$$\begin{aligned}R(t_1,t_2,t_3) &= \mu_{01}b''e^{i\omega t_3 - t_3/T_2} + \mu_{10}\left(b''e^{i\omega t_3 - t_3/T_2}\right)^{\dagger} \\ &= 2\mu_{01}\,\mathrm{Re}\left\{b''e^{i\omega t_3 - t_3/T_2}\right\} \\ &= 2\mu_{01}e^{-t_3/T_2}\,\mathrm{Re}\left\{iAe^{i\omega t_3}(4A^2\cos(\omega t_1)e^{-t_1/T_2} - 2e^{i\omega t_2 - t_2/T_2} - 1)\right\} \\ &= -2\mu_{01}Ae^{-t_3/T_2}\,\mathrm{Im}\left\{e^{i\omega t_3}(4A^2\cos(\omega t_1)e^{-t_1/T_2} - 2e^{i\omega t_2 - t_2/T_2} - 1)\right\} \\ &= -2\mu_{01}Ae^{-t_3/T_2}\times \\ &\times\left[\sin(\omega t_3)(4A^2\cos(\omega t_1)e^{-t_1/T_2} - 1) - 2e^{-t_2/T_2}\sin(\omega(t_2+t_3))\right] \end{aligned} \tag{3.43}$$

The double inverse Fourier transform of Eq. 3.43, multiplied by the imaginary unit, leads to the total 2D IR signal:

$$S(\omega_1,t_2,\omega_3) = q_1(\omega_1,t_2,\omega_3)A + q_3(\omega_1,t_2,\omega_3)A^3 \tag{3.44}$$

where

$$q_1(\omega_1,t_2,\omega_3) = \delta(\omega_1)\Bigg\{ - \mu_{01}T_2\left[\frac{1}{1 - i(\omega_3+\omega)T_2} - \frac{1}{1 - i(\omega_3-\omega)T_2}\right] \tag{3.45}$$

$$+ 4i\mu_{01}T_2e^{-t_2/T_2}\left[\frac{(\cos(\omega t_2) + \sin(\omega t_2))}{1 - i(\omega_3+\omega)T_2}\right. \tag{3.46}$$

$$\left.+ \frac{(-\cos(\omega t_2) + \sin(\omega t_2))}{1 - i(\omega_3-\omega)T_2}\right]\Bigg\} \tag{3.47}$$

$$q_3(\omega_1, t_2, \omega_3) = 2\mu_{01}T_2^2 \left[\frac{1}{1 - i(\omega_1 + \omega)T_2} + \frac{1}{1 - i(\omega_1 - \omega)T_2}\right] \times$$
$$\times \left[\frac{1}{1 - i(\omega_3 + \omega)T_2} - \frac{1}{1 - i(\omega_3 - \omega)T_2}\right] \tag{3.48}$$

At variance with the direct approach described in the previous section, if the whole density matrix is considered, we obtain the linear term in the field intensity summed over the cubic term, which is the term we need to estimate. So we need a way, in the actual calculation, to separate the two contributions. To this aim, we run the 2D IR simulation at two different values of the field intensity and, for each point of the three dimensional grid $[\omega_1, t_2, \omega_3]$, we solve the linear system of equations for q_3.

While promising, this strategy does not fully solve the problem of propagating in time a *well-behaved* density matrix. If needed, the relaxation dynamics must be properly addressed via open quantum systems approaches and specifically, for our aims, via the Redfield-Smoluchowski approach, to deal with the system dynamics entangled with the environmental dynamics[42, 99, 114]. The problem is that the density matrix expanded to the first perturbative order (see e.g. Eq. 3.30) does not fulfill the stringent mathematical restrictions of well-behaved density matrices requiring that:

$$\sum_k \rho_{kk}(t) = 1 \tag{3.49}$$

$$\rho_{kj}(t)\rho_{jk}(t) \leq \sqrt{\rho_{kk}(t)\rho_{jj}(t)} \tag{3.50}$$

This problem can be circumvented expanding the density matrix up to the second perturbative order or equivalently applying two pulses at each interaction while expanding the density matrix at the first perturbative order. As seen in the detailed derivation reported in appendix B for the same two-state system discussed above, along these lines, contributions up to the fifth order in the field are obtained. Following a similar (even if slightly more complex) strategy, as outlined above to disentangle linear and third order terms, we can again single out the pure third order contributions. The delicate issue is the appearance of spurious terms at the third order, terms that correspond to the "pump-probe" experiment and not to a true 2D IR. Specifically, in these spurious third order terms, instead of interacting with three different pulses, the system interacts twice with the same pulse. While we are considering strategies to address this issue, the results are too preliminary to be inserted here. In the following, we will summarize the preliminary results towards the detailed analysis of 2D-IR spectra of phenol blue (PB), a dye whose vibrational spectra shows a well pronounced and well understood solvatochromism.[111–113]

3.3 Preliminary results: the case of phenol blue

3.3.1 The model

The essential states model (ESM) for phenol blue (Fig. 3.2), a typical donor-acceptor dye, was derived several years back[111–113] and is summarized here.

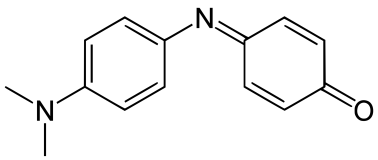

Figure 3.2: Molecular structure of Phenol blue.

The low energy spectra of the molecule can be described in terms of two diabatic states, a neutral, DA ($|N\rangle$) and a zwitterionic state, D^+A^- ($|Z\rangle$), separated by an energy gap $2z$ and mixed by a matrix element $\sqrt{2}t$. To simulate the vibrational spectra of phenol blue, up to two harmonic vibrational modes are considered, accounting for linear and quadratic coupling. Specifically, we account for the displacement of the vibrational coordinates when going from the $|N\rangle$ to the $|Z\rangle$ state (linear coupling) as well as for the variation of the frequency (quadratic coupling). The vibrational Hamiltonians for the $|N\rangle$ and $|Z\rangle$ states can be written in terms of the relevant creation and annihilation operators:

$$\hat{H}_{\mathrm{vib},N} = \sum_k \hbar\omega_k \left(\hat{a}_k^\dagger \hat{a}_k + \frac{1}{2}\right) \tag{3.51}$$

$$\hat{H}_{\mathrm{vib},Z} = \sum_k \hbar\tilde{\omega}_k \left(\hat{\tilde{a}}_k^\dagger \hat{\tilde{a}}_k + \frac{1}{2}\right) \tag{3.52}$$

where $\hat{a}_k$ and $\hat{\tilde{a}}_k$ are the annihilation operator for the k-th phonon on the $|N\rangle$ and $|Z\rangle$ potential energy surfaces, respectively, and ω_k and $\tilde{\omega}_k$ are the respective frequencies. The quadratic coupling is introduced on the diabatic states in the simplest approach, only accounting for the different frequencies associated with the $|N\rangle$ and $|Z\rangle$ states. Specifically, on this basis, we do not introduce explicitly neither the Duschinsky coupling (mode mixing) nor the anharmonicity. However, the mode mixing and the anharmonicity will be naturally recovered in the adiabatic basis.
It is useful to express the phonon operator for the $|Z\rangle$ state in terms of the phonon operators of the $|N\rangle$ states. To such an aim, we write the phonon operators in terms of the mass weighted coordinate and momentum operators ($\hat{q}_k$ and $\hat{p}_k$ respectively) as follows, for the $|N\rangle$ state:

$$\hat{a}_k = \sqrt{\frac{\omega_k}{2\hbar}}\left(\hat{q}_k + \frac{i}{\omega_k}\hat{p}_k\right), \quad \hat{a}_k^\dagger = \sqrt{\frac{\omega_k}{2\hbar}}\left(\hat{q}_k - \frac{i}{\omega_k}\hat{p}_k\right) \tag{3.53}$$

and for the $|Z\rangle$ state:

$$\hat{\tilde{a}}_k = \sqrt{\frac{\tilde{\omega}_k}{2\hbar}}\left(\hat{\tilde{q}}_k + \frac{i}{\tilde{\omega}_k}\hat{\tilde{p}}_k\right), \quad \hat{\tilde{a}}_k^\dagger = \sqrt{\frac{\tilde{\omega}_k}{2\hbar}}\left(\hat{\tilde{q}}_k - \frac{i}{\tilde{\omega}_k}\hat{\tilde{p}}_k\right). \tag{3.54}$$

To account for the linear coupling, we set

$$\hat{\tilde{p}}_k = \hat{p}_k \qquad \hat{\tilde{q}}_k = \hat{q}_k - \Delta_k \tag{3.55}$$

where Δ_k is the displacement of the k-th vibrational mode. The creation operator for the zwitterionic state can thus be written as:

$$\begin{aligned}
\hat{\tilde{a}}_k &= \sqrt{\frac{\tilde{\omega}_k}{2\hbar}}\left(\hat{\tilde{q}}_k + \frac{i}{\tilde{\omega}_k}\hat{\tilde{p}}_k\right) \\
&= \sqrt{\frac{\tilde{\omega}_k}{2\hbar}}\left(\hat{q}_k - \Delta_k + \frac{i}{\tilde{\omega}_k}\hat{p}_k\right) \\
&= \frac{1}{2}\sqrt{\frac{\tilde{\omega}_k}{\omega_k}}(\hat{a}_k^\dagger + \hat{a}_k) - \sqrt{\frac{\tilde{\omega}_k}{2\hbar}}\Delta_k + \frac{1}{2}\sqrt{\frac{\omega_k}{\tilde{\omega}_k}}(\hat{a}_k - \hat{a}_k^\dagger)
\end{aligned} \tag{3.56}$$

Defining

$$\hat{\tilde{a}}_k = c_{1k}\hat{a}_k + c_{2k}\hat{a}_k^\dagger + c_{3k}, \quad \hat{\tilde{a}}_k^\dagger = c_{1k}\hat{a}_k^\dagger + c_{2k}\hat{a}_k + c_{3k} \tag{3.57}$$

where

$$c_{1k} = \frac{1}{2}\left(\sqrt{\frac{\tilde{\omega}_k}{\omega_k}} + \sqrt{\frac{\omega_k}{\tilde{\omega}_k}}\right), \quad c_{2k} = \frac{1}{2}\left(\sqrt{\frac{\tilde{\omega}_k}{\omega_k}} - \sqrt{\frac{\omega_k}{\tilde{\omega}_k}}\right), \quad c_{3k} = -\sqrt{\frac{\tilde{\omega}_k}{2\hbar}}\Delta_k. \tag{3.58}$$

and set

$$r_k = \frac{\tilde{\omega}_k}{\omega_k}, \quad \delta_k = \sqrt{\frac{\tilde{\omega}_k}{\hbar}}\Delta_k \tag{3.59}$$

we are able to write the set of Eqs. 3.58 as:

$$c_{1k} = \frac{1}{2}\left(\sqrt{r_k} + \sqrt{\frac{1}{r_k}}\right), \quad c_{2k} = \frac{1}{2}\left(\sqrt{r_k} - \sqrt{\frac{1}{r_k}}\right), \quad c_{3k} = -\frac{\delta_k}{\sqrt{2}} \tag{3.60}$$

so that

$$\begin{aligned}
\hat{\tilde{a}}_k^\dagger\hat{\tilde{a}}_k &= (c_{1k}\hat{a}_k^\dagger + c_{2k}\hat{a}_k + c_{3k})(c_{1k}\hat{a}_k + c_{2k}\hat{a}_k^\dagger + c_{3k}) \\
&= c_{1k}c_{2k}(\hat{a}_k^{\dagger 2} + \hat{a}_k^2) + (c_{2k}c_{3k} + c_{1k}c_{3k})(\hat{a}_k + \hat{a}_k^\dagger) + \\
&+ c_{2k}^2\hat{a}_k\hat{a}_k^\dagger + c_{1k}^2\hat{a}_k^\dagger\hat{a}_k + c_{3k}^2
\end{aligned} \tag{3.61}$$

Using the commutator relation, $\hat{a}_k\hat{a}_k^\dagger - \hat{a}_k^\dagger\hat{a}_k = 1$, and Eq. 3.61, the vibrational Hamiltonian for the zwitterionic state, Eq. 3.52, can be written as:

$$\begin{aligned}
\hat{H}_{\text{vib},Z} = &\sum_k \hbar\tilde{\omega}_k\left[c_{1k}c_{2k}(\hat{a}_k^{\dagger 2} + \hat{a}_k^2) + (c_{2k}c_{3k} + c_{1k}c_{3k})(\hat{a}_k + \hat{a}_k^\dagger)\right] + \\
&+ \sum_k \hbar\tilde{\omega}_k\left[(c_{2k}^2 + c_{1k}^2)\hat{a}_k^\dagger\hat{a}_k + \left(c_{3k}^2 + c_{2k}^2 + \frac{1}{2}\right)\right]
\end{aligned} \tag{3.62}$$

Simplifying the terms in the parenthesis, we get:

$$\begin{aligned}
c_{1k}c_{2k} &= \frac{r_k^2 - 1}{4r_k} & c_{2k}c_{3k} + c_{1k}c_{3k} &= -\delta_k\sqrt{\tfrac{r_k}{2}} \\
c_{2k}^2 + c_{1k}^2 &= \frac{r_k^2 + 1}{2r_k} & c_{3k}^2 + c_{2k}^2 + \tfrac{1}{2} &= \tfrac{1}{2}\left[\delta_k^2 + \tfrac{1}{2}\left(r_k + \tfrac{1}{r_k}\right)\right]
\end{aligned} \tag{3.63}$$

The vibrational Hamiltonian for the $|Z\rangle$ state becomes:

$$\hat{H}_{\text{vib},Z} = \sum_k \hbar\tilde{\omega}_k \left[\frac{r_k^2-1}{4r_k}(\hat{a}_k^{\dagger 2} + \hat{a}_k^2) - \delta_k\sqrt{\frac{r_k}{2}}(\hat{a}_k + \hat{a}_k^\dagger)\right] + \\ + \sum_k \hbar\tilde{\omega}_k \left[\frac{r_k^2+1}{2r_k}\hat{a}_k^\dagger\hat{a}_k + \frac{1}{2}\left(\delta_k^2 + \frac{r_k^2+1}{2r_k}\right)\right] \tag{3.64}$$

and finally the total Hamiltonian reads:

$$\begin{aligned}\hat{H}_{\text{tot}} &= \hat{H}_N + \hat{H}_Z + \hat{H}_{NZ} \\ &= \sum_k \hbar\omega_k \left(\hat{a}_k^\dagger\hat{a}_k + \frac{1}{2}\right)|N\rangle\langle N| + 2z\,|Z\rangle\langle Z| \\ &\quad + \sum_k \hbar\tilde{\omega}_k \left[\frac{r_k^2-1}{4r_k}(\hat{a}_k^{\dagger 2} + \hat{a}_k^2) - \delta_k\sqrt{\frac{r_k}{2}}(\hat{a}_k + \hat{a}_k^\dagger) + \frac{r_k^2+1}{2r_k}\hat{a}_k^\dagger\hat{a}_k\right]|Z\rangle\langle Z| + \\ &\quad + \sum_k \left[\frac{\hbar\tilde{\omega}_k\delta_k^2}{2} + \frac{\hbar\tilde{\omega}_k(r_k^2+1)}{4r_k}\right]|Z\rangle\langle Z| - \sqrt{2}t\,(|N\rangle\langle Z| + |Z\rangle\langle N|)\end{aligned} \tag{3.65}$$

To address optical spectra, we must define the dipole moment operator. In line with the standard ESM approach, we rely on the Mulliken approximation,[116] and consider a single non-vanishing matrix element for the dipole operator, μ_0, that measures the dipole moment of the zwitterionic state. Accordingly, the dipole moment operator is a purely electronic operator, the vibrational intensity is indeed borrowed from the electronic states. In the following, when entering the dipole moment operator, we always enter $\hat{\mu} - \langle\hat{\mu}\rangle$ as the operator relevant to optical spectroscopy.[117]

The Hamiltonian is written on the basis obtained as the direct product of the two electronic states times the first n states of each oscillator for a total of $2n^2$ states. The resulting matrix is diagonalized to obtain the non-adiabatic eigenstates that fully account for anharmonicity. The convergence of the results in terms of eigenvalues is ensured by setting large enough n (typically $n = 14$).

In the 2D experiment, only states with up to two vibrational quanta are involved, so that, for our aims, we will only consider the first three states (the ground, the one and two quanta state) for the system with a single vibrational mode. Introducing two vibrational modes, up to six states are required instead.

3.3.2 Computational details

The interaction between the system and the light is modeled using Dirac-δ pulses, as described in Eq. 3.6, expanding the density matrix to the first order of the perturbation theory. During the time intervals t_1, t_2 and t_3, only coherence dephasing is allowed, as discussed in Sec. 3.2.3, while population relaxation is neglected.

The response function in Eq. 3.7 is sampled on a grid of $n_t \times n_t$ equally spaced time points along the t_1 and t_3 axis, at several t_2 waiting times. The n-dimensional inverse Fourier transform (IFT) is computed using Python 3[118] default subroutine, *ifftn*, from the *numpy* module. The spectral resolution, E_{res} (set to $15\,\text{cm}^{-1}$ for all the simulations), impacts the computational cost of the simulation and is chosen so that the details about the anharmonicity of the vibrational states of the system can be

properly assessed. The response function is sampled with a time step small enough to satisfy the Nyquist–Shannon theorem, with the sampling time interval defined as $\Delta_t = (2\omega_{01})^{-1}$, where $\omega_{01} = \frac{E_1 - E_0}{\hbar}$ is the frequency of the lowest vibrational transition of the system, with E_j being the energy of the j-the eigenstate of the system.

The number of time points is directly determined once the variables E_{res} and Δt are defined, through the equation:

$$n_t = \frac{2h\omega_{01}}{E_{res}} \tag{3.66}$$

where h is the Planck's constant. The simulation of the spectra is performed setting the dephasing time T_2 to values specified below and sampling the waiting times.

As discussed in Sec. 3.2.3, the third order response can be singled out in a reliable way: the 2D IR spectra obtained employing the direct method or propagating the complete density matrix coincide within the limits of numerical precision. Thus, only the results obtained propagating the complete density matrix are shown in the following sections. As stated above, the appearance of spurious "pump-probe" terms at the third order, when introducing the second order correction to the density matrix hinders the possibility to adopt a realistic approach to the entangled system-solvent dynamics. This more ambitious goal will be pursued after the closing of my PhD.

3.3.3 The three level system

To start with, we introduce a single vibrational mode and diagonalize the Hamiltonian in Eq. 3.65, with the model parameters reported in Tab. 3.1. Only the first three eigenstates are of interest to calculate the 2D-IR spectra.

Parameter	**Value**	**Units**
$2z$	1.4	eV
$\sqrt{2}t$	1	eV
$\hbar\omega$	0.22	eV
$\hbar\tilde{\omega}$	0.16	eV
δ	3	
μ_0	14	D
T_2	150	fs

Table 3.1: Parameters of the model for the single mode system.

The six states have relative energies (in cm^{-1}) of 0, 1439 and 2738, listed in ascending order, while the dipole moment matrix (in D) is given by

$$\boldsymbol{\mu} = \begin{pmatrix} 0 & 0.9 & 0.28 \\ 0.9 & 0.87 & 1.72 \\ 0.28 & 1.72 & 1.94 \end{pmatrix}$$

At first, we computed the linear response of the system after the interaction with the first field, and the left panel of Fig. 3.3 shows the obtained dipole moment (the

linear signal) as a function of time, while the right panel of the same figure shows the inverse Fourier transform of the linear signal multiplied by the imaginary unit. The field intensity, which regulates the absolute value of the linear response (same for the spectra), was set to $F_0 = 10^{-1} eVD^{-1}$.

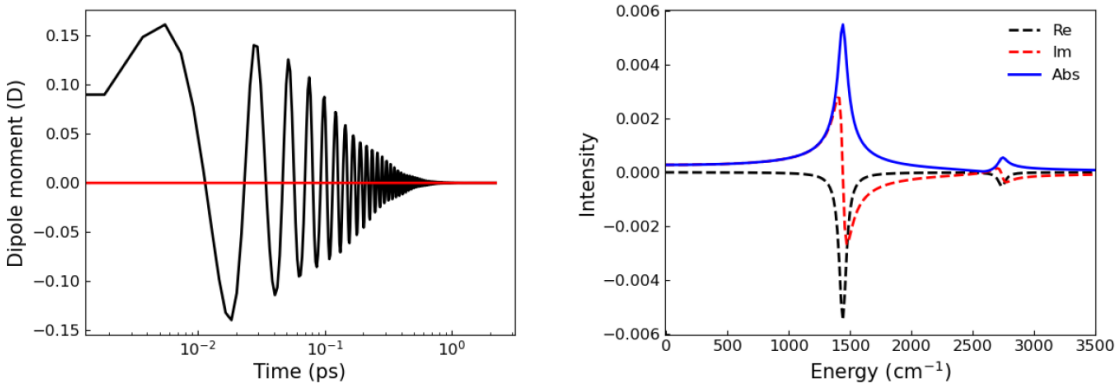

Figure 3.3: Left panel: Dipole moment as a function of time after the interaction with the first field. Right panel: Inverse Fourier transform (arbitrary units) of the dipole moment displayed in the left panel, multiplied by the imaginary unit. The dashed black and red curves denote the real and imaginary components, respectively, while the solid blue curve represents the magnitude. The field intensity was set to $F_0 = 10^{-1} eVD^{-1}$.

Apart from a sign, the black dashed line in the right panel of Fig. 3.3 corresponds to the absorption spectrum. The first more intense peak at $\sim 1440\,\mathrm{cm}^{-1}$ is associated to the fundamental transition:

$$v = 0 \quad \rightarrow \quad v = 1$$

where v is the vibrational quantum number. The second, less intense peak at $\sim 2740\,\mathrm{cm}^{-1}$ is instead related to the overtone transition:

$$v = 0 \quad \rightarrow \quad v = 2$$

The appearance of the overtone, at a frequency slightly lower than twice the frequency of the fundamental, confirms that the proposed model leads to sizable anharmonicity.

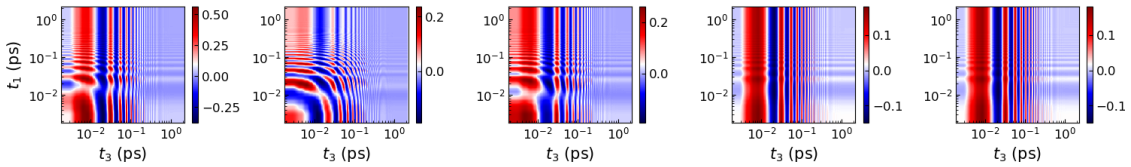

Figure 3.4: Response functions ($R(t_1, t_3)$ in Eq. 3.7) at different waiting times: from left to right, $t_2 = 0.001\,\mathrm{ps}$, $0.01\,\mathrm{ps}$, $0.1\,\mathrm{ps}$, $1\,\mathrm{ps}$, $10\,\mathrm{ps}$. The field intensity was set to $F_0 = 10^{-1}\, eVD^{-1}$.

The full simulation of the 2D IR experiment was then performed, and Fig. 3.4 shows the response functions at five different waiting times, with $F_0 = 10^{-1}\, eVD^{-1}$. At very short t_2, the 2D response function oscillates along t_1 and t_3 at the characteristic frequencies of the system, but as the waiting time increases (moving from left to

right of Fig. 3.4), the oscillations along t_1 are nearly absent, reflecting the loss of dynamical information associated with the coherences induced by the first electric field. For comparison purposes, Fig. 3.5 shows the response functions computed using a lower field intensity ($F_0 = 10^{-4} eVD^{-1}$). In this case, at long waiting times, the oscillations along t_1 are not visible since the absolute value of the coherences generated after the interaction with the first field is about three orders of magnitude lower than in the case of $F_0 = 10^{-1}\, eVD^{-1}$.

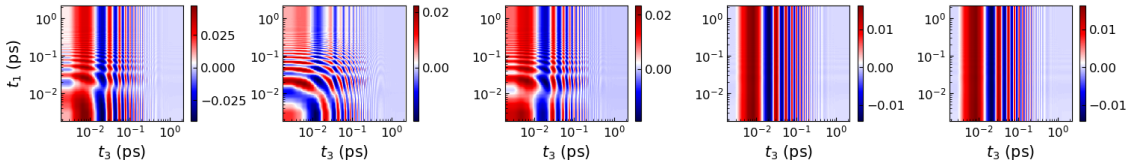

Figure 3.5: Response functions ($R(t_1, t_3)$ in Eq. 3.7) at different waiting times: from left to right, $t_2 = 0.001$ ps, 0.01 ps, 0.1 ps, 1 ps, 10 ps. The field intensity was set to $F_0 = 10^{-4}\, eVD^{-1}$.

The inverse 2D Fourier transform of the response functions (multiplied by the imaginary unit) in Figs. 3.4 and 3.5 are shown in Figs. 3.6. and 3.7, respectively. The inverse FT of the complete response function, $S(\omega_1, \omega_3)$ in Eq. 3.44 entails multiple contributions, which scale with different powers of the field intensity (see Eq. 3.44), and thus are not easy to elucidate. At short waiting times, the spectra are characterized by a pronounced elongated feature centered at $\omega_1 = \omega_3 = \omega_{01}$, while at longer waiting times, the magnitude of both real and imaginary components decreases, consistently with the vibrational dephasing processes occurring on the picosecond timescale. The absolute value spectra provide an easier visualization of the overall signal intensity and peak localization.

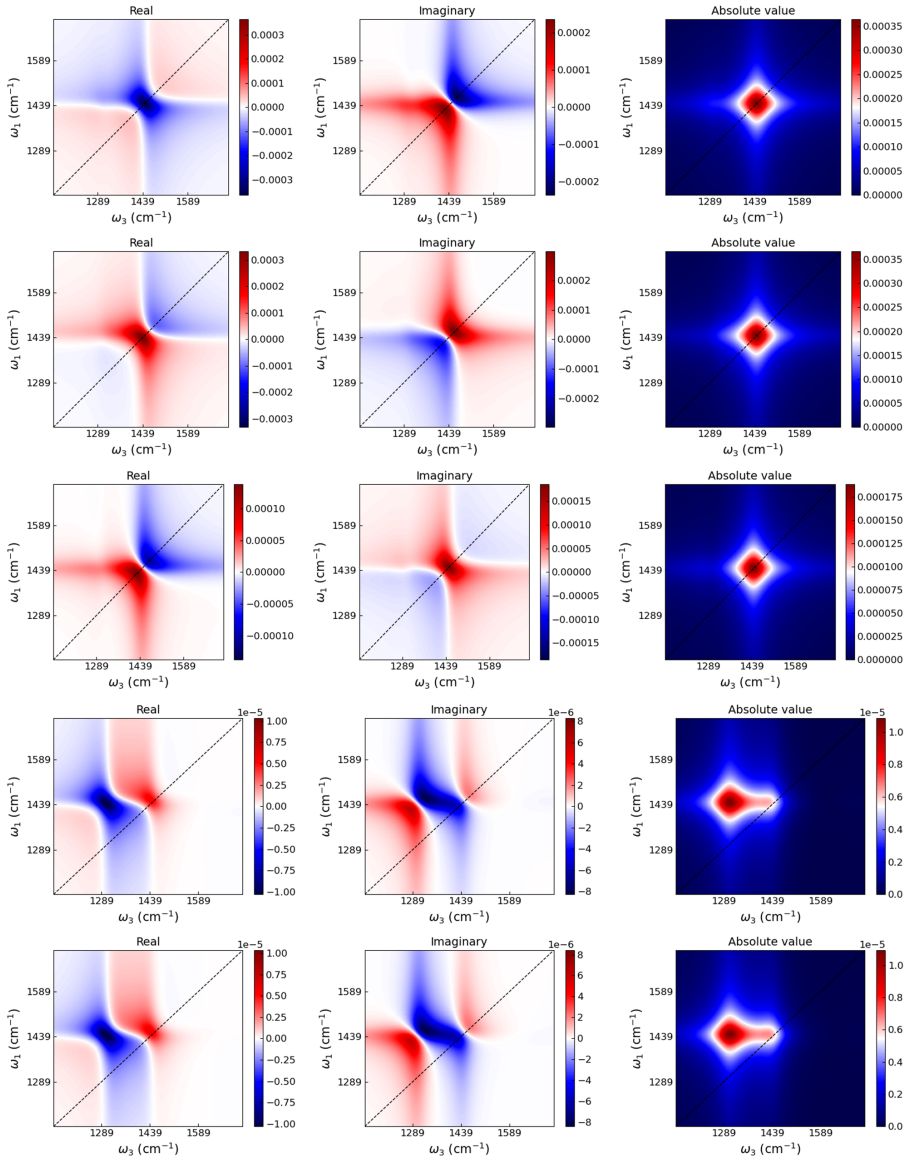

Figure 3.6: The 2D IR signal, $S(\omega_1, \omega_3)$ in Eq. 3.8 obtained as the inverse Fourier transform of the response functions in Fig. 3.4 multiplied by the imaginary unit. From top to bottom: $t_2 = 0.001\,\text{ps}$, $0.01\,\text{ps}$, $0.1\,\text{ps}$, $1\,\text{ps}$, $10\,\text{ps}$. Left panels, central panels and right panels show the real part, the imaginary part and absolute value, respectively.

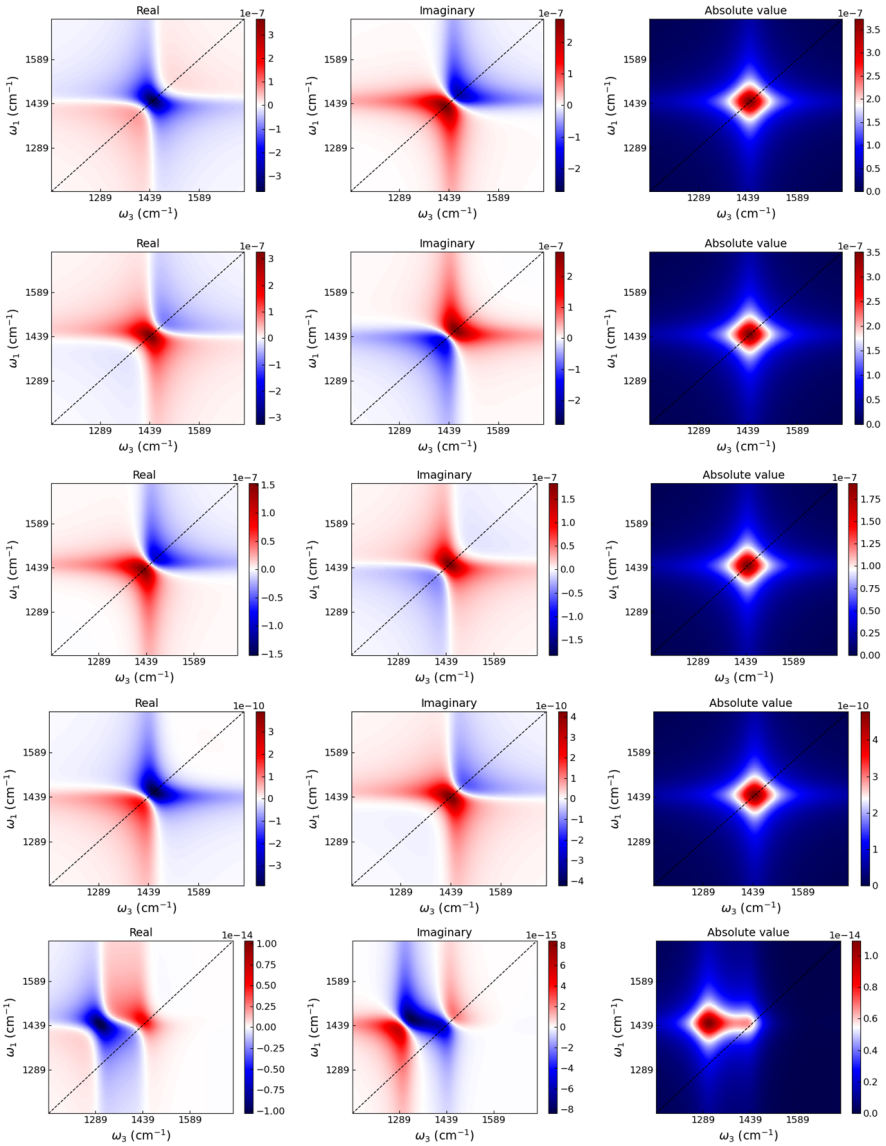

Figure 3.7: The 2D IR signal, $S(\omega_1, \omega_3)$ in Eq. 3.8 obtained as the inverse Fourier transform of the response functions in Figs. 3.5 multiplied by the imaginary unit. From top to bottom: $t_2 = 0.001\,\text{ps}$, $0.01\,\text{ps}$, $0.1\,\text{ps}$, $1\,\text{ps}$, $10\,\text{ps}$. Left panels, central panels and right panels show the real part, the imaginary part and absolute value, respectively.

More informative for our aim is the third order contribution, $q_3(\omega_1, \omega_3)$, the only relevant to 2D IR spectra, reported in Fig. 3.8.

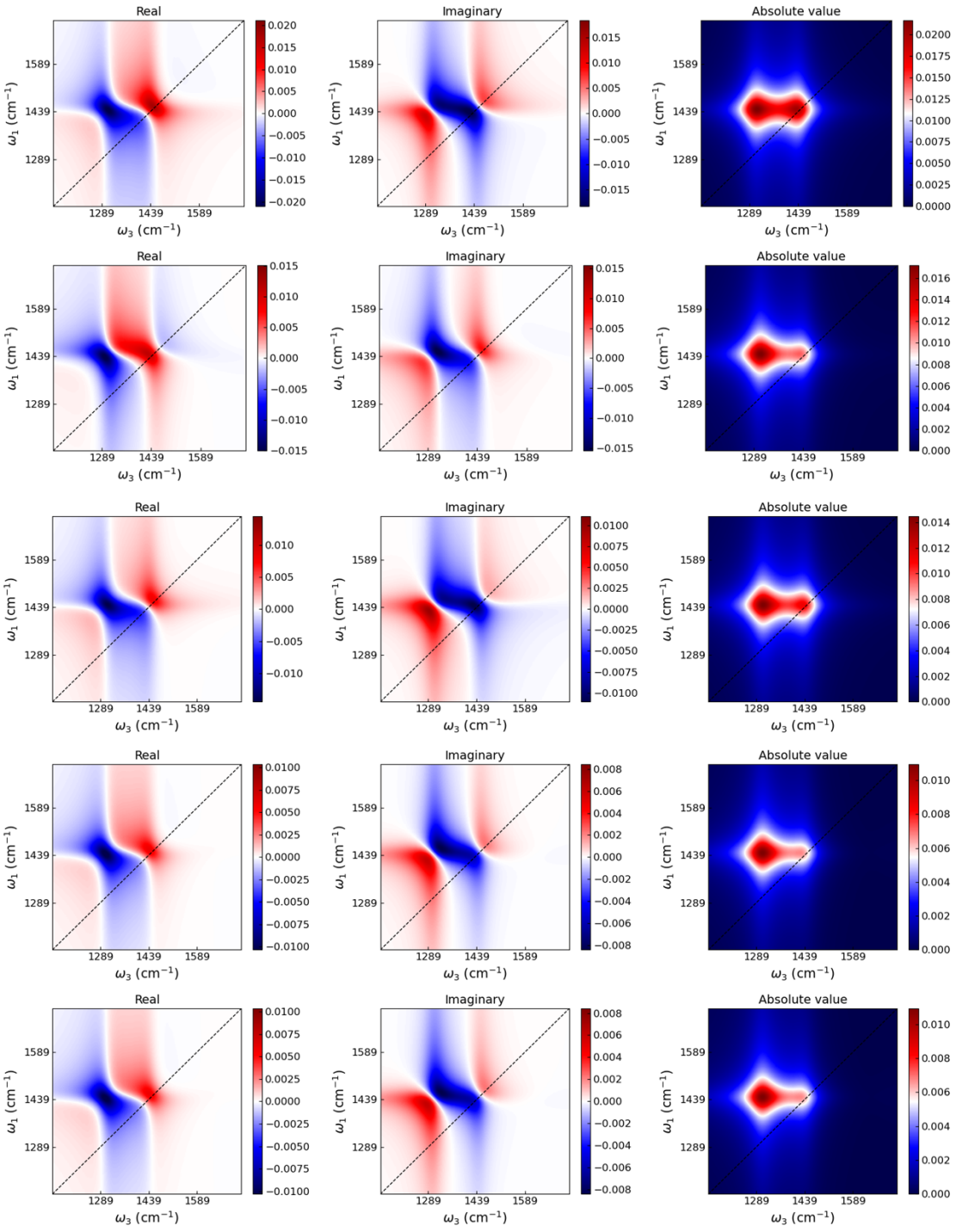

Figure 3.8: Third order contribution ($q_3(\omega_1, \omega_3)$ in Eq. 3.44) of the 2D IR spectra at different waiting times, from top to bottom: $t_2 = 0.001\,\text{ps}$, $0.01\,\text{ps}$, $0.1\,\text{ps}$, $1\,\text{ps}$, $10\,\text{ps}$. Left panels, central panels and right panels show the real part, the imaginary part and absolute value, respectively.

For a direct comparison with experiment, Fig. 3.9 shows the purely absorptive spectra, computed following the method explained in Sec. 3.2.3. The diagonal positive (red) peak centered at $\omega_1 = \omega_3 = \omega_{01}$ corresponds to the fundamental transition of the system, and more specifically it is a bleaching signal due to the decrease in absorbance associated with the de-population of the ground state. The second neg-

ative (blue) peak marks instead the excited state absorption: the population of the first excited state (the fundamental mode) allows for the observation of the $v = 1$ to $v = 2$ transition. This is clearly visible as a consequence of anharmonicity: in a harmonic system, the ground state bleaching and excited state absorption peaks would be exactly superimposed, canceling each other out. The separation between the positive diagonal peak and this negative feature directly reflects the magnitude of the vibrational anharmonicity ($\sim 140\, cm^{-1}$).

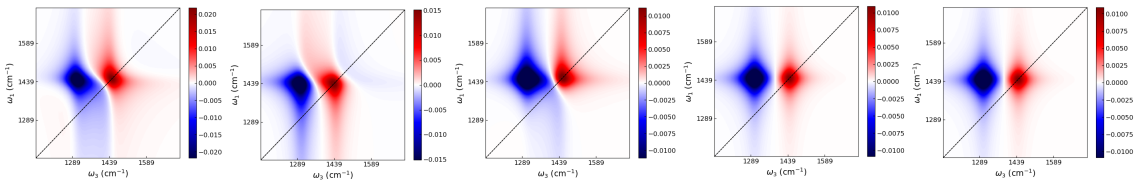

Figure 3.9: 2D IR spectra, purely absorptive component ($S_{abs}(\omega_1, \omega_3)$ in Eq. 3.9) at different waiting times. From left to right: $t_2 = 0.001$ ps, 0.01 ps, 0.1 ps, 1 ps, 10 ps.

3.3.4 The six level system

In the previous section we have seen how the anharmonicity shows up clearly in 2D IR spectra. Other important information can be retrieved from the spectra relating to the coupling between vibrational modes. It is therefore interesting to move from the single mode case, discussed in the previous section, to discuss a system where two vibrational modes are present. Specifically, we adopt model the parameters relevant to phenol blue,[111–113] listed in Tab. 3.2.

Parameter	**Value**	**Units**
$2z$	1.34	eV
$\sqrt{2}t$	0.95	eV
$\hbar\omega_1, \hbar\omega_2$	0.196, 0.209	eV
$\hbar\tilde{\omega}_1, \hbar\tilde{\omega}_2$	0.176, 0.199	eV
δ_1, δ_2	1.24, 1.20	
μ_0	14	D
T_2	350	fs

Table 3.2: Parameters of the model for the double-mode system.

Upon diagonalization, we obtain the system eigenstates and, for our purposes, only the first six eigenstates are of interest, with relative energies (in cm^{-1}) of 0, 1511, 1643, 3019, 3152, and 3285, listed in ascending order. The corresponding dipole moment matrix (in D) is:

$$\boldsymbol{\mu} = \begin{pmatrix} 0 & -0.42 & 0.25 & 0.07 & 0.03 & 0.03 \\ -0.42 & 0.11 & -0.03 & -0.61 & -0.25 & 0 \\ 0.25 & -0.03 & 0.05 & 0.01 & 0.42 & 0.36 \\ 0.07 & -0.61 & 0.01 & 0.22 & 0.05 & 0 \\ 0.03 & -0.25 & 0.42 & 0.05 & 0.16 & 0.05 \\ 0.03 & 0 & 0.36 & 0 & 0.05 & 0.09 \end{pmatrix}$$

We start addressing the linear spectrum. The left panel of Fig. 3.10 shows the dipole moment as a function of time after the initial pulse and the right panel shows the relevant inverse Fourier transform. The two fundamental transitions are clearly seen, the overtones and combination bands are very week and are only seen upon zooming.

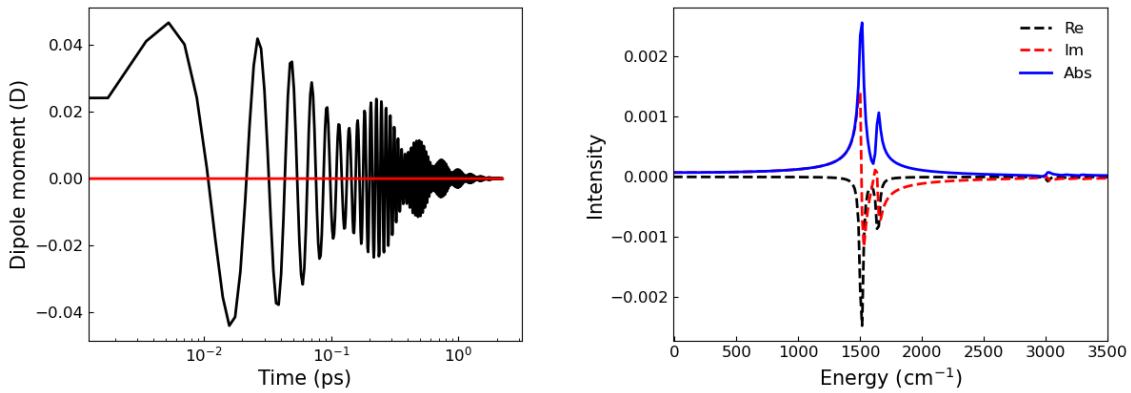

Figure 3.10: Left panel: Dipole moment as a function of time after the interaction with the first field. Right panel: Inverse Fourier transform (arbitrary units) of the dipole moment displayed in the left panel, multiplied by the imaginary unit. The dashed black and red curves denote the real and imaginary components, respectively, while the solid blue curve represents the magnitude. The field intensity was set to $F_0 = 10^{-1} eVD^{-1}$.

To address the 2D IR spectra, we first calculate the response function, reported in Fig. 3.11, for a specific value of the applied field, $F_0 = 10^{-1} eVD^{-1}$. Adopting the standard procedure to extract the third order response out of the total 2D signal, we obtain the data in Fig. 3.12. These data show the appearance of two diagonal peaks, as well as off-diagonal signals.

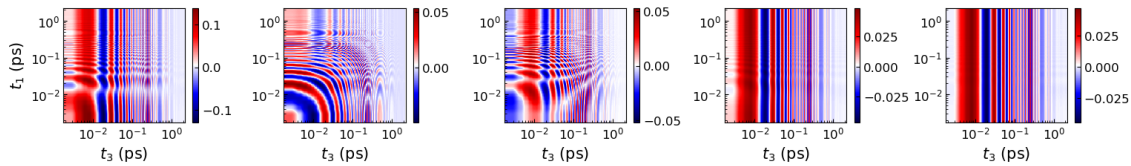

Figure 3.11: Response functions ($R(t_1, t_3)$ in Eq. 3.7) at different waiting times: from left to right, $t_2 = 0.001$ ps, 0.01 ps, 0.1 ps, 1 ps, 10 ps. The field intensity was set to $F_0 = 10^{-1} eVD^{-1}$.

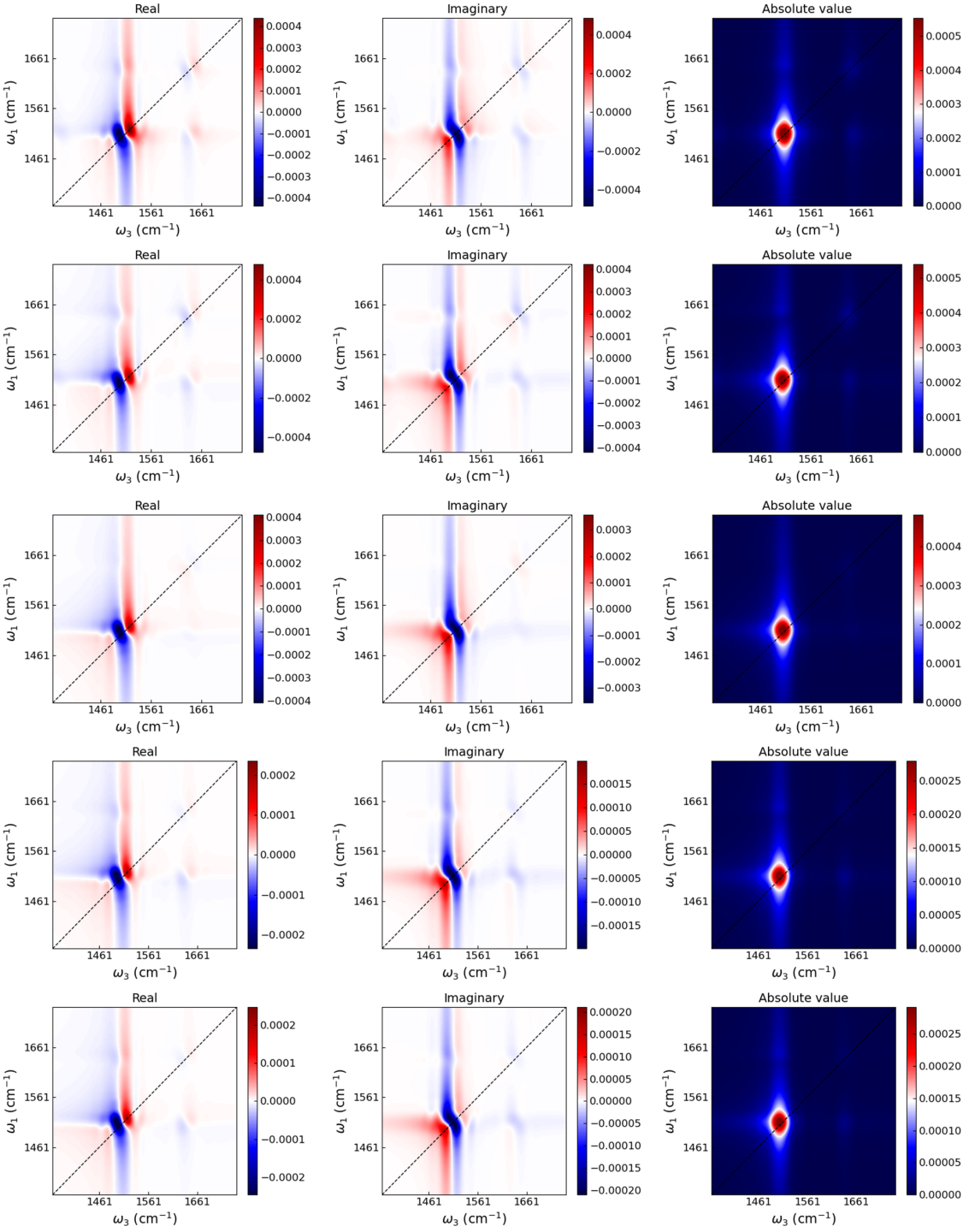

Figure 3.12: Third order contribution ($q_3(\omega_1, \omega_3)$ in Eq. 3.44) of the 2D IR spectra at different waiting times, from top to bottom: $t_2 = 0.001\,\text{ps}$, $0.01\,\text{ps}$, $0.1\,\text{ps}$, $1\,\text{ps}$, $10\,\text{ps}$. Left panels, central panels and right panels show the real part, the imaginary part and absolute value, respectively.

Finally, Fig. 3.13 shows the purely absorptive component of the 2D IR spectra. Along the diagonal we see the ground state bleaching peaks associated with the two fundamental transitions (blue in the figure). Close to these peaks, the excited state absorption peaks (red) appear, clearly demonstrating the anharmonic character of the two vibrations. More interesting are the off diagonal peaks that demonstrate

that the two modes are indeed mutually coupled, a quite impressive result since the two modes are fully decoupled in the model. Specifically, Duschinsky coupling is not explicitly introduced in the model, or, in other terms, it does not enter the diabatic picture. However, it naturally appears in the calculated spectra, as a result of the interaction of the two vibrational modes with the electronic system.

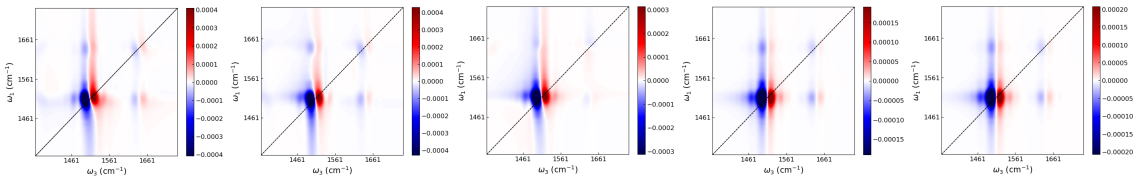

Figure 3.13: Purely absorptive spectra ($S_{abs}(\omega_1, \omega_3)$ in Eq. 3.9) at different waiting times. From left to right: $t_2 = 0.001\,\text{ps}$, $0.01\,\text{ps}$, $0.1\,\text{ps}$, $1\,\text{ps}$, $10\,\text{ps}$.

3.4 Conclusions and future outlook

The approach illustrated by Hamm and Zanni[115] regarding the simulation of the 2D spectra of molecular systems is well-known in the scientific literature. It enables the prediction of the spectra through a perturbative approach, directly providing the third order response function, from which the 2D signals can be efficiently estimated applying the inverse Fourier transform operation. This method, though, does not allow the implementation of a realistic evolution of the density matrix, which is needed to address the solvation dynamics in the proper way, and this is due to the fact that only the perturbative correction of the density matrix is propagated during the simulation of the 2D experiment. Here we proposed a new approach where the full density matrix is maintained and propagated throughout the simulation. Expanding the density matrix up to the first perturbative order, we are able to extract the correct third order response (and so the correct spectra) combining the results of the simulations performed at different values of the field intensity.

At the moment of writing this thesis, this work was not completed. Indeed, we realized that, in order to have a well-behaved density matrix as needed to properly implement open quantum system approaches to the matrix dynamics, the effect of each pulse should enter up to the second order. Unfortunately, in these conditions, spurious (pump-probe) terms appear in the third order response that are not easy to disentagle. While we are working to solve this issue, the results are too preliminary to be inserted here.

Appendix B

Derivation of the response function for a two-level system at the second perturbative order

The second order correction to the density matrix is given by:

$$\begin{aligned}
\boldsymbol{\rho}^{(2)} &= \left(\frac{1}{i\hbar}\right)\int_{-\infty}^{t}[-\boldsymbol{\mu}F_0\delta(t'-t_0),\boldsymbol{\rho}^{(1)}(t')]dt' \\
&= -iA^2/i\left[\begin{pmatrix}0 & 1\\ 1 & 0\end{pmatrix},\begin{pmatrix}c-b & d-a\\ a-d & b-c\end{pmatrix}\right] \\
&= -A^2\left[\begin{pmatrix}a-d & b-c\\ c-b & d-a\end{pmatrix}-\begin{pmatrix}d-a & c-b\\ b-c & a-d\end{pmatrix}\right] \\
&= 2A^2\begin{pmatrix}d-a & c-b\\ b-c & a-d\end{pmatrix}
\end{aligned} \tag{B.1}$$

so that the second order corrected density matrix can be written as:

$$\begin{aligned}
\boldsymbol{\rho} &= \begin{pmatrix}a & b\\ c & d\end{pmatrix}+iA\begin{pmatrix}c-b & d-a\\ a-d & b-c\end{pmatrix}+2A^2\begin{pmatrix}d-a & c-b\\ b-c & a-d\end{pmatrix} \\
&= \begin{pmatrix}a+iA(c-b)+2A^2(d-a) & b+iA(d-a)+2A^2(c-b)\\ c+iA(a-d)+2A^2(b-c) & d+iA(b-c)+2A^2(a-d)\end{pmatrix}
\end{aligned} \tag{B.2}$$

In the simplest case of a system prepared with the whole population in the ground state, $a=1$ and $b=c=d=0$, and Eq. B.1 becomes:

$$\boldsymbol{\rho} = \begin{pmatrix}1-2A^2 & -iA\\ iA & 2A^2\end{pmatrix} \tag{B.3}$$

Coherences evolve in time according to Eq. 3.18, and the elements of the density matrix become:

$$\boldsymbol{\rho}(t_1) = \begin{pmatrix}1-2A^2 & -iAe^{i\omega t_1-t_1/T_2}\\ iAe^{-i\omega t_1-t_1/T_2} & 2A^2\end{pmatrix} \equiv \begin{pmatrix}a' & b'\\ c' & d'\end{pmatrix} \tag{B.4}$$

The second pulse is shine on the sample, and we get:

$$\begin{aligned}
\rho_{00}(t_1) &\equiv a'' \\
&= a' + iA(c' - b') + 2A^2(d' - a') \\
&= 1 - 2A^2 + iA\big(iAe^{-i\omega t_1 - t_1/T_2} + iAe^{i\omega t_1 - t_1/T_2}\big) \\
&\quad + 2A^2(2A^2 - 1 + 2A^2) \\
&= 1 - 2A^2 - A^2\big(e^{-i\omega t_1 - t_1/T_2} + e^{i\omega t_1 - t_1/T_2}\big) + 8A^4 - 2A^2 \\
&= 8A^4 - A^2\Big[4 + e^{-i\omega t_1 - t_1/T_2} + e^{i\omega t_1 - t_1/T_2}\Big] + 1 \\
&= 8A^4 - A^2[4 + 2e^{-t_1/T_2}\cos(\omega t_1)]
\end{aligned} \tag{B.5}$$

$$\begin{aligned}
\rho_{01}(t_1) &\equiv b'' \\
&= b' + iA(d' - a') + 2A^2(c' - b') \\
&= -iAe^{i\omega t_1 - t_1/T_2} + iA(2A^2 - 1 + 2A^2) \\
&\quad + 2A^2\big(iAe^{-i\omega t_1 - t_1/T_2} + iAe^{i\omega t_1 - t_1/T_2}\big) \\
&= -iA\big(1 + e^{i\omega t_1 - t_1/T_2}\big) + 2iA^3\Big(2 + e^{-i\omega t_1 - t_1/T_2} + e^{i\omega t_1 - t_1/T_2}\Big) \\
&= 4iA^3[1 + e^{-t_1/T_2}\cos(\omega t_1)] - iA(1 + e^{i\omega t_1 - t_1/T_2})
\end{aligned} \tag{B.6}$$

$$\rho_{10}(t_1) = \rho_{01}^{\dagger}(t_1) \tag{B.7}$$

$$\rho_{11}(t_1) = 1 - \rho_{00}(t_1) \tag{B.8}$$

The system evolves during t_2 and the density matrix becomes:

$$\boldsymbol{\rho}(t_1, t_2) = \begin{pmatrix} a'' & b''e^{i\omega t_2 - t_2/T_2} \\ (b''e^{i\omega t_2 - t_2/T_2})^{\dagger} & 1 - a'' \end{pmatrix} \tag{B.9}$$

Lastly, the third pulse is then shine on the system, and the elements of the density matrix become:

$$\begin{aligned}
\rho_{00}(t_1, t_2) &= a'' + iA\left[(b''e^{i\omega t_2 - t_2/T_2})^{\dagger} - b''e^{i\omega t_2 - t_2/T_2}\right] + 2A^2(1 - a'' - a'') \\
&= a'' + iA\left[-2\,\mathrm{Im}(b''e^{i\omega t_2 - t_2/T_2})\right] + 2A^2(1 - 2a'')
\end{aligned} \tag{B.10}$$

$$\begin{aligned}
\rho_{01}(t_1, t_2) &= b''e^{i\omega t_2 - t_2/T_2} + iA(1 - 2a'') + 2A^2(-2\,\mathrm{Im}(b''e^{i\omega t_2 - t_2/T_2})) \\
&= b''e^{i\omega t_2 - t_2/T_2} + iA(1 - 2a'') - 4A^2\,\mathrm{Im}(b''e^{i\omega t_2 - t_2/T_2})
\end{aligned} \tag{B.11}$$

$$\rho_{10}(t_1, t_2) = \rho_{01}^{\dagger}(t_1, t_2) \tag{B.12}$$

$$\rho_{11}(t_1, t_2) = 1 - \rho_{00}(t_1, t_2) \tag{B.13}$$

The evolution of the coherences along t_3 gives:

$$\begin{aligned}\rho_{01}(t_1,t_2,t_3) &= e^{i\omega t_3 - t_3/T_2}[b'' e^{i\omega t_2 - t_2/T_2}] + \\ &+ e^{i\omega t_3 - t_3/T_2}[iA(1-2a'') - 4A^2\,\mathrm{Im}(b'' e^{i\omega t_2 - t_2/T_2})] \end{aligned} \tag{B.14}$$

$$\rho_{10}(t_1,t_2,t_3) = \rho_{01}^{(111)\dagger}(t_1,t_2,t_3) \tag{B.15}$$

and the response function can be obtained as:

$$\begin{aligned} R(t_1,t_2,t_3) &= \mathrm{Tr}\left[\boldsymbol{\mu}\boldsymbol{\rho}(t_1,t_2,t_3)\right] \\ &= \mu_{10}\left[\rho_{01}(t_1,t_2,t_3) + c.c.\right] \\ &= 2\mu_{10}\,\mathrm{Re}\{\rho_{01}(t_1,t_2,t_3)\} \end{aligned} \tag{B.16}$$

Re-arranging the terms of $\rho_{01}(t_1,t_2,t_3)$, we get:

$$\begin{aligned} \frac{\rho_{01}(t_1,t_2,t_3)}{e^{i\omega t_3 - t_3/T_2}} &= [b'' e^{i\omega t_2 - t_2/T_2} + iA(1-2a'') - 4A^2\,\mathrm{Im}(b'' e^{i\omega t_2 - t_2/T_2})] \\ &= [\mathrm{Re}\big\{b'' e^{i\omega t_2 - t_2/T_2}\big\}] + \\ &\quad + [(i-4A^2)\,\mathrm{Im}\big\{b'' e^{i\omega t_2 - t_2/T_2}\big\} + iA(1-2a'')] \end{aligned} \tag{B.17}$$

and simplifying each term of Eq. B.17, we write:

$$\begin{aligned} \mathrm{Re}\big\{b'' e^{i\omega t_2 - t_2/T_2}\big\} &= \mathrm{Re}\big\{e^{i\omega t_2 - t_2/T_2}[4iA^3[1+e^{-t_1/T_2}\cos(\omega t_1)] - iA(1+e^{i\omega t_1 - t_1/T_2})]\big\} \\ &= e^{-t_2/T_2}\,\mathrm{Im}\big\{-e^{i\omega t_2} 4A^3(1+e^{-t_1/T_2}\cos(\omega t_1))\big\} + \\ &\quad + e^{-t_2/T_2}\,\mathrm{Im}\big\{Ae^{i\omega t_2}(1+e^{i\omega t_1 - t_1/T_2})\big\} \\ &= -4A^3 e^{-t_2/T_2}\sin(\omega t_2)(1+e^{-t_1/T_2}\cos(\omega t_1)) + \\ &\quad + Ae^{-t_2/T_2}\,\mathrm{Im}\big\{e^{i\omega t_2}(1+e^{i\omega t_1 - t_1/T_2})\big\} \\ &= -4A^3 e^{-t_2/T_2}\sin(\omega t_2)(1+e^{-t_1/T_2}\cos(\omega t_1)) + \\ &\quad + Ae^{-t_2/T_2}[\sin(\omega t_2) + \sin(\omega(t_2+t_1))e^{-t_1/T_2}] \end{aligned} \tag{B.18}$$

$$\begin{aligned} \mathrm{Im}\big\{b'' e^{i\omega t_2 - t_2/T_2}\big\} &= \mathrm{Im}\big\{e^{i\omega t_2 - t_2/T_2}[4iA^3[1+e^{-t_1/T_2}\cos(\omega t_1)] - iA(1+e^{i\omega t_1 - t_1/T_2})]\big\} \\ &= e^{-t_2/T_2}\,\mathrm{Re}\big\{e^{i\omega t_2} 4A^3(1+e^{-t_1/T_2}\cos(\omega t_1))\big\} + \\ &\quad - e^{-t_2/T_2}\,\mathrm{Re}\big\{Ae^{i\omega t_2}(1+e^{i\omega t_1 - t_1/T_2})\big\} \\ &= 4A^3 e^{-t_2/T_2}\cos(\omega t_2)(1+e^{-t_1/T_2}\cos(\omega t_1)) + \\ &\quad - Ae^{-t_2/T_2}\,\mathrm{Re}\big\{e^{i\omega t_2}(1+e^{i\omega t_1 - t_1/T_2})\big\} \\ &= 4A^3 e^{-t_2/T_2}\cos(\omega t_2)(1+e^{-t_1/T_2}\cos(\omega t_1)) + \\ &\quad - Ae^{-t_2/T_2}[\cos(\omega t_2) + \cos(\omega(t_2+t_1))e^{-t_1/T_2}] \end{aligned} \tag{B.19}$$

$$\begin{aligned} iA(1-2a'') &= iA(1-16A^4+2A^2[4+2e^{-t_1/T_2}\cos(\omega t_1)]) \\ &= -16iA^5 + 2iA^3[4+2e^{-t_1/T_2}\cos(\omega t_1)] + iA \end{aligned} \tag{B.20}$$

Regrouping the terms with same power of A and assuming the special case of $t_2 = 0$, we get:

$$\begin{aligned}
\frac{\rho_{01}^{(111)}(t_1, t_2 = 0, t_3)}{e^{i\omega t_3 - t_3/T_2}} &= A\sin(\omega t_1)e^{-t_1/T_2} + 4A^3(i - 4A^2)(1 + e^{-t_1/T_2}\cos(\omega t_1)) + \\
&\quad - (i - 4A^2)A[1 + \cos(\omega t_1)e^{-t_1/T_2}] - 16iA^5 + \\
&\quad + 2iA^3[4 + 2e^{-t_1/T_2}\cos(\omega t_1)] + iA \\
&= -16A^5(i + 1 + e^{-t_1/T_2}\cos(\omega t_1)) + \\
&\quad + 4A^3[(3i + 1) + (2i + 1)e^{-t_1/T_2}\cos(\omega t_1)] + \\
&\quad + A[\sin(\omega t_1)e^{-t_1/T_2} - i(1 + e^{-t_1/T_2}\cos(\omega t_1)) + i] \\
&= -16A^5(i + 1 + e^{-t_1/T_2}\cos(\omega t_1)) + \\
&\quad + 4A^3[(3i + 1) + (2i + 1)e^{-t_1/T_2}\cos(\omega t_1)] + \\
&\quad + Ae^{-t_1/T_2}[\sin(\omega t_1) - i\cos(\omega t_1)]
\end{aligned} \tag{B.21}$$

In the weak field limit ($A \ll 0$), Eq. B.21 becomes:

$$\rho_{01}^{(111)}(t_1, t_3, A \ll 0) \approx -iAe^{i\omega t_3 - t_3/T_2}e^{\omega t_1 - t_1/T_2} \tag{B.22}$$

and the response function in Eq. 3.28 becomes:

$$\begin{aligned}
R(t_1, t_2 = 0, t_3, A \ll 0) &\approx 2\mu_{10}\,\mathrm{Re}\Big\{\rho_{01}^{(111)}(t_1, t_2 = 0, t_3)\Big\} \\
&\approx 2\mu_{10}A\,\mathrm{Im}[e^{i\omega t_3 - t_3/T_2}e^{\omega t_1 - t_1/T_2}] \\
&\approx 4\mu_{10}A\sin[\omega(t_1 + t_3)]e^{-(t_1+t_3)/T_2}
\end{aligned} \tag{B.23}$$

which is the expression for a damped sinusoidal function.

Once the inverse 2D Fourier transform is applied to Eq. B.23, we get a Lorentzian diagonal peak at the characteristic frequency of the system ($\omega = \omega_1 = \omega_2$), the intensity of which is increasing linearly with A under the assumptions outlined above.

In the limit of $t_2 \to +\infty$, instead, looking at Eq. B.17, it is easy to prove that the term $iA(1 - 2a'')$ is the only one surviving the summation. Thus, we recover the response function of a one-dimensional experiment

$$\begin{aligned}
R(t_1, t_2 \to +\infty, t_3, A \ll 0) &\approx 2\mu_{10}\,\mathrm{Re}\Big\{\rho_{01}^{(111)}(t_1, t_2 \to +\infty, t_3, A \ll 0)\Big\} \\
&= 2\mu_{10}\,\mathrm{Re}\big\{iAe^{i\omega t_3 - t_3/T_2}\big\} \\
&= -2\mu_{10}A\sin(\omega t_3)e^{-t_3/T_2}
\end{aligned} \tag{B.24}$$

since the information of the first two pulses is completely lost due to the dephasing of the coherences.

Conclusions

Understanding the dynamics and relaxation of excited states is a central theoretical issue with important implications in molecular spectroscopy and of enormous interest for the optimization of optoelectronic devices. In this thesis we have addressed the problem following different strategies. In the first chapter, we made extensive use of computational approaches to address the photophysics of thermally activated delayed fluorescence (TADF), a phenomenon at the heart of the third OLED generation. In a tight collaboration with experimentalists, we investigated how the molecular conformation and the conformational degrees of freedom affect in a highly non-trivial way the delicate photophysics of TADF in donor-acceptor dyes. Environmental effects are dealt with an in-house protocol, that, at variance with conventional approaches implemented in quantum chemical packages, properly accounts for the electronic solvent polarizability. The most important lesson in this respect is that apparently minor modifications of the system, in terms of chemical substitutions on the donor or acceptor sites and/or changes on the structure of the bridge, can indeed alter the photophysics of the system in a highly non-trivial way, affecting the ground and/or the excited state geometry, sometimes even introducing novel relaxation pathways. The second chapter faces the more fundamental issue of the estimate of non-radiative rates. In recent years, several computational packages have been released and have gained considerable popularity, devoted to the *ab initio* estimate of non-radiative rates. Strictly speaking, this is not possible: non-radiative rates require the interaction of the quantum mechanical system with the environment and since it is not possible to deal with the environment in any *ab initio* approach, the estimate of non-radiative rates must necessarily introduce some phenomenological parameter. In our work, we uncovered this parameter hidden into the apodization of the generating function. We discussed the relevant physics, also comparing the results with those obtained with standard open quantum system approaches. While introducing phenomenological parameters is in any case needed for the estimate of non-radiative rates, understanding their fundamental role and their physical origin is important in order to make educated guesses for their definition and even more to get a realistic assessment of the quality and reliability of estimated rates. Finally, in the last chapter, we presented preliminary results addressing the 2D IR spectra of phenol blue, a commercial dye with a well characterized vibrational solvatochromism. The goal here is the simulation of 2D IR spectra of the dye in solution to address the entangle dynamics of the dye and the solvent. In this respect, we plan to exploit an approach, recently developed in the host laboratory, that combines the Redfield approach for the dye relaxation with a Smoluchowski description of the solvent dynamics. The problem we faced in this respect is that

the standard approach to 2D IR spectra only deals with perturbative corrections to the density matrix and not with the whole *well-behaved* density matrix. But the Redfiled-Smoluchowski approach can only work on the whole density matrix and therefore we propose an alternative approach to the 2D IR spectra, where the third-order response is extracted from the propagation of the whole density matrix. The results are preliminary, and this work will be pursued in the months following the completion of the PhD.

Acknowledgments

Funding for all studies conducted during the PhD was provided by the PNRR MUR projects ECS-00000033-ECOSISTER and PE0000023-NQSTI. We acknowledge the support from the local HPC (High Performance Computing) facility and from the equipment and framework of the COMP-HUB and COMP-R Initiatives, funded by the "Departments of Excellence program of the Italian Ministry for University and Research" (MIUR, 2018-2022 and MUR, 2023–2027).

Bibliography

[1] G. Hong, X. Gan, C. Leonhardt, Z. Zhang, J. Seibert, J. M. Busch, and S. Bräse. A brief history of oleds—emitter development and industry milestones. *Advanced Materials*, 33:2005630, 2021. doi:10.1002/adma.202005630.

[2] A. Köhler and H. Bässler. Triplet states in organic semiconductors. *Materials Science and Engineering: R Reports*, 66:71, 2009. doi:10.1016/j.mser.2009.09.001.

[3] J. Marques Do Santos et al. The golden age of thermally activated delayed fluorescence materials: Design and exploitation. *Chemical Reviews*, 124(24): 13736–14110, 2024. doi:10.1021/acs.chemrev.3c00755.

[4] M. A. Baldo, D. F. O'Brien, Y. You, A. Shoustikov, S. Sibley, M. E. Thompson, and S. R. Forrest. Highly efficient phosphorescent emission from organic electroluminescent devices. *Nature*, 395(6698):151–154, 1998. ISSN 1476-4687. doi:10.1038/25954.

[5] S. Reineke and M. A. Baldo. Recent progress in the understanding of exciton dynamics within phosphorescent oleds. *Physica Status Solidi A*, 209:2341–2353, 2012. doi:10.1002/pssa.201228292.

[6] H. Uoyama, K. Goushi, K. Shizu, and C. Adachi. Highly efficient organic light-emitting diodes from delayed fluorescence. *Nature*, 492:234–238, 2012. doi:10.1038/nature11687.

[7] Ayataka Endo, Keigo Sato, Kazuaki Yoshimura, Takahiro Kai, Atsushi Kawada, Hiroshi Miyazaki, and Chihaya Adachi. Efficient up-conversion of triplet excitons into a singlet state and its application for organic light emitting diodes. *Applied Physics Letters*, 98(8):083302, 2011. doi:10.1063/1.3558906. URL `https://doi.org/10.1063/1.3558906`.

[8] Hajime Uoyama, Kenichi Goushi, Katsuyuki Shizu, Hiroki Nomura, and Chihaya Adachi. Highly efficient organic light-emitting diodes from delayed fluorescence. *Nature*, 492:234–238, 2012. doi:10.1038/nature11687. URL `https://doi.org/10.1038/nature11687`.

[9] T. J. Penfold, F. B. Dias, and A. P. Monkman. The theory of thermally activated delayed fluorescence for organic light emitting diodes. *Chemical Communications*, 54(32):3926–3935, 2018. ISSN 1364-548X. doi:10.1039/c7cc09612g.

[10] Yoann Olivier, Mónica Moral, Luca Muccioli, and Juan-Carlos Sancho-García. Dynamic nature of excited states of donor–acceptor TADF materials for OLEDs: how theory can reveal structure–property relationships. *Journal of Materials Chemistry C*, 5(23):5718–5729, 2017. ISSN 2050-7534. doi:10.1039/c6tc05075a.

[11] Y. Olivier, J.-C. Sancho-Garcia, L. Muccioli, G. D'Avino, and D. Beljonne. Computational design of thermally activated delayed fluorescence materials: The challenges ahead. *The Journal of Physical Chemistry Letters*, 9(20):6149–6163, 2018. ISSN 1948-7185. doi:10.1021/acs.jpclett.8b02327. URL `https://doi.org/10.1021/acs.jpclett.8b02327`.

[12] Francesco Di Maiolo, D. K. Andrea Phan Huu, Davide Giavazzi, Andrea Landi, Ottavia Racchi, and Anna Painelli. Shedding light on thermally-activated delayed fluorescence. *Chemical Science*, 15(15):5434–5450, 2024. ISSN 2041-6539. doi:10.1039/d4sc00033a.

[13] John Marques Dos Santos, David Hall, Biju Basumatary, Megan Bryden, Dongyang Chen, Praveen Choudhary, Thomas Comerford, Ettore Crovini, Andrew Danos, Joydip De, Stefan Diesing, Mahni Fatahi, Máire Griffin, Abhishek Kumar Gupta, Hassan Hafeez, Lea Hämmerling, Emily Hanover, Janine Haug, Tabea Heil, Durai Karthik, Shiv Kumar, Oliver Lee, Haoyang Li, Fabien Lucas, Campbell Frank Ross Mackenzie, Aminata Mariko, Tomas Matulaitis, Francis Millward, Yoann Olivier, Quan Qi, Ifor D. W. Samuel, Nidhi Sharma, Changfeng Si, Leander Spierling, Pagidi Sudhakar, Dianming Sun, Eglė Tankelevičiūtė, Michele Duarte Tonet, Jingxiang Wang, Tao Wang, Sen Wu, Yan Xu, Le Zhang, and Eli Zysman-Colman. The golden age of thermally activated delayed fluorescence materials: Design and exploitation. *Chemical Reviews*, 124(24):13736–14110, 2024-12. ISSN 1520-6890. doi:10.1021/acs.chemrev.3c00755.

[14] Begoña Milián-Medina and Johannes Gierschner. Computational design of low singlet–triplet gap all-organic molecules for oled application. *Organic Electronics*, 13(6):985–991, 2012. ISSN 1566-1199. doi:10.1016/j.orgel.2012.02.010.

[15] Wei-Lung Tsai, Ming-Hao Huang, Wei-Kai Lee, Yi-Jiun Hsu, Kuan-Chung Pan, Yi-Hsiang Huang, Hao-Chun Ting, Monima Sarma, Yu-Yi Ho, Hung-Chieh Hu, Chung-Chia Chen, Meng-Ting Lee, Ken-Tsung Wong, and Chung-Chih Wu. A versatile thermally activated delayed fluorescence emitter for both highly efficient doped and non-doped organic light emitting devices. *Chemical Communications*, 51(71):13662–13665, 2015. ISSN 1364-548X. doi:10.1039/C5CC05022G. URL `http://dx.doi.org/10.1039/C5CC05022G`.

[16] Wei Li, Binbin Li, Xinyi Cai, Lin Gan, Zhida Xu, Wenqi Li, Kunkun Liu, Dongcheng Chen, and Shi-Jian Su. Tri-spiral donor for high efficiency and versatile blue thermally activated delayed fluorescence materials. *Angewandte Chemie International Edition*, 58(33):11301–11305, 2019. ISSN 1521-3773. doi:10.1002/anie.201904272.

[17] Yoshimasa Wada, Shosei Kubo, and Hironori Kaji. Adamantyl substitution strategy for realizing solution-processable thermally stable deep-blue thermally activated delayed fluorescence materials. *Advanced Materials*, 30(8), 2018. ISSN 1521-4095. doi:10.1002/adma.201705641.

[18] Y. Wada, H. Nakagawa, S. Matsumoto, et al. Organic light emitters exhibiting very fast reverse intersystem crossing. *Nature Photonics*, 14:643–649, 2020. doi:10.1038/s41566-020-0667-0. URL `https://doi.org/10.1038/s41566-020-0667-0`.

[19] Eduard Spuling, Nidhi Sharma, Ifor D. W. Samuel, Eli Zysman-Colman, and Stefan Bräse. (deep) blue through-space conjugated tadf emitters based on [2.2]paracyclophanes. *Chemical Communications*, 54(67):9278–9281, 2018. ISSN 1364-548X. doi:10.1039/c8cc04594a.

[20] Shiv Kumar, Larissa Gomes Franca, Kleitos Stavrou, Ettore Crovini, David B. Cordes, Alexandra M. Z. Slawin, Andrew P. Monkman, and Eli Zysman-Colman. Investigation of intramolecular through-space charge-transfer states in donor–acceptor charge-transfer systems. *The Journal of Physical Chemistry Letters*, 12(11):2820–2830, 2021. ISSN 1948-7185. doi:10.1021/acs.jpclett.1c00265.

[21] Kummara Madhusudana Rao, Rajavaram Ramaraghavulu, Deepti Kolli, S. Harinath Babu, S. V. Prabhakar Vattikuti, and Mallesham Godumala. Recent breakthroughs in through-space charge transfer in π-stacked molecules as thermally activated delayed fluorescent emitters for oled applications. *Journal of Materials Chemistry C*, 13(7):3091–3122, 2025. ISSN 2050-7534. doi:10.1039/d4tc05181e.

[22] Susumu Oda, Bungo Kawakami, Ryosuke Kawasumi, Ryota Okita, and Takuji Hatakeyama. Multiple resonance effect-induced sky-blue thermally activated delayed fluorescence with a narrow emission band. *Organic Letters*, 21(23): 9311–9314, 2019. ISSN 1523-7052. doi:10.1021/acs.orglett.9b03342.

[23] Subeesh Madayanad Suresh, David Hall, David Beljonne, Yoann Olivier, and Eli Zysman-Colman. Multiresonant thermally activated delayed fluorescence emitters based on heteroatom-doped nanographenes: Recent advances and prospects for organic light-emitting diodes. *Advanced Functional Materials*, 30(33), 2020. ISSN 1616-3028. doi:10.1002/adfm.201908677.

[24] Guoyun Meng, Lijie Liu, Zhechang He, David Hall, Xiang Wang, Tai Peng, Xiaodong Yin, Pangkuan Chen, David Beljonne, Yoann Olivier, Eli Zysman-Colman, Nan Wang, and Suning Wang. Multi-resonant thermally activated delayed fluorescence emitters based on tetracoordinate boron-containing pahs: colour tuning based on the nature of chelates. *Chemical Science*, 13(6):1665–1674, 2022. ISSN 2041-6539. doi:10.1039/d1sc05692a.

[25] Jingxiang Wang, Yuka Yasuda, Yongxia Ren, Ryo Kondo, David B. Cordes, Hironori Kaji, and Eli Zysman-Colman. A multi-resonant thermally activated delayed fluorescence emitter with a twisted second-generation carbazole

dendron showing suppressed concentration quenching and its use in solution-processed organic light-emitting diodes. *Organic Chemistry Frontiers*, 12(10): 3279–3287, 2025. ISSN 2052-4129. doi:10.1039/d5qo00146c.

[26] Hajime Nakanotani, Takahiro Higuchi, Taro Furukawa, Kensuke Masui, Kei Morimoto, Masaki Numata, Hiroyuki Tanaka, Yuta Sagara, Takuma Yasuda, and Chihaya Adachi. High-efficiency organic light-emitting diodes with fluorescent emitters. *Nature Communications*, 5(1), 2014. ISSN 2041-1723. doi:10.1038/ncomms5016.

[27] Upasana Deori, Gyana Prakash Nanda, Caroline Murawski, and Pachaiyappan Rajamalli. A perspective on next-generation hyperfluorescent organic light-emitting diodes. *Chemical Science*, 15(43):17739–17759, 2024. ISSN 2041-6539. doi:10.1039/d4sc05489j.

[28] Aarti Aarti, Binesh Puthen Veettil, Alison Rodger, and Koushik Venkatesan. Recent progress and challenges in molecular design for hyperfluorescent based organic light emitting diodes (oleds). *Advanced Optical Materials*, 2025. ISSN 2195-1071. doi:10.1002/adom.202501648.

[29] Z. Yang, Z. Mao, Z. Xie, Y. Zhang, S. Liu, J. Zhao, J. Xu, Z. Chi, and M. P. Aldred. Recent advances in organic thermally activated delayed fluorescence materials. *Chemical Society Reviews*, 46:915, 2017. doi:10.1039/c6cs00368k.

[30] E. Zysman-Colman. Molecular designs offer fast exciton conversion. *Nature Photonics*, 14:593–594, 2020. doi:10.1038/s41566-020-0696-8.

[31] M. A. El-Sayed. Spin–orbit coupling and the radiationless processes in nitrogen heterocycles. *The Journal of Chemical Physics*, 38(12):2834–2838, 1963. doi:10.1063/1.1733610. URL `https://doi.org/10.1063/1.1733610`.

[32] Fernando B. Dias, Jose Santos, David R. Graves, Przemyslaw Data, Roberto S. Nobuyasu, Mark A. Fox, Andrei S. Batsanov, Tiago Palmeira, Mário N. Berberan-Santos, Martin R. Bryce, and Andrew P. Monkman. The role of local triplet excited states and d-a relative orientation in thermally activated delayed fluorescence: Photophysics and devices. *Advanced Science*, 3(12):1600080, 2016. ISSN 2198-3844. doi:10.1002/advs.201600080. URL `https://onlinelibrary.wiley.com/doi/abs/10.1002/advs.201600080`.

[33] Marc K. Etherington, Jamie Gibson, Heather F. Higginbotham, Thomas J. Penfold, and Andrew P. Monkman. Revealing the spin–vibronic coupling mechanism of thermally activated delayed fluorescence. *Nature Communications*, 7:13680, 2016. doi:10.1038/ncomms13680. URL `https://doi.org/10.1038/ncomms13680`.

[34] Igor Lyskov and Christel M. Marian. Climbing up the ladder: Intermediate triplet states promote the reverse intersystem crossing in the efficient TADF emitter ACRSA. *The Journal of Physical Chemistry C*, 121(39):21145–21153, sep 2017. doi:10.1021/acs.jpcc.7b06187.

[35] Jingyao Chen, Xiaoxiao Xiao, Shuai Li, Yuai Duan, Guo Wang, Yi Liao, Qian Peng, Hongbing Fu, Hua Geng, and Zhigang Shuai. A novel strategy toward thermally activated delayed fluorescence from a locally excited state. *The Journal of Physical Chemistry Letters*, 13(11):2653–2660, 2022. ISSN 1948-7185. doi:10.1021/acs.jpclett.2c00224.

[36] Xian-Kai Chen, Shou-Feng Zhang, Jian-Xun Fan, and Ai-Min Ren. Nature of highly efficient thermally activated delayed fluorescence in organic light-emitting diode emitters: Nonadiabatic effect between excited states. *The Journal of Physical Chemistry C*, 119(18):9728–9733, apr 2015. doi:10.1021/acs.jpcc.5b00276.

[37] Jamie Gibson, Andrew P. Monkman, and Thomas J. Penfold. The importance of vibronic coupling for efficient reverse intersystem crossing in thermally activated delayed fluorescence molecules. *ChemPhysChem*, 17(19):2956–2961, 2016. doi:10.1002/cphc.201600662. URL `https://chemistry-europe.onlinelibrary.wiley.com/doi/abs/10.1002/cphc.201600662`.

[38] Sirong Lin, Zheng Pei, Bin Zhang, Huili Ma, and WanZhen Liang. Vibronic coupling effect on the vibrationally resolved electronic spectra and intersystem crossing rates of a tadf emitter: 7-phqad. *The Journal of Physical Chemistry A*, 126(2):239–248, 2022. ISSN 1520-5215. doi:10.1021/acs.jpca.1c08456.

[39] Abel Carreras and David Casanova. Theory of exciton dynamics in thermally activated delayed fluorescence. *ChemPhotoChem*, 6(8), 2022. doi:10.1002/cptc.202200066.

[40] D. K. A. Phan Huu, S. Saseendran, and A. Painelli. Effective models for tadf: the role of the medium polarizability. *J. Mater. Chem. C*, 10(13):4620–4628, 2022. doi:10.1039/D1TC05296A. URL `https://doi.org/10.1039/D1TC05296A`.

[41] T. Northey, J. Stacey, and T. J. Penfold. The role of solid state solvation on the charge transfer state of a thermally activated delayed fluorescence emitter. *Journal of Materials Chemistry C*, 5(42):11001–11009, 2017. doi:10.1039/c7tc04099g.

[42] Brunella Bardi, Davide Giavazzi, Elena Ferrari, Alessandro Iagatti, Mariangela Di Donato, D. K. Andrea Phan Huu, Francesco Di Maiolo, Cristina Sissa, Matteo Masino, Andrea Lapini, and Anna Painelli. Solid state solvation: a fresh view. *Materials Horizons*, 10(10):4172–4182, 2023. ISSN 2051-6355. doi:10.1039/d3mh00988b.

[43] Tomas Serevičius, Rokas Skaisgiris, Jelena Dodonova, Irina Fiodorova, Kristijonas Genevičius, Sigitas Tumkevičius, Karolis Kazlauskas, and Saulius Juršėnas. Temporal dynamics of solid-state thermally activated delayed fluorescence: Disorder or ultraslow solvation? *The Journal of Physical Chemistry Letters*, 13(7):1839–1844, 2022. doi:10.1021/acs.jpclett.1c03810.

[44] D. K. Andrea Phan Huu, Sangeeth Saseendran, Rama Dhali, Larissa Gomes Franca, Kleitos Stavrou, Andrew Monkman, and Anna Painelli. Thermally activated delayed fluorescence: Polarity, rigidity, and disorder in condensed phases. *Journal of the American Chemical Society*, 144(33):15211–15222, 2022. doi:10.1021/jacs.2c05537.

[45] Gary Chen, John R. Swartzfager, and John B. Asbury. Matrix dynamics and their crucial role in non-radiative decay during thermally activated delayed fluorescence. *Journal of the American Chemical Society*, 145(46):25495–25504, 2023. ISSN 1520-5126. doi:10.1021/jacs.3c11719.

[46] Katsuaki Suzuki and Hironori Kaji. Torsion angle analysis of a thermally activated delayed fluorescence emitter in an amorphous state using dynamic nuclear polarization enhanced solid-state nmr. *Journal of the American Chemical Society*, 145(30):16324–16329, 2023. ISSN 1520-5126. doi:10.1021/jacs.3c05204.

[47] Albin Cakaj, Markus Schmid, Alexander Hofmann, and Wolfgang Brütting. Controlling spontaneous orientation polarization in organic semiconductors – the case of phosphine oxides. *ACS Applied Materials & Interfaces; Interfaces*, 15(47):54721–54731, 2023. ISSN 1944-8252. doi:10.1021/acsami.3c13049.

[48] Rama Dhali, D. K. Andrea Phan Huu, Francesco Bertocchi, Cristina Sissa, Francesca Terenziani, and Anna Painelli. Understanding TADF: a joint experimental and theoretical study of DMAC-TRZ. *Physical Chemistry Chemical Physics*, 23(1):378–387, 2021. ISSN 1463-9084. doi:10.1039/d0cp05982j.

[49] A. D. K. Phan Huu, S. Saseendran, R. Dhali, L. G. Franca, K. Stavrou, A. P. Monkman, and A. Painelli. Thermally activated delayed fluorescence: Polarity, rigidity, and disorder in condensed phases. *Journal of the American Chemical Society*, 144(33):15211–15222, 2022. doi:10.1021/jacs.2c05537.

[50] B. Boldrini, E. Cavalli, A. Painelli, and F. Terenziani. Polar dyes in solution: A joint experimental and theoretical study of absorption and emission band shapes. *J. Phys. Chem. A*, 106:6286–6294, 2002.

[51] E. Campioli, S. Sanyal, A. Marcelli, M. Di Donato, M. Blanchard-Desce, O. Mongin, A. Painelli, and F. Terenziani. Addressing charge-transfer and locally-excited states in a twisted biphenyl push-pull chromophore. *ChemPhysChem*, 20:2860–2873, 2019. doi:10.1002/cphc.201900703.

[52] N. Haase, A. Danos, C. Pflumm, A. Morherr, P. Stachelek, A. Mekic, W. Brütting, and A. P. Monkman. Kinetic modeling of transient photoluminescence from thermally activated delayed fluorescence. *Journal of Physical Chemistry C*, 122(51):29173–29179, 2018. doi:10.1021/acs.jpcc.8b11020.

[53] K. Stavrou, L. G. Franca, and A. P. Monkman. Photophysics of tadf guest–host systems: Introducing the idea of hosting potential. *ACS Applied Electronic Materials*, 2(9):2868–2881, 2020. doi:10.1021/acsaelm.0c00514.

[54] M. J. Frisch, G. W. Trucks, H. B. Schlegel, G. E. Scuseria, M. A. Robb, J. R. Cheeseman, G. Scalmani, V. Barone, G. A. Petersson, H. Nakatsuji, X. Li, M. Caricato, A. V. Marenich, J. Bloino, B. G. Janesko, R. Gomperts, B. Mennucci, H. P. Hratchian, J. V. Ortiz, A. F. Izmaylov, J. L. Sonnenberg, D. Williams-Young, F. Ding, F. Lipparini, F. Egidi, J. Goings, B. Peng, A. Petrone, T. Henderson, D. Ranasinghe, V. G. Zakrzewski, J. Gao, N. Rega, G. Zheng, W. Liang, M. Hada, M. Ehara, K. Toyota, R. Fukuda, J. Hasegawa, M. Ishida, T. Nakajima, Y. Honda, O. Kitao, H. Nakai, T. Vreven, K. Throssell, Jr. J. A. Montgomery, J. E. Peralta, F. Ogliaro, M. J. Bearpark, J. J. Heyd, E. N. Brothers, K. N. Kudin, V. N. Staroverov, T. A. Keith, R. Kobayashi, J. Normand, K. Raghavachari, A. P. Rendell, J. C. Burant, S. S. Iyengar, J. Tomasi, M. Cossi, J. M. Millam, M. Klene, C. Adamo, R. Cammi, J. W. Ochterski, R. L. Martin, K. Morokuma, O. Farkas, J. B. Foresman, and D. J. Fox. Gaussian 16, revision b.01, 2016. Gaussian16 is a software package for computational chemistry.

[55] D. K. Andrea Phan Huu, Rama Dhali, Carlotta Pieroni, Francesco Di Maiolo, Cristina Sissa, Francesca Terenziani, and Anna Painelli. Antiadiabatic view of fast environmental effects on optical spectra. *Phys. Rev. Lett.*, 124:107401, Mar 2020. doi:10.1103/PhysRevLett.124.107401. URL `https://link.aps.org/doi/10.1103/PhysRevLett.124.107401`.

[56] Tian Lu and Feiwu Chen. Multiwfn: A multifunctional wavefunction analyzer. *Journal of Computational Chemistry*, 33(5):580–592, 2012. doi:10.1002/jcc.22885.

[57] Matteo Bedogni, Davide Giavazzi, Francesco Di Maiolo, and Anna Painelli. Shining light on inverted singlet–triplet emitters. *Journal of Chemical Theory and Computation*, 20(2):902–913, 2023. ISSN 1549-9626. doi:10.1021/acs.jctc.3c01112.

[58] J. N. Demas and G. A. Crosby. The measurement of photoluminescence quantum yields. a review. *The Journal of Physical Chemistry*, 75(8):991–1024, 1971. doi:10.1021/j100678a001.

[59] Kleitos Stavrou, Larissa G. Franca, Tobias Böhmer, Luka M. Duben, Christel M. Marian, and Andrew P. Monkman. Unexpected quasi-axial conformer in thermally activated delayed fluorescence dmac-trz, pushing green oleds to blue. *Advanced Functional Materials*, 33(25), 2023. ISSN 1616-3028. doi:10.1002/adfm.202300910.

[60] Rama Dhali, D. K. Andrea Phan Huu, Francesca Terenziani, Cristina Sissa, and Anna Painelli. Thermally activated delayed fluorescence: A critical assessment of environmental effects on the singlet–triplet energy gap. *The Journal of Chemical Physics*, 154(13):134112, apr 2021. ISSN 1089-7690. doi:10.1063/5.0042058.

[61] Youichi Tsuchiya, Stefan Diesing, Fatima Bencheikh, Yoshimasa Wada, Paloma L. dos Santos, Hironori Kaji, Eli Zysman-Colman, Ifor D. W. Samuel,

and Chihaya Adachi. Exact solution of kinetic analysis for thermally activated delayed fluorescence materials. *The Journal of Physical Chemistry A*, 125(36): 8074–8089, sep 2021. ISSN 1520-5215. doi:10.1021/acs.jpca.1c04056.

[62] Andrea Landi, D. K. Andrea Phan Huu, and Anna Painelli. From the fermi golden rule to open quantum systems: Basic concepts on non-radiative rates. *The Journal of Physical Chemistry C*, 128(43), October 2024.

[63] Lakowicz, J. R. *Principles of Fluorescence Spectroscopy*. Springer US, 1999. ISBN 978-1-4757-3063-0.

[64] Abraham Nitzan. *Chemical dynamics in condensed phases : relaxation, transfer, and reactions in condensed molecular systems*. Oxford University Press, Oxford, 2013. ISBN 9780199686681.

[65] Johannes Gierschner, Junqing Shi, Begoña Milián-Medina, Daniel Roca-Sanjuán, Shinto Varghese, and SooYoung Park. Luminescence in crystalline organic materials: From molecules to molecular solids. *Advanced Optical Materials*, 9(13):2002251, 2021. ISSN 2195-1071. doi:10.1002/adom.202002251.

[66] G. C. Schatz and Ratner M. A. *Quantum mechanics in chemistry*. Prentice Hall, 2002. ISBN 0130750115.

[67] Fabrizio Santoro, Alessandro Lami, Roberto Improta, and Vincenzo Barone. Effective method to compute vibrationally resolved optical spectra of large molecules at finite temperature in the gas phase and in solution. *The Journal of Chemical Physics*, 126(18):184102, 2007. ISSN 1089-7690. doi:10.1063/1.2721539.

[68] Qian Peng, Yuanping Yi, Zhigang Shuai, and Jiushu Shao. Excited state radiationless decay process with duschinsky rotation effect: Formalism and implementation. *The Journal of chemical physics*, 126(11), 2007.

[69] Bernardo de Souza, Frank Neese, and Róbert Izsák. On the theoretical prediction of fluorescence rates from first principles using the path integral approach. *The Journal of Chemical Physics*, 148(3):034104, 01 2018. ISSN 0021-9606. doi:10.1063/1.5010895. URL `https://doi.org/10.1063/1.5010895`.

[70] Raffaele Borrelli, Amedeo Capobianco, and Andrea Peluso. Franck–condon factors—computational approaches and recent developments. *Canadian Journal of Chemistry*, 91(7):495–504, 2013. doi:10.1139/cjc-2012-0518. URL `https://doi.org/10.1139/cjc-2012-0518`.

[71] R. R. Levich, V. G.and Dogonadze. Theory of rediationless electron transitions between ions in solution. *Proc. Akad. Naukl. SSSR.*, 29:9–13, 1959.

[72] R. R. Levich, V. G.and Dogonadze. Adiabatic theory for electron-transfer processes in solution. *Proc. Akad. Naukl. SSSR.*, 133:591–594, 1960.

[73] Joshua Jortner. Temperature dependent activation energy for electron transfer between biological molecules. *The Journal of Chemical Physics*, 64(12):4860–4867, 1976. ISSN 1089-7690. doi:10.1063/1.432142.

[74] Neil R. Kestner, Jean Logan, and Joshua Jortner. Thermal electron transfer reactions in polar solvents. *The Journal of Physical Chemistry*, 78(21):2148–2166, oct 1974. ISSN 1541-5740. doi:10.1021/j100614a017.

[75] Arieh Warshel. Dynamics of reactions in polar solvents. semiclassical trajectory studies of electron-transfer and proton-transfer reactions. *The Journal of Physical Chemistry*, 86(12):2218–2224, 1982. ISSN 1541-5740. doi:10.1021/j100209a016.

[76] S. Efrima and M. Bixon. On the role of vibrational excitation in electron transfer reactions with large negative free energies. *Chemical Physics Letters*, 25(1):34–37, 1974. ISSN 0009-2614. doi:10.1016/0009-2614(74)80325-8.

[77] Raffaele Borrelli and Andrea Peluso. Dynamics of radiationless transitions in large molecular systems: A franck–condon-based method accounting for displacements and rotations of all the normal coordinates. *The Journal of Chemical Physics*, 119(16):8437–8448, 2003. ISSN 1089-7690. doi:10.1063/1.1609979.

[78] Qian Peng, Yingli Niu, Qinghua Shi, Xing Gao, and Zhigang Shuai. Correlation function formalism for triplet excited state decay: Combined spin–orbit and nonadiabatic couplings. *Journal of Chemical Theory and Computation*, 9 (2):1132–1143, 2013. ISSN 1549-9626. doi:10.1021/ct300798t.

[79] Katsuyuki Shizu and Hironori Kaji. Theoretical determination of rate constants from excited states: Application to benzophenone. *The Journal of Physical Chemistry A*, 125(40):9000–9010, 2021. ISSN 1520-5215. doi:10.1021/acs.jpca.1c06165.

[80] Masaya Hagai, Naoto Inai, Takuma Yasuda, Kazuhiro J. Fujimoto, and Takeshi Yanai. Extended theoretical modeling of reverse intersystem crossing for thermally activated delayed fluorescence materials. *Science Advances*, 10(5):eadk3219, 2024. ISSN 2375-2548. doi:10.1126/sciadv.adk3219.

[81] Melvin Lax. The franck-condon principle and its application to crystals. *The Journal of chemical physics*, 20(11):1752–1760, 1952.

[82] Ryogo Kubo and Yutaka Toyozawa. Application of the method of generating function to radiative and non-radiative transitions of a trapped electron in a crystal. *Progress of Theoretical Physics*, 13(2):160–182, 1955.

[83] Alexander Humeniuk, Margarita Bužančić, Joscha Hoche, Javier Cerezo, Roland Mitrić, Fabrizio Santoro, and Vlasta Bonačić-Koutecký. Predicting fluorescence quantum yields for molecules in solution: A critical assessment of the harmonic approximation and the choice of the lineshape function. *The Journal of Chemical Physics*, 152(5), 2020. ISSN 1089-7690. doi:10.1063/1.5143212.

[84] Fabrizio Santoro, Alessandro Lami, Roberto Improta, Julien Bloino, and Vincenzo Barone. Effective method for the computation of optical spectra of large molecules at finite temperature including the duschinsky and herzberg–teller effect: The qx band of porphyrin as a case study. *The Journal of Chemical Physics*, 128(22):224311, 2008. ISSN 1089-7690. doi:10.1063/1.2929846.

[85] Raffaele Borrelli and Andrea Peluso. The temperature dependence of radiationless transition rates from ab initio computations. *Phys. Chem. Chem. Phys.*, 13:4420–4426, 2011. doi:10.1039/C0CP02307H. URL `http://dx.doi.org/10.1039/C0CP02307H`.

[86] Raffaele Borrelli, Amedeo Capobianco, and Andrea Peluso. Generating function approach to the calculation of spectral band shapes of free-base chlorin including duschinsky and herzberg–teller effects. *The Journal of Physical Chemistry A*, 116(40):9934–9940, 2012.

[87] Alberto Baiardi, Julien Bloino, and Vincenzo Barone. General time dependent approach to vibronic spectroscopy including franck–condon, herzberg–teller, and duschinsky effects. *Journal of chemical theory and computation*, 9(9): 4097–4115, 2013.

[88] R. Borrelli and A. Peluso. Elementary electron transfer reactions: from basic concepts to recent computational advances. *WIREs Computational Molecular Science*, 3:542–559, 2013. doi:10.1002/wcms.1147.

[89] Amalia Velardo, Alessandro Landi, Raffaele Borrelli, and Andrea Peluso. Reliable predictions of benzophenone singlet–triplet transition rates: A second-order cumulant approach. *The Journal of Physical Chemistry A*, 125(1):43–49, 2021. doi:10.1021/acs.jpca.0c07848. URL `https://doi.org/10.1021/acs.jpca.0c07848`. PMID: 33369419.

[90] A. G. Marshall and F. R. Verdun. *Fourier Transforms in NMR, Optical, and Mass Spectrometry*. Elsevier Science, 1989. ISBN 9780444873606.

[91] Yasuhito Ohta, Alexander V. Soudackov, and Sharon Hammes-Schiffer. Extended spin-boson model for nonadiabatic hydrogen tunneling in the condensed phase. *The Journal of Chemical Physics*, 125(14):144522, 2006. ISSN 1089-7690. doi:10.1063/1.2354500.

[92] Vincenzo Barone, Julien Bloino, Malgorzata Biczysko, and Fabrizio Santoro. Fully integrated approach to compute vibrationally resolved optical spectra: From small molecules to macrosystems. *Journal of Chemical Theory and Computation*, 5(3):540–554, 2009. ISSN 1549-9626. doi:10.1021/ct8004744.

[93] Raffaele Borrelli, Amedeo Capobianco, and Andrea Peluso. Generating function approach to the calculation of spectral band shapes of free-base chlorin including duschinsky and herzberg–teller effects. *The Journal of Physical Chemistry A*, 116(40):9934–9940, 2012. doi:10.1021/jp307887s. URL `https://doi.org/10.1021/jp307887s`. PMID: 22978703.

[94] Qian Peng, Di Fan, Ruihong Duan, Yuanping Yi, Yingli Niu, Dong Wang, and Zhigang Shuai. Theoretical study of conversion and decay processes of excited triplet and singlet states in a thermally activated delayed fluorescence molecule. *The Journal of Physical Chemistry C*, 121(25):13448–13456, 2017. ISSN 1932-7455. doi:10.1021/acs.jpcc.7b00692.

[95] Javier Cerezo and Fabrizio Santoro. Fcclasses3: Vibrationally-resolved spectra simulated at the edge of the harmonic approximation. *Journal of Computational Chemistry*, 44(4):626–643, 2023.

[96] Frank Neese. The orca program system. *Wiley Interdisciplinary Reviews: Computational Molecular Science*, 2(1):73–78, 2012.

[97] Zhigang Shuai. Thermal vibration correlation function formalism for molecular excited state decay rates. *Chinese Journal of Chemistry*, 38(11):1223–1232, 2020.

[98] T Elsaesser and W Kaiser. Vibrational and vibronic relaxation of large polyatomic molecules in liquids. *Annual Review of Physical Chemistry*, 42(1): 83–107, oct 1991. doi:10.1146/annurev.pc.42.100191.000503.

[99] D Giavazzi, F Di Maiolo, and A Painelli. The fate of molecular excited states: modeling donor–acceptor dyes. *Physical Chemistry Chemical Physics*, 24(9): 5555–5563, 2022.

[100] Di Maiolo, F. and Painelli, A. Intermolecular Energy Transfer in Real Time. *Journal of Chemical Theory and Computation*, 14(10):5339–5349, 2018. ISSN 1549-9626. doi:10.1021/acs.jctc.8b00540.

[101] D. Giavazzi, S. Saseendran, F. Di Maiolo, and A. Painelli. A comprehensive approach to exciton delocalization and energy transfer. *Journal of Chemical Theory and Computation*, 19(2):436–447, 2022. ISSN 1549-9626. doi:10.1021/acs.jctc.2c00980.

[102] H.-P. Breuer and F. Petruccione. *The Theory of Open Quantum Systems*, chapter 3, page 110. Oxford University Press, 2010. ISBN 9780199213900.

[103] Michael Thoss, Haobin Wang, and William H. Miller. Self-consistent hybrid approach for complex systems: Application to the spin-boson model with debye spectral density. *The Journal of Chemical Physics*, 115(7):2991–3005, 2001. ISSN 1089-7690. doi:10.1063/1.1385562.

[104] Amalia Velardo, Alessandro Landi, Raffaele Borrelli, and Andrea Peluso. Reliable predictions of benzophenone singlet–triplet transition rates: A second-order cumulant approach. *The Journal of Physical Chemistry A*, 125(1):43–49, 2020. ISSN 1520-5215. doi:10.1021/acs.jpca.0c07848.

[105] Xiang Sun and Eitan Geva. Nonequilibrium fermi's golden rule charge transfer rates via the linearized semiclassical method. *Journal of Chemical Theory and Computation*, 12(6):2926–2941, 2016. ISSN 1549-9626. doi:10.1021/acs.jctc.6b00236.

[106] Anupam Garg, José Nelson Onuchic, and Vinay Ambegaokar. Effect of friction on electron transfer in biomolecules. *The Journal of Chemical Physics*, 83(9): 4491–4503, 1985. ISSN 1089-7690. doi:10.1063/1.449017.

[107] Eric J. Heller. The semiclassical way to molecular spectroscopy. *Accounts of Chemical Research*, 14(12):368–375, 1981. ISSN 1520-4898. doi:10.1021/ar00072a002.

[108] B. Dick, R.M. Hochstrasser, and H.P. Trommsdorff. Chapter iii-6 - resonant molecular optics. In D.S. Chemla and J. Zyss, editors, *Nonlinear Optical Properties of Organic Molecules and Crystals*, pages 159–212. Academic Press, 1987. ISBN 978-0-12-170612-8. doi:https://doi.org/10.1016/B978-0-12-170612-8.50008-0. URL `https://www.sciencedirect.com/science/article/pii/B9780121706128500080`.

[109] S. Mukamel. *Principles of nonlinear optical spectroscopy*. Oxford series in optical and imaging sciences. Oxford University Press, 1995. ISBN 9780195092783.

[110] F. Di Maiolo and A. Painelli. Dynamical disorder and resonance energy transfer: a novel quantum-classical approach. *Physical Chemistry Chemical Physics*, 22(3):1061–1068, 2020. ISSN 1463-9084. doi:10.1039/c9cp06038c.

[111] Anna Painelli and Francesca Terenziani. Optical spectra of push–pull chromophores in solution: A simple model. *The Journal of Physical Chemistry A*, 104(47), 2000.

[112] Francesca Terenziani, Anna Painelli, and Davide Comoretto. Solvation effects and inhomogeneous broadening in optical spectra of phenol blue. *The Journal of Physical Chemistry A*, 104(47), 2000.

[113] Anna Painelli and Francesca Terenziani. Push–pull chromophores: Nlo responses, solvatochromism and vibrational spectra in a simple nonperturbative model. *Synthetic Metals*, 116(1):135–138, 2001. ISSN 0379-6779. doi:https://doi.org/10.1016/S0379-6779(00)00472-0. URL `https://www.sciencedirect.com/science/article/pii/S0379677900004720`.

[114] F. Di Maiolo and A. Painelli. Dynamical disorder and resonance energy transfer: a novel quantum-classical approach. *Physical Chemistry Chemical Physics*, 22(3):1061–1068, 2020. doi:10.1039/C9CP06038C.

[115] Peter Hamm and Martin T. Zanni. *Concepts and Methods of 2D Infrared Spectroscopy*. Cambridge University Press, 2011. ISBN 978-1-107-00005-6.

[116] Mulliken, R. S. Molecular Compounds and their Spectra. II. *J. Am. Chem. Soc.*, 74(3):811–824, 1952.

[117] B.J. Orr and J.F. Ward. Perturbation theory of the non-linear optical polarization of an isolated system. *Molecular Physics*, 20(3):513–526, 1971. ISSN 1362-3028. doi:10.1080/00268977100100481.

[118] Python Software Foundation. *Python Language Reference, version 3.11*, 2023. URL `https://www.python.org/`.

[119] Sebastian Gorgon, Kuo Lv, Jeannine Grüne, Bluebell H. Drummond, William K. Myers, Giacomo Londi, Gaetano Ricci, Danillo Valverde, Claire Tonnelé, Petri Murto, Alexander S. Romanov, David Casanova, Vladimir Dyakonov, Andreas Sperlich, David Beljonne, Yoann Olivier, Feng Li, Richard H. Friend, and Emrys W. Evans. Reversible spin-optical interface in luminescent organic radicals. *Nature*, 620(7974):538–544, 2023. ISSN 1476-4687. doi:10.1038/s41586-023-06222-1.

[120] Fabio Biscarini, Eugenio Coronado, Anna Painelli, and Masahiro Yamashita. Materials for molecular electronics and magnetism. *Journal of Materials Chemistry C*, 9(33):10521–10523, 2021. doi:10.1039/d1tc90161c.

[121] Hiroki Uoyama, Kenichi Goushi, Katsuyuki Shizu, Hiroko Nomura, and Chihaya Adachi. Highly efficient organic light-emitting diodes from delayed fluorescence. *Nature*, 492(7428):234–238, Dec 2012. ISSN 1476-4687. doi:10.1038/nature11687. URL `https://doi.org/10.1038/nature11687`.

[122] Xin Ai, Emrys W. Evans, Shengzhi Dong, Alexander J. Gillett, Haoqing Guo, Yingxin Chen, Timothy J. H. Hele, Richard H. Friend, and Feng Li. Efficient radical-based light-emitting diodes with doublet emission. *Nature*, 563(7732): 536–540, 2018. ISSN 1476-4687. doi:10.1038/s41586-018-0695-9.

[123] Yingli Niu, Qian Peng, Chunmei Deng, Xing Gao, and Zhigang Shuai. Theory of excited state decays and optical spectra: Application to polyatomic molecules. *The Journal of Physical Chemistry A*, 114(30):7817–7831, 2010. ISSN 1520-5215. doi:10.1021/jp101568f.

[124] Nikolay Klinduhov and Kamel Boukheddaden. Vibronic theory of ultrafast intersystem crossing dynamics in a single spin-crossover molecule at finite temperature beyond the born–oppenheimer approximation. *The Journal of Physical Chemistry Letters*, 7(4):722–727, 2016.

[125] Rudolph A. Marcus. Electron transfer reactions in chemistry: Theory and experiment (nobel lecture). *Angewandte Chemie International Edition in English*, 32(8):1111–1121, 1993. ISSN 0570-0833. doi:10.1002/anie.199311113.

[126] Qian Peng, Yuanping Yi, Zhigang Shuai, and Jiushu Shao. Toward quantitative prediction of molecular fluorescence quantum efficiency: Role of duschinsky rotation. *Journal of the American Chemical Society*, 129(30):9333–9339, 2007.

[127] M. Etherington, F. Franchello, J. Gibson, et al. Regio- and conformational isomerization critical to design of efficient thermally-activated delayed fluorescence emitters. *Nature Communications*, 8:14987, 2017. doi:10.1038/ncomms14987.

[128] H. Miranda-Salinas, Y.-T. Hung, Y.-S. Chen, D. Luo, H.-C. Kao, C.-H. Chang, K.-S. Wong, and A. P. Monkman. Controlling through-space and through-bond intramolecular charge transfer in bridged d–d'-a tadf emitters. *Journal of Materials Chemistry C*, 9:8819, 2021. doi:10.1039/D1TC02316K.

[129] K. Stavrou, L. G. Franca, A. Danos, and A. P. Monkman. Key requirements for ultraefficient sensitization in hyperfluorescence organic light-emitting diodes. *Nature Photonics*, 18:554–561, 2024. doi:10.1038/s41566-024-01395-1.

[130] J. Wang, J. Lu, and J. Zhang. Tuning the electronic and optical properties of diphenylsulphone based thermally activated delayed fluorescent materials via structural modification: A theoretical study. *Dyes and Pigments*, 143:42–47, 2017. doi:10.1016/j.dyepig.2017.03.064.

[131] Y.-L. Ji and Q.-S. Li. Boron-containing thermally activated delayed blue fluorescence materials via donor tuning: A theoretical study. *Chinese Journal of Chemical Physics*, 35(3):499–508, 2022. doi:10.1063/1674-0068/cjcp2203039.

[132] A. Kamal, S. M. Hussaini, V. L. Nayak, M. S. Malik, M. L. Sucharitha, T. B. Shaik, M. Ashraf, and C. Bagul. Bioorg. med. chem. *Bioorganic & Medicinal Chemistry*, 22:6755–6767, 2014. doi:10.1016/j.bmc.2014.11.001.

[133] P. Meisel, E. Kretzschmar, and R. Bartsch. Pharmazie. *Pharmazie*, 39:671–672, 1984. doi:10.1002/chin.198508199.

[134] P. Sudhakar, S. Kuila, K. Stavrou, A. Danos, A. M. Z. Slawin, A. P. Monkman, and E. Zysman-Colman. Azaborine as a versatile weak donor for thermally activated delayed fluorescence. *ACS Applied Materials & Interfaces*, 15:25806–25818, 2023. doi:10.1021/acsami.3c05409.

[135] Anna Painelli and Francesca Terenziani. Optical spectra of push-pull chromophores in solution: A simple model. *J. Phys. Chem. A*, 104(47):11041–11048, 2000. doi:10.1021/jp0016075.

[136] Anna Painelli and Francesca Terenziani. Solvation effects and inhomogeneous broadening in optical spectra. *J. Phys. Chem. A*, 104(47):11049–11057, 2000. doi:10.1021/jp001608x.

[137] S. R. Marder, D. N. Beratan, and L. T. Cheng. Approaches for optimizing the first electronic hyperpolarizability of conjugated organic molecules. *Science*, 252(5002):103–106, 1991. doi:10.1126/science.252.5002.103. URL `https://doi.org/10.1126/science.252.5002.103`.

[138] Colin D. Abernethy, Gareth M. Codd, Mark D. Spicer, and Michelle K. Taylor. A highly stable N-heterocyclic carbene complex of trichloro-oxo-vanadium(v) displaying novel Cl—C(carbene) bonding interactions. *J. Am. Chem. Soc.*, 125(5):1128–1129, 2003. doi:10.1021/ja0276321.

[139] 2007. URL `http://pubs.acs.org/books/references.shtml`.

[140] Anthony J. Arduengo, III, H. V. Rasika Dias, Richard L. Harlow, and Michael Kline. Electronic stabilization of nucleophilic carbenes. *J. Am. Chem. Soc.*, 114(14):5530–5534, 1992. doi:10.1021/ja00040a007.

[141] Anthony J. Arduengo, III, Siegfried F. Gamper, Joseph C. Calabrese, and Fredric Davidson. Low-coordinate carbene complexes of nickel(0) and platinum(0). *J. Am. Chem. Soc.*, 116(10):4391–4394, 1994. doi:10.1021/ja00089a029.

[142] Leah N. Appelhans, Daniele Zuccaccia, Anes Kovacevic, Anthony R. Chianese, John R. Miecznikowski, Aleco Macchioni, Eric Clot, Odile Eisenstein, and Robert H. Crabtree. An anion-dependent switch in selectivity results from a change of C—H activation mechanism in the reaction of an imidazolium salt with $IrH_5(PPh_3)_2$. *J. Am. Chem. Soc.*, 127(46):16299–16311, 2005. doi:10.1021/ja055317j.

[143] Anne M. Coghill and Lorrin R. Garson, editors. *The ACS Style Guide*. Oxford University Press, Inc. and The American Chemical Society, New York, 3 edition, 2006.

[144] Frank Albert Cotton, Geoffrery Wilkinson, Carlos A. Murillio, and Manfred Bochmann. *Advanced Inorganic Chemistry*. Wiley, Chichester, 6 edition, 1999.

[145] Angel Abarca, Pilar Gómez-Sal, Avelino Martín, Miguel Mena, Josep María Poblet, and Carlos Yélamos. Ammonolysis of mono(pentamethylcyclopentadienyl) titanium(IV) derivatives. *Inorg. Chem.*, 39(4):642–651, 2000. doi:10.1021/ic9907718.

[146] Brunella Bardi, Davide Giavazzi, Elena Ferrari, Alessandro Iagatti, Mariangela Di Donato, D. K. Andrea Phan Huu, Francesco Di Maiolo, Cristina Sissa, Matteo Masino, Andrea Lapini, and Anna Painelli. Solid state solvation: a fresh view. *Mater. Horiz.*, 10:4172–4182, 2023. doi:10.1039/D3MH00988B. URL `http://dx.doi.org/10.1039/D3MH00988B`.

[147] Ettore Crovini, Rama Dhali, Dianming Sun, Tomas Matulaitis, Thomas Comerford, Alexandra M. Z. Slawin, Cristina Sissa, Francesco Azzolin, Francesco Di Maiolo, Anna Painelli, and Eli Zysman-Colman. Molecular geometry and the photophysics of thermally activated delayed fluorescence: the strange case of dmac-py-trz. *J. Mater. Chem. C*, 11:8284–8292, 2023. doi:10.1039/D2TC05213J. URL `http://dx.doi.org/10.1039/D2TC05213J`.

[148] Yoshimasa Wada, Katsuyuki Shizu, and Hironori Kaji. Molecular vibration accelerates charge transfer emission in a highly twisted blue thermally activated delayed fluorescence material. *The Journal of Physical Chemistry A*, 125(21):4534–4539, 2021. ISSN 1520-5215. doi:10.1021/acs.jpca.0c11478.

[149] Glenn A. Crosby and James N. Demas. Measurement of photoluminescence quantum yields. review. *The Journal of Physical Chemistry*, 75(8):991–1024, 1971. ISSN 1541-5740. doi:10.1021/j100678a001.

List of publications

- Landi, A.; Phan Huu, D. K. A.; Painelli, A. From the Fermi Golden Rule to Open Quantum Systems: Basic Concepts on Non-radiative Rates. *J. Phys. Chem. C* **2024**, *128* (43), 31967–31982.
- Di Maiolo, F.; Phan Huu, D. K. A.; Giavazzi, D.; Landi, A.; Racchi, O.; Painelli, A. Shedding Light on Thermally-Activated Delayed Fluorescence. *Chem. Sci.* **2024**, *15* (15), 5434–5450.